

Argonne National Laboratory

REACTOR DEVELOPMENT PROGRAM PROGRESS REPORT

February 1971

The facilities of Argonne National Laboratory are owned by the United States Government. Under the terms of a contract (W-31-109-Eng-38) between the U. S. Atomic Energy Commission, Argonne Universities Association and The University of Chicago, the University employs the staff and operates the Laboratory in accordance with policies and programs formulated, approved and reviewed by the Association.

MEMBERS OF ARGONNE UNIVERSITIES ASSOCIATION

The University of Arizona	Kansas State University	The Ohio State University
Carnegie-Mellon University	The University of Kansas	Ohio University
Case Western Reserve University	Loyola University	The Pennsylvania State University
The University of Chicago	Marquette University	Purdue University
University of Cincinnati	Michigan State University	Saint Louis University
Illinois Institute of Technology	The University of Michigan	Southern Illinois University
University of Illinois	University of Minnesota	The University of Texas at Austin
Indiana University	University of Missouri	Washington University
Iowa State University	Northwestern University	Wayne State University
The University of Iowa	University of Notre Dame	The University of Wisconsin

NOTICE

This report was prepared as an account of work sponsored by the United States Government. Neither the United States nor the United States Atomic Energy Commission, nor any of their employees, nor any of their contractors, subcontractors, or their employees, makes any warranty, express or implied, or assumes any legal liability or responsibility for the accuracy, completeness or usefulness of any information, apparatus, product or process disclosed, or represents that its use would not infringe privately-owned rights.

Printed in the United States of America
Available from
National Technical Information Service
U.S. Department of Commerce
5285 Port Royal Road
Springfield, Virginia 22151
Price: Printed Copy \$3.00; Microfiche \$0.95

ARGONNE NATIONAL LABORATORY
9700 South Cass Avenue
Argonne, Illinois 60439

REACTOR DEVELOPMENT PROGRAM
PROGRESS REPORT

February 1971

Robert B. Duffield, Laboratory Director
Robert V. Laney, Associate Laboratory Director

<u>Division</u>	<u>Director</u>
Applied Physics	R. Avery
Chemical Engineering	R. C. Vogel
EBR-II Project	M. Levenson
Engineering and Technology	S. A. Davis
Idaho Facilities	R. G. Staker
Materials Science	P. G. Shewmon
Reactor Analysis and Safety	W. R. Simmons

Report coordinated by
M. Weber and V. G. Trice, Jr.

Issued March 22, 1971

FOREWORD

The Reactor Development Program Progress Report describes current activities, technical progress, and technical problems in the program at Argonne National Laboratory sponsored by the USAEC Division of Reactor Development and Technology. Organized in accordance with the AEC's budget and reporting classifications, the report is published monthly. Not all projects are reported every month, but a running account of each project is maintained in the series of reports.

The last six reports
in this series are:

August 1970	ANL-7737
September 1970	ANL-7742
October 1970	ANL-7753
November 1970	ANL-7758
December 1970	ANL-7765
January 1971	ANL-7776

REACTOR DEVELOPMENT PROGRAM

Highlights of Project Activities for February 1971

EBR-II

The cause of the noise in the intermediate heat exchanger was found and corrected. The reactor is scheduled to be critical the first week in March.

Recently developed methods for analyzing spatial variations in neutron- and gamma-flux levels in heterogeneous reactors (such as EBR-II) show that irradiation conditions can be modified significantly in small regions of the core without severely distorting flux and fission rate in the reactor. These methods have been used to define a modified EBR-II core-loading pattern to accommodate instrumented subassembly XX03, which is to be irradiated at a controlled temperature through gamma heating. The pattern ensures the needed 39% reduction in the gamma-flux level in XX03, but will have negligible effect on most of the other driver and fueled experimental subassemblies.

ZPR-6

Using a pneumatic sample oscillator and a calibrated autorod system in ZPR-6 Assembly 7, central reactivity worths were studied in two zones to compare results obtained in plate and fuel-pin environments of identical homogeneous isotopic compositions. The reactivity worths of the fissile, fertile, control, coolant, and structural materials measured in plate and pin zones agree well with each other and indicate a possible small difference in perturbation denominator for the two cores.

ZPR-9

A consolidation of the great range of data relating to the reactivity worth of peripheral and in-core control rods and to simulated test loops in the FTR-3 core, ZPR-9 Assembly 26, presents a consistent pattern of results. Worths are not strongly dependent on the configuration of other control rods or loops in the assembly.

ZPPR

The low-frequency polarity-coherence-function technique was used to measure the worth of ^{10}B safety rods in ZPPR Assembly 2. Results were compared with a calibration established by inverse-kinetics techniques over the reactivity range between \$0.06 and \$2.70 subcritical.

TABLE OF CONTENTS

<u>189a No.</u>		<u>Page</u>
	I. LIQUID METAL FAST BREEDER REACTORS	1
	A. Fuel Development	1
02-526	1. Fuel Cladding and Structure	1
	a. In-pile Stainless Steel Swelling and Mechanical Behavior	1
	B. Physics Development	2
02-009	1. Theoretical Reactor Physics	2
02-010	a. General Fast Reactor Physics	2
	b. Fast Critical Experiments-- Theoretical Support--Idaho	8
02-134	c. Fast Critical Experiments-- Theoretical Support--Illinois	10
	2. Experimental Reactor Physics	11
02-011	a. Fast Critical Experiments--Experimental Support--Idaho	11
02-013	b. Fast Critical Experiments--Experimental Support--Illinois	12
	3. ZPR-6 and -9 Operations and Analysis	13
02-179	a. Fast Critical Facilities Experiments and Evaluation--Illinois	13
	4. ZPPR and ZPR-3 Operations and Analysis	19
02-181	a. Fast Critical Facilities Experiments and Evaluation--Idaho	19
	C. Component Development	21
	1. Instrumentation and Control	21
02-025	a. FFTF Instrumentation Development	21
02-138	b. Neutron-detector Channel Development	26
02-528	c. Plant Dynamics and Control Analysis	30
	2. Fuel Handling, Vessels, and Internals	30
02-026	a. Core Component Test Loop (CCTL)	30
	D. Experimental Breeder Reactor No. II--Research and Development	32
02-144	1. Reactor Analysis, Testing, and Methods Development	32
	a. Nuclear, Thermal, and Hydraulic Surveillance	32

TABLE OF CONTENTS

<u>189a No.</u>		<u>Page</u>
02-151	2. Characterization of Irradiation Environment	46
	a. Axial Gamma-deposition Profiles for ZPR-3 Assemblies 60, 61, and 62	46
	b. Calculated Fine-energy Flux Spectra in ZPR-3 Assembly 61	47
	c. Characterization of Environment of Subassembly X012 in EBR-II	47
02-530	3. Operation of Data Acquisition System (DAS)	50
	PUBLICATIONS	51
II.	GENERAL REACTOR TECHNOLOGY	53
	A. Applied and Reactor Physics Development	53
	1. Theoretical Reactor Physics	53
02-081	a. Theoretical Reactor Physics	53
	2. Nuclear Data	60
02-085	a. Reactor Code Center	60
	B. Reactor Fuels and Materials Development	61
none	1. Core Applications Planning and Analysis	61
	a. Empirical Assessment of Swelling and Creep Correlations	61
	2. Fuels and Claddings	65
02-086	a. Behavior of Reactor Materials	65
02-005	b. Oxide Fuel Studies	66
	3. Radiation Damage on Structural Materials	68
02-091	a. In-reactor Creep Studies	68
	4. Techniques of Fabrication and Testing	69
02-092	a. Nondestructive Testing Research and Development	69
02-133	b. NDT Measurement of Effective Cold Work in Cladding Tubes	70
	5. Engineering Properties of Reactor Materials	71
02-094	a. High-temperature Properties of Ceramic Fuels	71
	C. Engineering Development	76
02-096	1. Instrumentation and Control	76
	a. Boiling Detector	76
02-097	2. Heat Transfer and Fluid Flow	80
	a. LMFBR Flow Stability Studies	80

TABLE OF CONTENTS

<u>189a No.</u>		<u>Page</u>
	D. Chemistry and Chemical Separations	80
	1. Fuel Cycle Technology	80
02-159	a. LMFBR Reprocessing--Plutonium Isolation	80
02-173	b. Molten Metal Decladding of LMFBR Fuels	81
02-157	c. LMFBR Fuel Materials Preparation--U/Pu Nitrates to Oxides	83
	2. General Chemistry and Chemical Engineering	84
02-162	a. Thermophysical Properties of Reactor Fuels	84
02-175	b. Physical and Chemical Studies--Molten Fuel, Cladding, and Coolant	89
	PUBLICATIONS	90
	III. NUCLEAR SAFETY	91
	A. LMFBR Safety	91
02-112	1. Accident Analysis and Safety Evaluation	91
	a. Initiating Accident Code Development	91
	b. Disassembly Accident Analysis, Including Computer Code Development and Sensitivity Studies	91
02-114	2. Coolant Dynamics	94
	a. Sodium Superheat	94
	b. Sodium Expulsion and Reentry: In-pile	97
	c. Liquid-Vapor Dynamics	98
	d. Sodium Simulations	101
02-117	3. Fuel Dynamics Studies in TREAT	101
	a. Transient In-pile Tests with Ceramic Fuel	101
	b. Experimental Support	103
	c. Analytical Support	104
02-119	4. High-temperature Physical Properties and Equation-of-state of Reactor Materials	106
	a. Theoretical Extrapolation of Measured Physical Properties to Very High Temperatures	106
	b. High-temperature Physical-property Studies	107

TABLE OF CONTENTS

<u>189a No.</u>		<u>Page</u>
02-164	5. Fuel-Coolant Interactions	108
	a. Model Development	108
	B. Operations	111
02-122	1. TREAT Operations	111
	a. Operations	111
	C. Effluent Control	111
	1. Environmental Studies	111
02-184	a. Mass/Energy Balance of the Great Lakes	111
	PUBLICATIONS	113

Listing of the
ANL Reactor Development Program Projects
in 189a Order

189a No.	Reported This Month	189a Title	RDT Branch
02-005	x	Oxide Fuel Studies	RT-FM
02-009	x	General Fast Reactor Physics	RT-PH
02-010	x	Fast Critical Experiments--Theoretical Support--Idaho	RT-PH
02-011	x	Fast Critical Experiments--Experimental Support--Idaho	RT-PH
02-012		Fast Critical Experiments--Industrial Appointments	RT-PH
02-013	x	Fast Critical Experiments--Experimental Support--Illinois	RT-PH
02-015		Planning and Evaluation of FFTF Critical Assembly Experiments	RT-PH
02-019		Production of Materials for ZPR Experiments	RE-FE
02-020		ZPR Materials Procurement	RE-FE
02-021		On-line Monitoring and Sampling for Sodium Systems	RT-CC
02-024		Instrumentation Development for Instrumented Subassembly	PE-IC
02-025	x	FFTF Instrumentation Development	PE-IC
02-026	x	Core Component Test Loop (CCTL)	RE-CD
02-035		LMFBR Program Office	PM-LP
02-036		EBR-II Program Management	PM-EB
02-038		System Design Descriptions	PE-LS
02-045		Equipment--Fuel Related	RE-FH
02-046		New Subassemblies and Experimental Support	RE-CD
02-048		Instrumented Subassemblies	RE-CD
02-051		Coolant Chemistry	RT-CC
02-053		Experimental Irradiation and Testing	RT-FM
02-061		Nuclear Instrument Test Facility	PE-IC
02-063		Materials-Coolant Compatibility	RT-CC
02-065		Procedures, Planning, and Scheduling	PE-LS
02-068		Systems Engineering	PE-LS
02-073		Fuel and Hardware Procurement	RE-FE
02-075		Reactor Operations	PE-LS
02-076		Fuel Cycle Facility Operations	RE-FE
02-079		Studies and Evaluations for RDT Program Analysis Branch	PA-PA
02-081	x	Theoretical Reactor Physics	RT-PH
02-082		Cross-section Measurements	RT-PH

189a No.	Reported This Month	189a Title	RDT Branch
02-083		Burnup Analysis and Fission Yields for Fast Reactors	RT-PH
02-084		Determination of Nuclear Constants	RT-PH
02-085	x	Reactor Code Center	RT-PH
02-086	x	Behavior of Reactor Materials	RT-FM
02-087		Chemistry of Irradiated Fuel Materials	RT-FM
02-088		Thermodynamics of Carbide Fuel	RT-FM
02-091	x	In-reactor Creep Studies	RT-FM
02-092	x	Nondestructive Testing Research and Development	RT-FM
02-094	x	High-temperature Properties of Ceramic Fuels	RT-FM
02-096	x	Instrumentation and Control	RT-ST
02-097	x	Heat Transfer and Fluid Flow	RT-ST
02-099		Engineering Mechanics	RT-ST
02-112	x	Accident Analysis and Safety Evaluation	NS-FS
02-114	x	Coolant Dynamics	NS-FS
02-115		Core Structural Safety	NS-FS
02-116		Fuel-element Failure Propagation	NS-FS
02-117	x	Fuel Dynamics Studies in TREAT	NS-FS
02-119	x	High-temperature Physical Properties and Equation-of-state of Reactor Materials	NS-FS
02-120		Fast Reactor Safety Test Facility Study	NS-FS
02-121		1000-MWe Safety Analysis Study Subcontracts	NS-FS
02-122	x	TREAT Operations	NS-RD
02-126		Reactor System and Containment Structural Dynamic Response	NS-FS
02-131		EBR-II In-core Instrument Test Facility	PE-IC
02-133	x	NDT Measurement of Effective Cold Work in Cladding Tubes	RT-FM
02-134	x	Fast Critical Experiments--Theoretical Support--Illinois	RT-PH
02-137		Nonmetallic Impurity Interactions in Sodium-Metal Systems	RT-CC
02-138	x	Neutron-detector Channel Development	PE-IC
02-144	x	Reactor Analysis, Testing, and Methods Development	RE-CD
02-145		Metal Driver Fuel Development and Application	RE-FE
02-148		Operation with Failed Fuel	RE-CD
02-150		Hot Fuel Examination Facilities	PE-FH
02-151	x	Characterization of Irradiation Environment	RE-CD
02-156		Sodium Impurity Analysis and Control	RT-CC

189a No.	Reported This Month	189a Title	RDT Branch
02-157	x	LMFBR Fuel Materials Preparation--U/Pu Nitrates to Oxides	RT-FR
02-158		LMFBR Fuel Fabrication--Analyses and Continuous Processing	RT-FR
02-159	x	LMFBR Reprocessing--Plutonium Isolation	RT-FR
02-162	x	Thermophysical Properties of Reactor Fuels	RT-FR
02-164	x	Fuel-Coolant Interactions	NS-FS
02-165		Post-accident Heat Removal	NS-FS
02-166		Thermal-plume Dispersion Studies	NS-EE
02-173	x	Molten Metal Decladding of LMFBR Fuels	RT-FR
02-175	x	Physical and Chemical Studies--Molten Fuel, Cladding, and Coolant	RT-FR
02-178		ZPR-6 and -9 Operations and Maintenance	RT-PH
02-179	x	Fast Critical Facilities Experiments and Evaluation--Illinois	RT-PH
02-180		ZPPR and ZPR-3 Operations and Maintenance	RT-PH
02-181	x	Fast Critical Facilities Experiments and Evaluation--Idaho	RT-PH
02-182		LMFBR Fuel Management Studies	RT-FR
02-184	x	Mass/Energy Balance of the Great Lakes	NS-ES
02-185		Lake Circulation Model Development	NS-EE
02-186		1000-MWe Contract Management, Technical Review, and Evaluation	PE-LM
02-191		Disposal of EBWR Fuel	RD-AB
02-194		Surveillance and Failure Evaluation of Experimental Fuel Irradiations	RT-FM
02-195		Scram System Study	PE-LS
02-197		TREAT Improvement Studies	PM-EB
02-200		Conceptual Design Study of FFTF Vessel Head-cavity System	RE-CD
02-201		Utilization of EBR-II in the Development of Sodium Technology	RT-CC
02-509		Sodium Chemistry and Radioactive Contaminant Behavior	RT-CC
02-526	x	In-pile Stainless Steel Swelling and Mechanical Behavior	RT-FM
02-528	x	Plant Dynamics and Control Analysis	PE-IC
02-530	x	Operation of Data Acquisition System (DAS)	PE-IC

I. LIQUID METAL FAST BREEDER REACTORS

A. Fuel Development

1. Fuel Cladding and Structure

a. In-pile Stainless Steel Swelling and Mechanical Behavior (189a 02-526)

(i) Neutron Simulation Studies Using 4-MeV Dynamitron (A. Taylor)

Last Reported: ANL-7765, p. 1 (Dec 1970).

A preliminary examination of Type 304 stainless steel irradiated with 3-MeV Ni^+ ions at 500°C has been made. Foils were prepared at approximately 0.2 and 0.5 μm below the irradiated surface in Sample 1201-1 and examined by transmission-electron microscopy. The distribution of the void diameters versus number density calculated from an estimated foil thickness for the two foils is given in Fig. I.A.1.

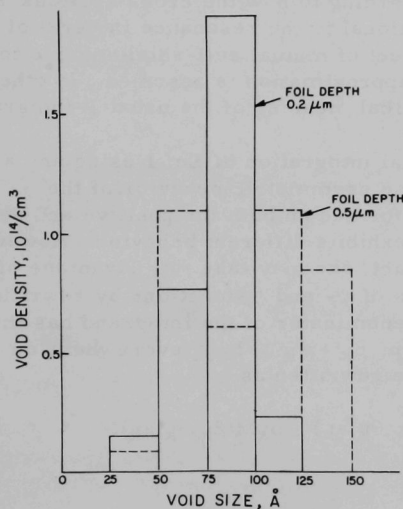


Fig. I.A.1

Distribution of Void Diameters vs Void Number Density Calculated from Estimated Foil Thickness. Solid line indicates data at 0.2 μm ; broken line indicates data at 0.5 μm below irradiated surface. Mean void diameters were 83 ± 19 Å and 102 ± 36 Å, respectively. Neg. No. MSD-53953.

The relative variation of the void number density and void diameter is in qualitative agreement with the calculated distribution of the radiation damage. For Sample 1201-1, the damage peaks at 0.55 μm at approximately 80 displacements per atom and falls to 40 displacements per atom 0.2 μm below the surface.

B. Physics Development

1. Theoretical Reactor Physics

a. General Fast Reactor Physics (189a 02-009)

(i) Resonance and Doppler Theory (R. N. Hwang)

Last Reported: ANL-7669, pp. 1-9 (Feb 1970).

(a) An Efficient Method for Evaluating $J(\beta_k, \theta_k, a_k, b_k)$
Integral. The integral $J(\beta_k, \theta_k, a_k, b_k)$ represents the generalized form of the usual J-integral which arises: (1) when the effect of the interference scattering cross section in the single-level formulation is included; or (2) when the multilevel formalism is used. $J(\beta_k, \theta_k, a_k, b_k)$ is defined as

$$J(\beta_k, \theta_k, a_k, b_k) = \frac{1}{2} \int_{-\infty}^{\infty} \frac{\psi(\theta_k, x_k) + b_k \chi(\theta_k, x_k)}{\beta_k + 2a_k \chi_k + \psi(\theta_k, x_k)} dx_k, \quad (1)$$

where the parameters are defined according to how the cross sections are formulated.* Physically, it is proportional to the resonance integral of an "isolated" resonance excluding the effect of mutual self-shielding due to the neighboring resonances when the NR approximation is assumed. In other words, it has precisely the same physical meaning of the usual J-integral.

A direct numerical integration of Eq. 1 using any algorithm is highly undesirable due to the asymmetric behavior of the χ -function. The integration must be performed on both the positive and negative planes of x_k where the integrand exhibits different behavior. However, this difficulty can be avoided and, in fact, one may take full advantage of the symmetric and asymmetric properties of ψ - and χ -functions by rewriting Eq. 1 in a different form. Since the denominator of the integrand has the physical meaning of total cross section, $\beta_k + \psi_k > 2a_k \chi$ everywhere on physical grounds. Hence, Eq. 1 can be rewritten as

$$J(\beta_k, \theta_k, a_k, b_k) = J(\beta_k, \theta_k) + I(\beta_k, \theta_k, a_k) - b_k M(\beta_k, \theta_k, a_k), \quad (2)$$

where

$$I(\beta_k, \theta_k, a_k) = (2a_k)^2 \int_0^{\infty} \frac{\chi^2}{(\beta_k + \psi)^2 - \chi^2} \cdot \frac{\psi}{\beta_k + \psi} dx_k, \quad (3)$$

$$M(\beta_k, \theta_k, a_k) = (2a_k)^2 \int_0^{\infty} \frac{\chi^2}{(\beta_k + \psi)^2 - \chi^2} dx_k, \quad (4)$$

*R. N. Hwang, Nucl. Sci. Eng. **21**, 523-535 (1965); *ibid.* **36**, 82-96 (1969).

and $J(\beta_k, \theta_k)$ is the usual J-integral and b_k is equal to zero if the Breit-Wigner equation is used.

The magnitudes of M- and I-integrals are generally much smaller than the corresponding $J(\beta_k, \theta_k)$, and therefore less strict error criteria are required. An accurate and efficient algorithm using the Gauss-Jacobi quadrature is proposed to evaluate these integrals simultaneously. The efficiency of any Gauss quadrature, in general, depends strongly on whether the integrand is expressible as a power series of low order in terms of the variable of integration. The integrands under consideration generally do not meet this requirement, since ψ - and χ -functions quickly approach their asymptotic series when x_k becomes large. This problem can be resolved by using the technique of rational transformation whereby the integrands become expressible by a rapidly convergent power series of the new variable u . For simplicity, let a symmetric function $f(x)$ be the integrand under consideration. A rational transformation is made so that

$$\begin{aligned} \int_0^{\infty} f(x) dx &= \frac{1}{K} \int_0^1 \frac{du}{\sqrt{1-u^2}} \frac{f(u)}{1-u^2} \\ &= \frac{\pi/N}{K} \left\{ \frac{1}{2} f(0) + \sum_{i=2}^{(N-1)/2} \frac{f(u_i)}{1-u_i^2} \right\} + R_N, \end{aligned} \quad (5)$$

where N , the total number of points over both the positive and negative domains of u , is taken to be an odd integer, the new variable u is related to x by

$$u^2 = \frac{K^2 x^2}{1 + K^2 x^2}, \quad (6)$$

and the free parameter K is to be chosen.

Equation 5 represents the Gauss-Jacobi quadrature with an odd number of mesh points,* where the related orthogonal polynomial is the Chebyshev polynomial of first kind and

$$u_i = \cos \frac{(2i-1)\pi}{2N}; \quad (7)$$

$$R_N = \frac{\pi}{(2N)! 2^{2N-1}} f^{(2N)}(\xi); \quad 0 < \xi < 1. \quad (8)$$

*A. H. Stroud and D. Secrest, Gaussian Quadrature Formulas, Prentice-Hall, Inc. (1966).

The inclusion of the $u_i = 0$ point is a significant saving in computing time, since $\chi(0, \theta_k) = 0$ and $\psi(0, \theta_k)$ is related to the complementary error function which can be evaluated quite readily using the exceedingly efficient rational approximation of Hastings.* Thus, the total number of entries to the ψ - and χ -function routine is $(N-1)/2$ for all integrals considered. The purposes of making the rational transformation are manifold. The most obvious purpose is to take advantage of the Lorentzian behavior of $\psi/(\beta + \psi)$ and $\chi/(\beta + \chi)^2$ far away from the origin. Hence, the asymptotic series behavior of the integrands can be eliminated. Of even greater importance from the mathematical point of view is the fact that the transformation amounts to the analytic continuation of the series

$$\sum_{k=0}^{\infty} \alpha_k X^{2k},$$

representing the integrands in X domain; this series does not converge in the limit of large X . The corresponding series

$$\sum_k \gamma_k u^{2k}$$

is believed to converge much more rapidly in the u domain ($0 \leq u < 1$).

By choosing the parameter K appropriately, one may obtain an accuracy of $|\epsilon| < 0.1\%$ for $J(\beta_k, \theta_k)$ and $|\epsilon| < 1\%$ for M and I integrals in the region of practical interest ($\beta_k > 10^{-5}$, any θ_k) by using six points in the summation. For the principal region of interest for fast-reactor applications [$\psi(0, \theta_k)/\beta_k \geq 5$] and the region $\theta \geq 0.5$, only five points or less are required. A detailed report is now under preparation.

(ii) Group Constant Averaging

(a) Application of Space-energy Factorization to Fine-group Neutronics Problems (W. M. Stacey, Jr. and H. Henryson II)

Last Reported: ANL-7753, pp. 103-104 (Oct 1970).

Solution of the neutron diffusion equations by use of the space-energy factorization method has yielded accurate solutions in one- and two-dimensional broad-group problems.** The approximation, based

*C. Hastings, Jr., Approximations for Digital Computers, Princeton University Press, Princeton, N. J. (1955).
 W. M. Stacey, Jr., Solution of the Neutron Diffusion Equation by Space-Energy Factorization, Trans. Am. Nucl. Soc. **13, 739 (1970); also FRA-TM-3, Argonne National Laboratory (Dec 15, 1970). Also, W. M. Stacey, Jr., and H. Henryson II, "Applications of Space-Energy Factorization to the Solution of Static Fast-Reactor Neutronics Problems," Proceedings of Conference on New Developments in Mathematical Models and Applications, American Nuclear Society Mathematics and Computations Division Topical Meeting, Idaho Falls, March 29, 1971 (to be published).

upon a factorization of the flux into a spectral function and a spatial-shape function with weak energy dependence, leads to a set of coupled equations which may be solved by a straightforward iterative process. Because of its computational speed, the space-energy factorization approximation has potential application in fine-group diffusion calculations.

The one-dimensional broad-group space-energy factorization (SEF) code has been extended to accommodate approximately 200 energy groups. As a step in assessing the accuracy of the approximation for fine-group problems, numerical studies for typical one-dimensional fast-reactor models with 166 energy groups have been performed. The fine-group cross-section set used in the studies was generated from ENDF/B Version I data using MC².^{*} The reactivity, detailed spectra, power distributions, and breeding ratios predicted by the space-energy factorization approximation compared favorably with direct solutions of the fine-group equations. The acceleration of the direct solution by use of the converged fission source from the space-energy factorization solution has also been found to be an effective technique. In addition, studies have been initiated to assess the importance of space dependence in the collapsing of fine-group cross sections to a broad-group structure for representative LMFBR configurations.

Table I.B.1 presents results for a four-region slab configuration made up of two core regions containing ²³⁸U, ²³⁹Pu, ²³Na, ⁵⁶Fe, ¹⁶O, a blanket, and reflector. The calculation used Chebyshev acceleration with a k_{eff} convergence of 10^{-7} and were performed on an IBM-360/75. The detailed flux spectra from the 15-shape function solution was also in extremely good agreement with the direct 166-group solution in all regions except the reflector, where the flux was down by approximately two orders of magnitude from the flux in the blanket. In these calculations, no attempt was made to tailor the number of fine groups per shape function interval to

TABLE I.B.1. Results of 15-Shape Function and Multigroup Solutions

Method	k_{eff}	Iteration Time, min	BR ^a
15-shape function space-energy factorization	1.2421	1.2	0.856
166-group direct solution	1.2445	4.1	0.861

$$^a \text{BR} = \frac{{}^{238}\text{U Capture}}{{}^{239}\text{Pu Absorption}}.$$

^{*}B. J. Toppel, A. L. Rago, and D. M. O'Shea, MC², A Code to Calculate Multigroup Cross Sections, ANL-7318 (June 1967).

the particular problem. Rather, an equal number of fine groups was assumed in each interval. The total iteration time for convergence in this problem was reduced by 18% in using the fission source from the space-energy factorization solution as a starting guess for the 166-group solution. Similar problems have been studied in which the savings were as high as 45%.

The results of numerical studies on fine-group problems indicate that the space-energy factorization method may make ultrafine-group (~2000) 1D calculations feasible.

(b) Effect of the 2.85-keV ^{23}Na Resonance on Multigroup Narrow Resonance Cross Sections (W. M. Stacey, Jr.)

Not previously reported.

The contribution of narrow (e.g., uranium and plutonium) resonances to multigroup cross sections depends not only upon these resonances, but also upon the composition of the medium in question. This composition dependence arises from the competition between the resonance and nonresonance "background" reactions, and from the shape of the "asymptotic" flux which weights the contribution of each resonance.

For process x (x = capture, fission) the group cross section is defined.

$$\bar{\sigma}_x \equiv \frac{\int_{\Delta E} \sigma_x(E) \phi(E) dE}{\int_{\Delta E} \phi(E) dE} = \frac{\sum_i \int_{\Delta E} \sigma_x^i(E) \phi(E) dE}{\int_{\Delta E} \phi(E) dE}, \quad (1)$$

where the sum is over all resonances of the sequence (isotope, quantum state) in question which fall within the group. Using the NRA and the single-level formula, Eq. 1 may be approximated as

$$\bar{\sigma}_x \approx \frac{\sum_i (\Gamma_x^i/E_0^i) \sigma_p^i \phi_{as}(E_0^i) J(\theta_i, \beta_i)}{\int_{\Delta E} \phi_{as}(E) dE - \sum_j (\Gamma_j^j/E_0^j) J(\theta_j, \beta_j)} \quad (2)$$

The sum in the denominator is over all resonances of all sequences within the group.

It is convenient in evaluating Eq. 2 to assume that the total "background" cross section per resonance atom (σ_p^i) is the same for all resonances in the sequence and that $\phi_{as} \propto 1/E$. Then Eq. 2 can be evaluated directly. Moreover, the composition dependence of $\bar{\sigma}_x$ is uniquely

characterized by σ_p , which facilitates the construction of tables for rapid cross-section determination such as those proposed by Bondarenko.*

The purpose of this work is to examine the effect of the large sodium-scattering resonance ($\sigma_0 = 912$ eV) at 2.85 keV upon the average group cross section for ^{238}U and ^{239}Pu as given by Eq. 2, and to evaluate the magnitude of the resulting error inherent in the Bondarenko-type cross-section scheme. Resonance parameters for ^{238}U were taken from ENDF/B, and ^{239}Pu parameters were constructed by a statistical ladder technique. Equation 2 was evaluated "exactly," using ϕ_{as} given by continuous slowing-down theory** and an energy-dependent σ_p^i based on the value of the sodium-scattering cross section at each individual narrow resonance.

A qualitative appreciation for the effect of σ_p^i on $\bar{\sigma}_x$ can be obtained by expanding J about its infinite dilution value

$$J(\theta_i, \beta_i) = J(\theta_i, \infty) \left[1 - \frac{2}{\pi \beta_i} \int_0^\infty \psi^2(\theta_i, x) dx + \dots \right], \quad \psi < \beta_i, \quad (3)$$

where β_i is the ratio of σ_p^i to the peak resonance cross section. The second term in Eq. 3, the self-shielding term, becomes negligible at the peak of the sodium resonance and becomes significant in the wings, for mixtures typical of LMFBR cores. The temperature dependence of J is contained entirely in the self-shielding term.

As can be seen from Eq. 2, the effect of the sodium resonance upon ϕ_{as} also influences $\bar{\sigma}_x$.

Two plausible methods were considered in defining an average σ_p to be used over an energy group containing the sodium resonance. In the first method the sodium resonance was simply ignored. (This is consistent with an application of the Bondarenko scheme in which the same σ_p is used for all energy groups.) This would obviously overpredict the self-shielding, hence also the Doppler effect. A second method consists of averaging the sodium-scattering cross section over the group to obtain a value to be used in defining an effective σ_p for the group. This has the effect of under-predicting the self-shielding of those narrow resonances located in the wings of the sodium resonance, without significantly changing the self-shielding of those narrow resonances near the peak of the sodium resonance. Thus, this method underpredicts the self-shielding and hence the Doppler effect.

*I. I. Bondarenko, Ed., Group Constants for Nuclear Reactor Calculations, Consultants Bureau, New York (1964).

W. M. Stacey, Jr., Continuous Slowing Down Theory Applied to Fast-Reactor Assemblies, Nucl. Sci. Eng. **41, 381 (1970).

A series of calculations has been performed to evaluate $\bar{\sigma}_c^{28}$, $\bar{\sigma}_c^{49}$, and $\bar{\sigma}_f^{49}$ for different group structures and compositions typical of LMFBR cores. Several methods were considered for averaging the sodium scattering cross section; the typical results shown in Table I.B.2 are based upon flux weighting with $\phi \propto 1/\xi \Sigma_t$, which yielded the best results. Some appreciation for the significance of these results is obtained by considering that a half-lethargy group about the sodium resonance contributes roughly 10% to the total Doppler effect in a typical LMFBR.

TABLE I.B.2. Percent Errors in Group Average ^{238}U
Resonance Capture Cross Section^a

ΔE , keV	ΔU	$\bar{\sigma}_c^{28}(1000^\circ\text{K}) - \bar{\sigma}_c^{28}(300^\circ\text{K})$			
		$\bar{\sigma}_c^{28}(300^\circ\text{K})$		$\bar{\sigma}_c^{28}(300^\circ\text{K})$	
		1	2	1	2
3.35-3.03	0.10	-21	-1	+216	-16
3.03-2.74	0.10	-26	-4	+431	-5
2.74-2.48	0.10	-22	-1	+109	-9
2.48-2.24	0.10	-27	-4	+53	-7
3.35-2.61	0.25	-42	-8	+251	-18
3.35-2.03	0.50	-27	-8	+43	-22

^aMethod 1 ignores sodium resonance. Method 2 uses averaged scattering cross section to include sodium resonance in σ_p .

The use of an averaged scattering cross section to include the effect of the sodium resonance in σ_p is clearly superior to ignoring the sodium resonance and results in errors that are tolerable for preliminary calculations. This suggests that Bondarenko-type schemes should be used with a group-dependent σ_p which can reflect the presence of the sodium resonance.

b. Fast Critical Experiments--Theoretical Support--Idaho
(189a 02-010)

(i) ZPR Heterogeneity Methods Development (R. G. Palmer)

Last Reported: ANL-7765, pp. 5-7 (Dec 1970).

(a) VIM-I Monte Carlo Code (F. L. Fillmore)

An investigation was carried out to trace the source of the anomalous ^{238}U -to- ^{235}U fission ratio calculated by the VIM-I Code

for ZPPR Assembly 2. This ratio was about 40% higher than the measured value, whereas the standard multigroup-diffusion-theory approach was 7% lower using ostensibly the same source of differential cross-section data, namely, ENDF/B Version I. The investigation revealed an error in the VIM-I cross-section library. The present library contains a constant which is used in determining the neutron energy loss in an inelastic scattering collision where the evaporation model is used. The value of this constant was wrong for all isotopes. After this error was corrected, the 10,000-history calculation for the ZPPR-2 critical assembly was repeated. Table I.B.3 compares the VIM results with corresponding results obtained from multigroup transport and diffusion-theory calculations.

TABLE I.B.3. ZPPR-2 Results Using
ENDF/B Version I Data

Quantity	VIM-I	DOT	2D-Diffusion
k	0.9834	0.9912	0.9888
Probable Error	± 0.0102	---	---
Total Leakage	0.0326	0.0322	0.0365
Total Absorption	0.9693	0.9698	0.9635

The agreement between the VIM and DOT results is well within the statistical errors. Although the VIM result is not converged very well, it has been decided not to make a longer run until the VIM library based on ENDF/B Version II data is available.

Central fission ratios were obtained in the VIM calculation by monitoring the integrated fission rates of five isotopes over the central eighth of the inner-core volume. The results for pairs of isotopes are not statistically independent, because an expected contribution to the fission rate of each isotope is calculated every time there is a collision whether or not a fission event actually occurs. The ratios of fission rates are much more accurate than the rates themselves, due to this correlation in the Monte Carlo method. The results are compared with experimental fission ratios in Table I.B.4.

Standard deviations were not calculated for the VIM results, but it is estimated that F_{49}/F_{25} and F_{41}/F_{25} are accurate to about 1% while F_{28}/F_{25} and F_{40}/F_{25} are accurate to about 5%.

The volume-integrated neutron spectrum was monitored in half-lethargy group structure over the inner core, outer core, inner radial blanket, outer radial blanket, and central portions of each of these regions. For the eight energy groups around the peak of the neutron

spectrum, the standard deviation on the group flux was about 2.5% in the cores, about 3.5% in the inner radial blanket, and about 7% in the outer radial blanket. The standard deviations at higher and lower energies were poorer than this. For the group fluxes integrated over the central portions of these regions, the standard deviations around the peak of the spectrum were about 6, 5, 7, and 10%. These standard deviations would be halved in a run of about 40,000 histories, which would give reasonable accuracy for the core and inner blanket flux and fair accuracy for the outer blanket flux. Although the accuracy obtained in the 10,000-history run is not sufficient to justify presenting a detailed comparison with experimental and multigroup fluxes, no serious disagreement was observed. There is some disagreement which is outside the range of statistical errors, but this might be accounted for by differences between, and shortcomings in, the two calculational methods, as well as imperfections in the basic cross-section data.

TABLE I.B.4. Comparison of Calculated
and Experimental Central Fission
Ratios for ZPPR-2

Quantity	VIM	Exper.	C/E
F_{28}/F_{25}	0.0222	0.0201	1.100
F_{49}/F_{25}	0.9125	0.9372	0.974
F_{40}/F_{25}	0.1816	0.1704	1.060
F_{41}/F_{25}	1.3038	---	---

c. Fast Critical Experiments--Theoretical Support--Illinois
(189a 02-134)

(i) Adjustment of Cross Sections on the Basis of Integral
Measurements (C. E. Till)

Not previously reported.

(a) Cross-section Sensitivity Studies. The main effort has been in adapting the neutron-transport perturbation code DUNDEE* to the IBM-360/75. This code calculates the sensitivity of k_{eff} to changes in various cross sections. Such results are directly useful for planning future critical assemblies as well as for investigating methods of improving cross-section data using integral measurements from fast critical assemblies.

Since the code was developed for the IBM-7030, considerable changes were necessary to make it operable on the 360. A test

*P. C. E. Hemment et al., The Multigroup Neutron Transport Perturbation Program DUNDEE, AWRE-0-40/66 (1966).

problem has been prepared at Aldermaston, and present efforts are directed toward using this test to aid in debugging the code.

The codes SPECTRE* and JINX,** which calculate the sensitivities of spectra and reaction ratios to cross-section changes, have also been obtained from Aldermaston. The next step will be to adapt them to the 360 system.

(b) Evaluation of Data Adjustment Feasibility. A summary report is being prepared on the study of methods of cross-section error identification using integral data from fast critical assemblies. The report details the results of a complete data-adjustment procedure using simulated known results and errors in integral experiments and simulated errors and uncertainties in microscopic cross-section data. Various adjustment procedures are discussed, based upon the use of a one-group zero-dimension model. A paper will also be presented on this work at the Conference on Neutron Cross Sections and Technology, to be held at Knoxville, Tennessee, in March 1971.

2. Experimental Reactor Physics

a. Fast Critical Experiments--Experimental Support--Idaho (189a 02-011)

(i) ZPPR Noise Studies (W. K. Lehto)

Last Reported: ANL-7705, pp. 17-18 (June 1970).

Boron-10 safety-rod worths have been measured in ZPPR Assembly 2 by the low-frequency polarity-coherence function technique[†] using the polarity-correlation equipment recently developed for the ZPPR. (See Progress Report for March 1969, ANL-7561.) The signs of the analog signals derived from each of two detectors is determined by a discrimination circuit and compared in an exclusive-or gate. The ex-or circuit provides a positive logic signal when the inputs are in phase and a negative signal when they are out of phase. These signals instruct a reversing scaler to count external clock pulses up or down. The net result is related to the coherence function by

$$\rho = \sin (\pi C/2),$$

*P. C. E. Hemment et al., The Multigroup Neutron Diffusion Theory Perturbation Program SPECTRE, AWR-0-74/70 (1970).

**B. M. O. Ballance et al., "The Optimization of Neutron Cross Section Data Adjustments to Give Agreement with Spectrum Measurements at the Center of Critical Systems," Proc. Conf. on Physics of Fast Reactor Operation and Design, London, June 23-26, 1969.

†W. Seifritz, The Polarity Correlation of Reactor Noise in the Frequency Domain, Nucl. Appl. & Tech. 7, 513 (1969).

where ρ is the coherence function and C is the ratio of scaler counts to total number of clock pulses. The coherence function is related to reactivity by*

$$\beta = 1 - \left(\frac{\rho_c}{1 - \rho_c} \times \frac{1 - \rho}{\rho} \right)^{1/2},$$

where ρ_c and ρ are the coherence functions measured at critical and subcritical, respectively.

The detectors were placed in the inner core, where the efficiency was expected to be highest. The critical coherence function was 0.976. The various subcritical levels were obtained by inserting ^{10}B safety rods previously calibrated by the inverse-kinetics technique. For comparison, it is assumed that the worths of the individual rods are additive.

Table I.B.5 shows the results, along with the results of the inverse-kinetics technique.

TABLE I.B.5. ZPPR Assembly 2
Subcriticality Measurements

Inverse Kinetics		Polarity Coherence
\$0.064	1.07	\$0.06
\$0.51	1.04	\$0.49
\$0.87	1.02	\$0.85
\$1.40	1.09	\$1.29
\$1.86	1.12	\$1.66
\$2.30	1.09	\$2.12
\$2.83	1.04	\$2.71
1.067		

b. Fast Critical Experiments--Experimental Support--Illinois
(189a 02-013)

(i) Computer Applications (C. E. Cohn)

Not previously reported.

*W. Seifritz, op. cit., see previous page.

(a) A CAMAC Controller for the SEL-840 MP Computer
for Data Collection in Time-of-Flight Experiments
(C. E. Cohn and S. J. Rudnick)

A CAMAC controller has been designed and built for the SEL-840 MP computer to allow the use of on-line data-collection circuits built to the new CAMAC standard to be used with that computer. It was built specifically for the time-of-flight measurements, but is expected to offer great flexibility and convenience for a wide range of applications. It is the first computer-controlled CAMAC system to be operational at Argonne.

The controller is designed for operation of one crate only, with no provision for intercrate communication. If additional crates are added, they will be handled by separate controllers with distinct unit numbers. One crate should be sufficient for the needs of the time-of-flight experiments. All data transfers are programmed; therefore provision is made in the controller for cycle-steal operation, as CAMAC is not readily adapted to that mode. The data rates expected in the time-of-flight experiments are such that programmed data transfers would be entirely adequate.

The standard CAMAC controller enclosure is too small to accommodate, at the rear, the connectors for the computer I/O cable. Therefore, this enclosure has intermediate cables running to an auxiliary chassis mounted in the interface rack. The auxiliary chassis carries the computer connectors in the rear.

3. ZPR-6 and -9 Operations and Analysis

a. Fast Critical Facilities Experiments and Evaluation--Illinois
(189a 02-179)

(i) Clean Critical Experiments (R. A. Lewis)

Last Reported: ANL-7776, pp. 5-7 (Jan 1971).

(a) Central Reactivity Worths Measured in ZPR-6
Assembly 7 (E. M. Bohn)

The reactivity worths of several small cylindrical samples were measured at the center ($r = z = 0$) of ZPR-6 Assembly 7. Measurements were made in the original plate core (see Progress Report for September 1970, ANL-7742, pp. 6-8), in the core containing a central 5×5 drawer section loaded with sodium-filled calandria cans and $\text{PuO}_2\text{-UO}_2$ fuel pins, giving approximately the same homogeneous composition as the plate core; and in the core containing a central 5×5 drawer section

loaded with plates to match exactly the calandria-pin homogeneous composition. There is little difference in the two plate-core central zones, and measurements in these zones are expected to give essentially the same results.

The measurements were made with a pneumatic sample oscillator positioned along Row 23 of the reactor matrix and a calibrated autorod system. The autorod, a 1/4-in.-thick, trapezoidally shaped piece of polyethylene, extending through the 23-24 matrix position in each half, was calibrated by inverse kinetics. The total rod worth was 6.73 lh, with less than 1% maximum differential nonlinearity.

Sample weights and measured worths are listed in Table I.B.6. Gross sample worths for each sample were computed from the oscillator data using the averaging technique of Bennett and Long.* The gross worths were then corrected for the worth of stainless steel cladding and sample holders. The uncertainty for each measurement given in Table I.B.6 includes only the uncertainties due to counting statistics; other sources of error are considered small.

Several samples of boron, two tantalum samples, and two plutonium samples were measured to study flux self-shielding effects in these samples. There appears to be a discrepancy in the two intermediate-weight boron samples; this discrepancy will be investigated.

The reactivity worths in the two plate-core central zones are in good agreement, as expected, except for sodium. The measurements in the central pin zone agree well with the plate-core measurements and indicate a possible few percent difference in the perturbation denominator between the two cases.

(ii) Mockup Critical Experiments (J. W. Daughtry)

Last Reported: ANL-7776, pp. 7-11 (Jan 1971).

(a) Status of ZPR-9 Assembly 27. The FTR engineering mockup, ZPR-9 Assembly 27, is being loaded with fuel for the initial approach to critical.

(b) Reactivity Worths of Material Exchanges in ZPR-9 Assembly 26, Loadings 74-113. During the FTR-3 experiments on ZPR-9, the k_{ex} of the assembly was determined for a great variety of configurations to obtain data on the reactivity worths of peripheral and in-core control rods and on large in-core perturbations simulating test loops of the

*E. J. Bennett and R. L. Long, Precision Limitations in the Measurement of Small Reactivity Changes, Nucl. Sci. Eng. 17, 425-932 (1963).

TABLE I.B.6. Reactivity Worths of Small Cylindrical Samples
Measured at the Center of ZPR-6 Assembly 7

Sample	Sample Weight, g	Specific Worth, Ih/kg		
		Plate Core	Central Pin Zone	Central Matched Plate Zone
Pu ^a	3.524	158.7 \pm 2.3	-	-
Pu ^a	9.956	157.9 \pm 0.9	153.8 \pm 0.6	157.7 \pm 0.25
²³⁵ U ^b	3.084	123.6 \pm 2.0	119.7 \pm 2.3	119.2 \pm 1.04
²³⁸ U ^c	25.988	-9.512 \pm 0.316	-9.023 \pm 0.192	-9.483 \pm 0.104
Ta	8.698	-58.01 \pm 1.46	-54.88 \pm 0.85	-58.07 \pm 1.12
Ta	18.647	-43.07 \pm 0.41	-	-
Boron ^d	0.179	-582.1 \pm 38.7	-	-
Boron	0.483	-507.0 \pm 21.0	-	-
Boron	0.555	-570.3 \pm 11.7	-590.0 \pm 11.7	-571.2 \pm 7.4
Boron	2.345	-494.7 \pm 1.9	-	-
Na	17.044	-4.729 \pm 0.488	-5.398 \pm 0.264	-6.205 \pm 0.315
C	33.441	-12.19 \pm 0.21	-12.54 \pm 0.27	-12.67 \pm 0.27
Al	53.067	-	-	-6.717 \pm 0.168
Fe	33.277	-4.270 \pm 0.156	-3.970 \pm 0.267	-
Ni	37.916	-6.467 \pm 0.185	-6.074 \pm 0.243	-
Cr	26.999	-4.537 \pm 0.370	-4.041 \pm 0.415	-
Mo	43.398	-15.39 \pm 0.11	-	-
Stainless Steel Sample Holder	34.506	-5.034 \pm 0.139	-4.622 \pm 0.090	-4.886 \pm 0.055

^a Composition of sample by weight percent: ²³⁹Pu-85.48, ²⁴⁰Pu-11.39, ²⁴¹Pu-1.93
²⁴²Pu-0.17, Al-1.03.

^b Composition of sample by weight percent: ²³⁵U-93.20, ²³⁸U-6.80.

^c Composition of sample by weight percent: ²³⁵U-0.22, ²³⁸U-99.78.

^d Composition of sample by weight percent: ¹⁰B-19.88, ¹¹B-80.12.
(natural boron)

FTR. The results of these experiments have been tabulated in previous monthly reports. (See Progress Reports for September 1970, ANL-7742, pp. 9-11, and for October 1970, ANL-7753, pp. 14-17.) In this report the data given earlier are consolidated, and the worths of the various configuration changes have been extracted from the k_{ex} data. Figure I.B.1 shows the locations of the various zones of the FTR-3 assembly in which loading changes were made for this series of measurements. Tables I.B.7-I.B.10 list the reactivity worths for all the arrays of control rods and loops that were loaded into the assembly. In addition, at the bottom of each table, is a list of worths obtained indirectly as combinations of the arrays given in the top part of each table. The letters in each table identify the change in composition that was made. These letters are defined in Table I.B.11. In some

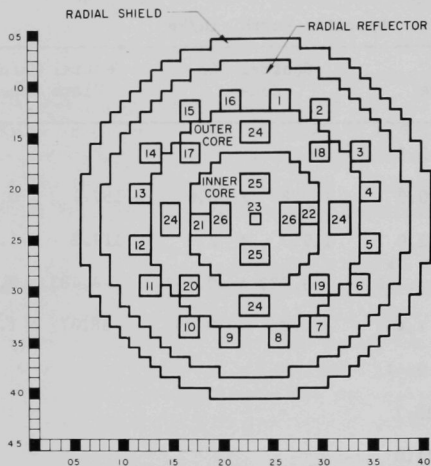


Fig. I.B.1. FTR-3 Assembly Diagram Showing the Locations of Composition Changes in Loadings 74-119

TABLE I.B.7. Loading Exchange Worths for Loadings 74-77

Loading No.	Loading Exchange Zone																				Exchange Worth, Ih	σ , Ih	
	1	2	3	4	5	6	7	8	9	10	11	12	13	14	15	16	17	18	19	20			
74													-B								-92.8	5.1	
75																		-C	-C	-C	-C	-1624.5	45.1
76					A	A							A	A							+1351.2	45.3	
77																		-D			-855.2	80.2	
78	A							A	A								A				+413.0	82.5	
79																				-D	-1015.0	147.4	
80	A							A	A								A				+959.0	150.2	
81																				-D	-1041.0	166.8	
82				A			A					A			A						+881.7	166.3	
83			A					A		A							A				+425.6	34.8	
84																				-D	-1225.3	146.4	
85			A					A		A							A				+399.0	171.0	
86																				B	+335.0	97.5	
87	-A	-A	-A	-A	-A	-A	-A	-A	-A	-A	-A	-A	-A	-A	-A	-A	-A	L	L	L	O	+991.7	40.0
																		-D	-D	-D	-D	-4136.5	278.2
																			-F			-890.3	175.9
																		-L	-L	-L	-L	-5761.0	281.9
																		-L	-L	-L	-O	-5426.0	298.3
	A								A	A							A				+1372.0	171.4	
		A																			+824.6	174.5	
			A		A	A	A														+2232.9	172.4	
	A		A	A	A	A	A	A	A				A	A	A						+2723.2	177.3	
		A	A	A	A	A	A	A	A	A			A	A	A	A	A				+3057.5	245.3	
		A	A	A	A	A	A	A	A	A	A		A	A	A	A	A				+4429.5	299.2	
																		-L	-L	-L	-O	-996.5	422.5

TABLE I.B.8. Loading Exchange Worths for Loadings 88-100

Loading No.	Loading Exchange Zone															Exchange Worth,		σ , Ih	
	2	3	4	5	6	7	10	11	12	13	14	15	21	22	23	Ih			
88														-E	-E		-920.0	41.2	
89										A	A						+659.9	41.3	
90				A	A												+355.2	6.2	
91																	-2219.8	103.1	
92			A	A	A	A			A				A			-D	+1235.3	107.3	
93		A						A	A					A			+997.9	30.3	
94															-F		-1904.2	84.1	
95															-B		-1123.0	182.5	
96		-A	-A	-A	-A	-A	-A	-A	-A	-A	-A	-A	-A	G	G		+2917.4	162.1	
97																-E	-190.0	6.1	
98																-F	-845.4	18.6	
99																-B	-486.0	67.4	
100															-E	-E	G	+529.9	66.2
																G	+1449.9	80.0	
																-D	-3027.2	200.9	
																	-1331.4	69.9	
																-M	-1035.4	19.6	
															-G	-G	-6167.0	229.6	
																-G	-1521.4	70.2	
															-E	-E	-991.5	96.5	
		A	A	A	A	A			A	A	A	A	A				+2250.4	115.1	
		A	A	A	A	A	A	A	A	A	A	A	A	A			+3248.3	119.1	
		A	A	A	A	A	A	A	A	A	A	A	A	-G	-G		-2918.7	258.6	

TABLE I.B.9. Loading Exchange Worths for Loading 101-114

Loading No.	Loading Exchange Zone																				Exchange Worth, Ih	σ, Ih
	1	2	3	4	5	6	7	8	9	10	11	12	13	14	15	16	21	22				
101			B			B					B			B					+322.5	36.9		
102		B					B			B					B				+314.1	35.4		
103																	-I	-I	-1698.5	82.2		
104		H						H			H					H			+658.0	86.9		
105			H				H				H				H				+577.2	32.7		
106		-H	-H				-H	-H			-H	-H			-H	-H			-1286.2	125.8		
107				A	A								A	A					+1339.5	125.8		
108																	-J	-J	-868.5	32.2		
109	A							A	A								A		+1489.1	29.3		
110																		-K	-K	-820.9	31.3	
111			H																+180.3	34.3		
112						H													+194.3	15.5		
113											H				H				+362.5	6.6		
114	-A	-B	-A	-A	-A	-A	-B	-A	-A	-B	-A	-A	-A	-A	-B	-A	M	M	+223.8	6.0		
																			-N	-N	-1689.4	44.9
																			-F	-F	-3387.9	93.7
																			-P	-P	-2567.0	88.3
																			-M	-M	-4307.9	102.3
			B	B			B	B			B	B		B	B				+636.6	51.1		
		H	H				H	H			H	H		H	H				+1235.2	92.8		
			H									H							+737.1	38.2		
			H																+374.6	37.6		
		A						A			A				A				+972.1	93.8		
			A				A				A			A					+899.7	49.3		
		A	A				A				A			A	A				+1871.8	106.0		
	A	A	A	A	A	A	A	A	A	A	A	A	A	A	A	A			+2828.6	129.2		
	A	A	A	A	A	A	A	A	A	A	A	A	A	A	A	A			+4700.4	167.1		
	A	B	A	A	A	A	A	B	A	A	B	A	A	A	A	B	A		+4042.4	142.7		
	A	B	A	A	A	A	B	A	A	B	A	A	A	A	A	B	A	-M	-M	-265.5	175.6	

TABLE I.B.10. Loading Exchange Worths for Loading 115-119

Loading No.	Loading Exchange Zone																Exchange Worth,		σ
	1	2	4	5	7	8	9	10	12	13	15	16	24	25	26	Ih	Ih		
115													-Q			-876.6	12.6		
116	A		<u>A</u>	\bar{A}		A	A		\bar{A}	<u>A</u>		A				+826.5	12.6		
117														-R		-1408.2	37.2		
118		A			A			A				A				+1047.2	37.2		
119															-R	-1555.2	68.1		
														-R	-R	-2963.4	77.6		

TABLE I.B.11. Definitions of Symbols Used to Identify Changes in Composition

Symbol ^a	Composition Removed	Composition Added
A	B ₄ C Control	Radial Reflector
B	B ₄ C Control	Ta Control
C	Safety Rod Channel	Outer Core
D	B ₄ C Control	Safety Rod Channel
E	Safety Rod Channel	Inner Core
F	Ta Control	Safety Rod Channel
G	B ₄ C Control	Inner Core
H	Ta Control	Radial Reflector
I	Ta (25/75)	Safety Rod Channel
J	Ta (50/50)	Ta (25/75)
K	Ta Control	Ta (50/50)
L	B ₄ C Control	Outer Core
M	Ta Control	Inner Core
N	Ta Control	Ta (25/75)
O	Ta Control	Outer Core
P	Ta (50/50)	Safety Rod Channel
Q	Open Loop	Outer Core
R	Closed Loop	Inner Core
S	Closed Loop, Type B	Inner Core
T	B ₄ C Control	Closed Loop, Type B

^aA minus sign before a letter in Tables I.B.7-I.B.10 means the reverse of the composition change identified here.

of the loading changes, only part of a zone was modified. To designate this type of loading change in Tables I.B.7-I.B.10, the following symbols were used: $A|$, $|A$, \underline{A} , and \bar{A} . The symbol $A|$ means that in the left half of the zone, radial reflector composition was substituted for B₄C control; \underline{A} means the same composition change was made in the top half of the zone, etc. The atom densities for each composition are given in the Progress Reports for January 1970, ANL-7661, p. 15; September 1970, ANL-7742, p. 9; and October 1970, ANL-7753, p. 15.

From a survey of the results given in Tables I.B.7-I.B.10, the worths of the various changes are consistent. It is to be expected

that the worth of a given loading change would depend on the configuration of the assembly before the change. However, the worths obtained in these experiments were not strongly dependent on the configurations of the other control rods and loops in the assembly.

(c) Correction of Central Reaction Ratios Reported for FTR-3. New fission-foil mass data necessitate a minor change in the values of the central reaction ratios measured in ZPR-9 Assembly 26 (FTR-3). (See Progress Report for August 1970, ANL-7737, pp. 23-25.) The total mass of the ^{240}Pu detector source should be changed to 60.78 μg . Increased uncertainty in the impurity content of the ^{235}U detector source results in larger error limits for the measured fission ratios. The new values that reflect both these corrections are:

$$^{239}\text{Pu}/^{235}\text{U} \text{ by detector } 0.984 \pm 0.022;$$

$$^{240}\text{Pu}/^{235}\text{U} \text{ by detector } 0.256 \pm 0.006;$$

$$^{238}\text{U}/^{235}\text{U} \text{ by detector } 0.0250 \pm 0.0006.$$

4. ZPPR and ZPR-3 Operations and Analysis

a. Fast Critical Facilities Experiments and Evaluation--Idaho (189a 02-181)

(i) Clean Critical Experiments (P. I. Amundson)

Last Reported: ANL-7776, pp. 11-12 (Jan 1971).

(a) ZPPR Assembly 2 (R. E. Kaiser)

Counter and reactivity traverses have been completed in the radial traverse tube located 14 in. from the interface. Counters used included ^{239}Pu , ^{240}Pu , ^{235}U , ^{238}U , and ^{10}B . Results of the ^{239}Pu traverses in the 3 and 14 in. positions are shown in Fig. 1.B.2, where both curves are normalized to unity at the axial centerline.

Reactivity traverses were made for sodium, ^{238}U , ^{235}U , and plutonium samples of different isotopic compositions, and worths at the axial centerline were measured for samples of typical reactor structural materials. The worth of a ^{252}Cf source was also measured, as a function of radius, at two different power levels. These data were then used to determine an experimental shape for the neutron importance at that position.

A separate experiment was performed to check on the effects of room return on the counter-traverse data. A ^{239}Pu traverse was run with a 1-in.-thick layer of natural B_4C outside the iron reflector. This

shield extended at least 9 in. in all directions from the traverse tube. A reduction of a factor of two was seen in the last count in the reflector, as shown in Fig. I.B.2, indicating the presence of significant room return. The effect disappeared at the reflector/radial-blanket interface, but if a larger boron layer were available, the effects might penetrate more deeply. The results indicate that the measurements made in the iron reflector itself should be treated with reserve. Room-return effects are probably not important in the radial blanket, except possibly in the extreme outer portions.

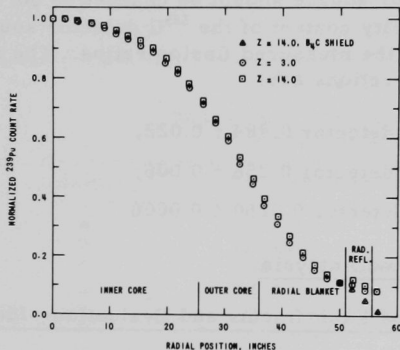


Fig. I.B.2

Radial ^{239}Pu Counter Traverses in
ZPPR Assembly 2, Showing Effects
of Room Return

C. Component Development

1. Instrumentation and Control

a. FFTF Instrumentation Development (R. A. Jaross) (189a 02-025)

Prototypes of permanent-magnet, eddy-current, and magnetometer probe-type flowsensors are being designed, fabricated, and flowtested to establish detailed specifications and design for the FFTF permanent-magnet probe-type flowsensor, and to provide technical guidance to ensure competence in commercial fabrication of probe-type flowsensors. Supporting tests are conducted to determine long-term thermal effects on permanent-magnet materials of interest, and to study the effects of simulated fission-gas release on flowsensor response.

Flowtests and certain supporting tests are conducted in existing facilities (CCTL or CAMEL); new specialized facilities are designed and constructed, as required.

(i) In-core Flowsensors (T. P. Mulcahey)

(a) Permanent Magnet Probe-type Flowsensors (F. Verber)

Last Reported: ANL-7776, p. 14 (Jan 1971).

On January 27, 1971, the Type A-4 $\frac{1}{4}$ Flowsensor (No. 1) was removed from the CCTL after accumulating ~4987 hr of testing in sodium at 1100°F and ~16.4 ft/sec. During this time, the flowsensor output signal decreased from the initial value of ~11.6 to 6.9 mV, or 40.5%.

Subsequent inspection and testing of the flowsensor revealed that the decrease in output signal was due to loss of magnet strength, i.e., structural (material) temperature change or structural plus magnetic irreversible temperature change of the permanent magnet. (The case Alnico VIII magnet had been temperature-stabilized at 1300°F before assembly in the flowsensor.)

The sheathed alumina-insulated electrode-leads cable and the four sheathed magnesium-oxide-insulated thermocouple cables were badly corroded in a 6-in.-long section about 28 in. from the nose of the flowsensor. (This damage was apparently the result of sodium-oxide attack, since a small leak was detected at the thermocouple junctions on the flowsensor guide tube.) However, continuity of the two conductors in the electrode-leads cable was undisturbed. Insulation- and lead wire-resistance tests indicated that the damaged cable did not affect the output signal reading on the Elektronik-19 strip recorder used during testing of the flowsensor in the CCTL.

The Type 304 stainless steel probe guide shaft, and the cable sheaths in the area of the cable faults and toward the flowsensor, evidenced marked ferromagnetic properties. The flowsensor enclosure tube, however, was normally nonmagnetic.

In accordance with instructions for integration of the ANL flowmeter program (ltr. WADCO/FFTF-701530, December 17, 1970) a detailed report of the performance of Type A-4 $\frac{1}{4}$ Flowsensor (No. 1) in the CCTL has been prepared.

(b) Eddy-current Probe-type Flowsensors (J. Brewer)

Last Reported: ANL-7776, p. 14 (Jan 1971).

Eddy-current Probe No. 12 has been operating continuously for over 500 hr in the CCTL in sodium at 1100°F and 525 gpm. The sodium velocity through the probe annulus is approximately 16.4 ft/sec.

The probe was electrically balanced (in air) before installation in the CCTL. After installation, it was again checked for balance before operation. There was no significant change.

On January 27, 1971, the sodium velocity was increased in increments of ~2 ft/sec (holding time: ~1 min/increment), to 16.33 ft/sec from zero flow, and the probe output signal was recorded continuously.

Figure I.C.1 shows the linear relationship between probe output signal and average sodium velocity. Two days later, the output stabilized at ~13 mV for an average sodium velocity of 16.4 ft/sec. This is approximately 1.5 mV higher than the initial output.

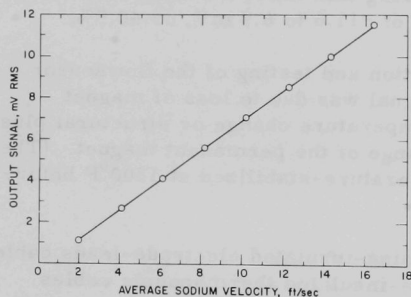
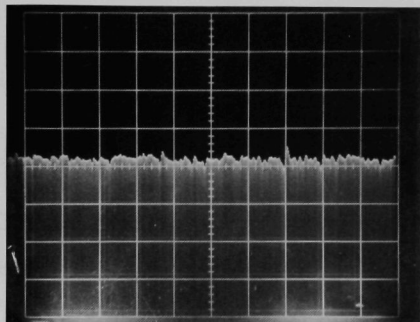
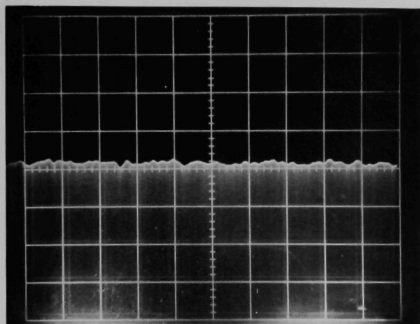


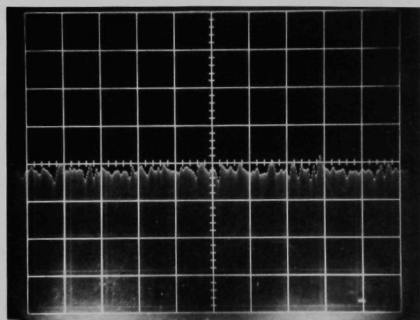
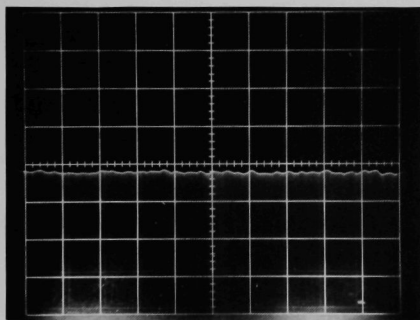
Fig. I.C.1. Output Signal of Eddy-current Flowsensor No. 12 vs Average Sodium Velocity in the CCTL at 1100°F. Drive Current: 500 mA at 1000 Hz.

Gas-injection tests were performed to establish the feasibility of using the eddy-current probe-type flowsensor as a fission-gas burst indicated in support of the FFTF Fuel Failure Location System. These tests were performed at 100% flow (16.4 ft/sec), 75% flow (12.3 ft/sec), and 50% flow (8.2 ft/sec). In each test, argon gas was injected, at a rate of 100 cc/sec for 5 sec, into the center of the sodium stream at a point 14 in. upstream of the probe.

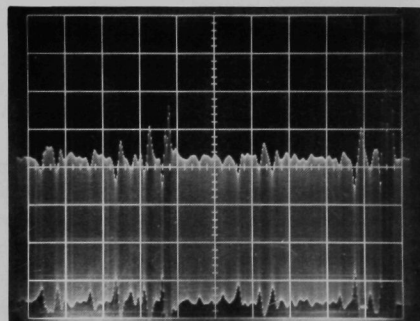
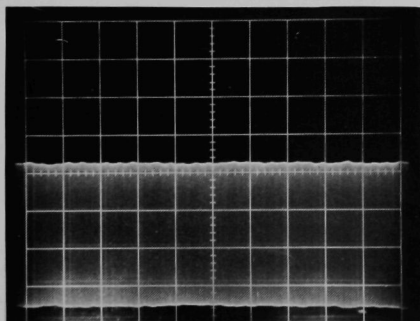
The oscilloscope traces (see Fig. I.C.2) illustrate: (A) normal sodium-turbulence modulation of the output signal without gas injection; and (B) combined sodium turbulence and gas bubble modulation with gas injection. Bubble modulation has higher frequency components



Sodium Velocity = 16.4 ft/sec



Sodium Velocity = 12.3 ft/sec



Sodium Velocity = 8.2 ft/sec

(A)

(B)

Fig. I.C.2. Modulation Component on Output Signal of Eddy-current Flowsensor No. 12: (A) without Gas Injection and (B) with Gas Injection in CCTL in Sodium at 1100°F and Various Sodium Velocities. Drive Current: 500 mA at 1000 Hz; Vertical Sensitivity: 5 mV/cm; Horizontal Sweep: 50 msec/cm; Argon Gas Injection Rate: 100 cc/sec.

than the turbulent modulation, and both the amplitude and percent modulation increase with decreasing flow rate. By comparison, normal sodium-turbulence modulation of the signal decreases with decreasing flow rate.

Spectrum analysis of the flowsensor signal, with and without gas injection, is in progress.

(c) Magnetometer Probe-type Flowsensors (D. E. Wiegand)

Last Reported: ANL-7776, pp. 16-19 (Jan 1971).

There are two sources of spurious signals in an array of magnetometer flowsensors: (a) unbalances in the flowsensor, and (b) improper location or orientation relative to an adjacent flowsensor. Calculations based on a sodium temperature of 1000°F and the proportions of Magnetometer Flowsensor No. 2 (MFS-2) described in ANL-7776 show that:

- (1) A flux-gate off-neutral position of 0.0125 in. produces a flow error of 1 ft/sec.
- (2) Unbalances of 5.05% in magnet moments produce a flow error of 1 ft/sec.
- (3) A sensor 2 in. off axis produces a maximum flow error of 0.490 ft/sec.
- (4) A sensor misalignment of 7.7° produces a flow error of 1 ft/sec.

Items (3) and (4) assume an adjacent sensor on a parallel axis spaced at 4.75 in.

It is not implied that 1 ft/sec is a tolerable flow error; rather, it is chosen as a convenient reference. Except for Item (3), the error in velocity is linear with the magnitude of the source.

Initial unbalances in magnet strengths can be compensated by adjusting the magnet positions (as was done in the tests on MFS-2), or by stabilizing the magnets to the same strength. In the tests on MFS-2, unbalances were not troublesome at temperatures up to 700°F, as the strengths of the two magnets apparently changed almost identically with changes in temperature. Whether the unbalances will become troublesome at higher temperatures depends on the results of stabilization studies in progress and on tests of a high-temperature version of the magnetometer flowsensor.

Items (3) and (4) would appear to pose no problems, except that when one sensor in an array is removed for calibration or

repair, a false dip or rise approaching 0.5 ft/sec in magnitude will appear on flow charts of adjacent sensors as the removed sensor passes the 2-in. position.

The errors generated by Items (3) and (4) could be reduced to very low values by using a gradiometer arrangement consisting of two spaced, oppositely poled flux-gate elements with a suitable balanced array of magnets. Since the sensors and the field sources would be balanced in this arrangement, coupling effects between sensors and sensitivity to stray magnetic disturbances would be greatly reduced. Therefore, if overall length limitations permit, the mechanical and magnetic tolerances associated with Items (1) and (2) could be relaxed by increasing the magnet spacings.

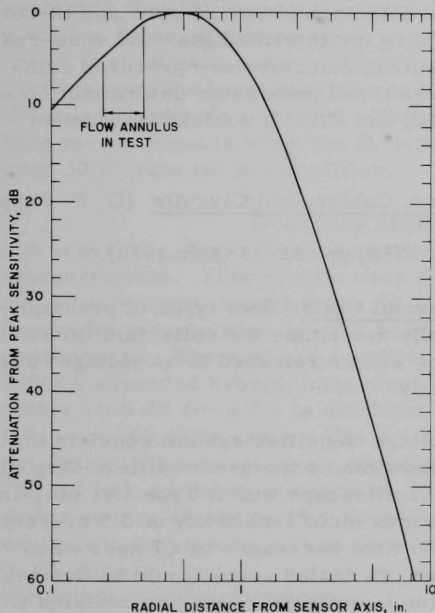


Fig. I.C.3. Calculated Signal-profile Function for Magnetometer Flowsensor No. 2

The signal-profile function (see Fig. I.C.3) shows the relative sensitivity of MFS-2 to fluid velocity at various radii. Only the indicated portion of the curve was applicable to the tests, because of the area limitations of the annular flow channel. The curve shows that for an extended flow region, the radius of maximum response is 0.47 in. out from the axis of the sensor. The location of the peak indicates that the wall thickness of the flowsensor thimble could be increased significantly, with only

a minor loss in sensitivity. Also feasible are various multiple-wall arrangements that might be desired for safety, inert-gas sealing, or other reasons. Furthermore, the effects of velocity-profile variations caused by surface conditions of the thimble wall are reduced by the in-stream location of the response peak.

The signal-profile function indicates the response to flow conditions in the region of adjacent sensors in an array. For example, Fig. I.C.3 shows that the sensitivity to flow at an adjacent sensor spaced at 4.75 in. is 41.3 dB below the peak response. It is evident that the magnetometer flowsensor responds primarily to flow conditions in its immediate vicinity.

b. Neutron-detector Channel Development
(T. P. Mulcahey and G. P. Popper) (189a 02-138)

Development under contract with industrial vendors is focused on complete neutron-detection channels, including cabling and circuitry to transmit, process, and display information from high- and low-temperature ionization chambers and self-powered detectors in out-of-core and in-core regions of LMFBFR's. Advanced circuitry for intermediate- and wide-range applications, and high-temperature neutron detectors are procured commercially; vendor tests are administered; and parameter determination and operational tests are performed in ANL and EBR-II nuclear instrument test facilities.

(i) Out-of-Core Detectors, Cables, and Circuits (G. F. Popper)

Last Reported: ANL-7758, pp. 32-33 (Nov 1970).

(a) Tests on Commercial Units. Two types of preamplifiers are used at ANL to experimentally determine the collection times of fission counters. These preamplifiers will be referred to as voltage- and current-sensitive systems, respectively.

Basically, the voltage-sensitive system consists of an oscilloscope with adequate gain-bandwidth as the preamplifier. Argonne has been using a Tektronix Type 547 oscilloscope with a Type 1A1 plug-in. This scope-plug-in combination has a maximum sensitivity of 0.5 mV/cm, with a rise time of < 20 nsec. The rise time decreases to < 7 nsec when the sensitivity decreases to 50 mV/cm. (A faster scope would be desirable for these measurements.) A small aluminum feedthrough box contains a $0.1\text{-}\mu\text{F}$ decoupling capacitor, rated at 3000 V, connected directly between the fission counter and the Channel 1 oscilloscope input, and a $30\text{-k}\Omega$ bias resistor. The capacitor prevents the detector excitation voltage from being applied to the preamplifier when the fission counter is operated in the unguarded mode. The resistor is connected to the detector excitation input connector and, when combined with the total input capacitance of the detector and other strays, provides a clipping time constant (RC_t) of about $5\text{ }\mu\text{sec}$.

A 50-ohm delay line (~ 100 ft of RG 58/U cable) is connected between the Channel 1 output and the Channel 2 input. The scope is then set to be triggered by the Channel 1 output and thus provides an additional pulse delay of ~ 150 nsec before display. A Polaroid camera is used to record single pulses from the Channel 2 output by using the single-sweep feature of the oscilloscope. The trigger level is set to record only pulses with the largest amplitudes. A pulse is photographed by resetting

the single sweep, opening the camera shutter, and waiting for a pulse to trigger the sweep. After the pulse has triggered the scope, the shutter is closed. Gradicules are then separately recorded on the film. Many such photographs are used to determine the average collection time.

The biggest disadvantage of the voltage-sensitive system is that the input capacitance must be kept small in order to yield a voltage pulse amplitude large enough to be measured. For example, if only 5 ft of 50-ohm cable (~ 150 pF) are used to connect the detector and oscilloscope, the input capacitance is approximately doubled; therefore, the pulse amplitude is halved. The system cannot be used for collection-time measurements when the detector is located in an instrument thimble over 30 ft from the preamplifier.

When long cables between the detector and preamplifier are necessary, the current-sensitive system is used for collection-time measurements. This system uses the same equipment as the voltage-sensitive system, except that a 50-ohm input-output impedance, wide-bandwidth preamplifier is used between the decoupling capacitor and the oscilloscope. The current-sensitive preamplifier is a Hewlett Packard 35002A advanced hybrid, integrated circuit type. It has a gain of 20 dB flat within ± 0.5 dB from 0.1 to 400 MHz, with a typical 3-dB response in the 0.015- to 700-MHz range. The noise rating is < 5.0 dB and therefore does not change the overall scope noise level. The small physical size ($\sim 1/2 \times 7/8 \times 2$ in.), including connectors, makes it convenient to use. A unipolar power source of +24 to 28 V dc is required for this preamplifier. The equivalent conversion gain is ~ 0.6 mV/ μ A when the output is terminated in 50 ohms. A typical neutron pulse will therefore yield about a 2.0-cm deflection on the oscilloscope.

The rise time of the current-sensitive preamplifier is less than 1 nsec, but the combined detector capacitance and preamplifier input impedance limits the pulse rise time to ~ 17 nsec, as stated earlier. This time, coupled with the scope rise time of ~ 20 nsec, gives a total current system rise time of ~ 25 nsec.

The collection times of General Electric Company (GE) Type NA 04, Reuter Stokes Electronic Components, Inc. (RS) Types RSN-314A and RSN-286, and Westinghouse Electric Corporation (W) Types WL-6376, WL-23071, and WX-31384 fission counters were measured. Only the results for the GE Type NA 04 and RS Type RSN-314A counters will be reported at this time.

Two GE Type NA 04 fission counters were available. One (SN/5808524) had $< 1 \times 10^{13}$ nvt integrated dose at the time of these measurements. The other (SN/5477893) had $> 5 \times 10^{17}$ nvt integrated dose; it is presently installed in the J-1 instrument thimble at the EBR-II.

Three RS Type RSN 314A fission counters were available. The first (SN/M1061) had not seen any service and had an estimated $<1 \times 10^{10}$ nvt integrated dose. The second (SN/M1060) had an integrated dose of $<1 \times 10^{13}$ nvt. The third (SN/K1038) is presently installed in the J-3 instrument thimble and has an estimated integrated dose of $>1.2 \times 10^{17}$ nvt.

The GE NA 04 fission counter has a plate spacing of 0.125 in. and is filled with argon-1% nitrogen at 1 atm. The RSN-314A fission counter also has a plate spacing of 0.125 in., but is filled with argon-5% nitrogen at 1 atm.

The results of the collection-time measurements are given in Tables I.C.1 and I.C.2. Eight different voltages were applied to the detectors, so that a range of electron drift velocities would be covered. The tables list the applied voltage, the calculated E/p value, the electron drift velocity w , the calculated collection time T_c , the measured collection time of the unirradiated fission counters $T_{u'}$, and the measured collection time of the irradiated fission counters, T_i .

TABLE I.C.1. Comparison of Collection Times for Irradiated and Unirradiated Type RSN 314A Fission Counters

Applied Voltage, V	E/p , V/cm/mmHg	w , 10^6 cm/sec (Ar-5%N)	T_c , nsec	T_{u1}^a , nsec	T_{u2}^b , nsec	T_i^c , nsec
100	0.41	1.0	310	322	285	191
200	0.83	1.7	187	211	194	167
300	1.24	2.3	138	163	150	149
400	1.66	2.8 ^d	118	155	144	138
500	2.07	3.0 ^d	106	145	129	139
600	2.47	3.0	106	136	128	139
700	2.90	3.0	106	145	126	139
800	3.31	3.0	106	143	127	139

^a Fission counter SN/M1061

^b Fission counter SN/M1060

^c Fission counter SN/K1038

^d Estimated; no data available.

TABLE I.C.2. Comparison of Collection Times
for Irradiated and Unirradiated
GE Type NA 04 Fission Counters

Applied Voltage, V	E/p, V/cm/mmHg	w, 10 ⁶ cm/sec (Ar-1% N)	T _c , nsec	T _u , ^a nsec	T _i , ^b nsec
100	0.41	1.2	265	212	265
200	0.83	2.1	151	184	180
300	1.24	2.3	138	167	156
400	1.66	2.3	138	171	165
500	2.07	2.3	138	164	136
600	2.47	2.3	138	168	168
700	2.90	2.3	138	173	169
800	3.31	2.3	138	170	174

^a Fission counter SN/5808524

^b Fission counter SN/5477893

All measurements were made with the current-sensitive system. The collection times measured on the irradiated detectors may have been influenced by slight reflections noted in the output pulses. These reflections were caused by the mismatch between the 93-ohm cables that were used and the 50-ohm input impedance of the preamplifier. To overcome this problem in the future, an impedance-matching trimmer resistor will be included in series with the decoupling capacitor. It has been shown that an almost perfect match to a 93-ohm cable can be made in this manner.

For purposes of comparison, several collection-time measurements were made, using a 50-ohm cable and a 93-ohm cable between the same fission counter and the preamplifier. There was no significant difference between the respective measured values.

The tabulated values also show there is little, if any, difference between collection times for an irradiated detector and units that have never been exposed to large neutron fluxes. The discrepancies at the lower applied voltages are most likely due to the effects of electron diffusion or incomplete detector saturation. At these voltages, a wider spread in the collection times is noted; therefore, with the finite number of pulses studied, a deviation in the average is more likely.

It can also be shown from these results that both the magnitude and shape of the electron-drift-velocity data found in the literature are fairly accurate. Further studies of the electron drift velocity in the common counter gases should be made at E/p ratios between about 1 and 4 V/cm/mm Hg, and over the entire range of E/p for unusual gas combinations such as helium-xenon.

c. Plant Dynamics and Control Analysis (W. C. Lipinski)
(189a 02-528)

Last Reported: ANL-7776, p. 19 (Jan 1971).

(i) Simulation of Simplified Plant Model on Hybrid Computer.

The programming of the simplified plant model without controllers has been completed and has been checked under steady-state conditions. The program includes analog simulation of the reactor, intermediate heat exchanger, once-through steam generator, reheater, and turbine-generator. The digital computer is used in the simulation of pressure-flow relations and pure time delays in the coolant transport between plant components.

After a dynamic check of the open-loop plant simulation, plant controllers will be added and their effect will be analyzed.

2. Fuel Handling, Vessels, and Internals

a. Core Component Test Loop (CCTL) (R. A. Jaross) (189a 02-026)

The CCTL is operated, maintained, and modified to facilitate long-term tests of prototype FFTF fuel assemblies and in-core instrumentation in sodium under conditions established by the FFTF and LMFBR Programs. Technologies pertinent to sodium-loop operation (e.g., surveillance of sodium and cover-gas quality, and material compatibility, including the Type 304 loop structure) are developed and improved concurrently.

(i) Operation of Loop to Test Second FFTF Subassembly
(F. A. Smith)

Last Reported: ANL-7776, p. 20 (Jan 1971).

As of February 22, 1971, the CCTL has completed a total of 5,803 hr of flowtesting the Mark-II FFTF fuel assembly at 1100°F and ~525 gpm.

During the reporting period, the CCTL accumulated 709.5 hr of flowtesting. On January 27, CCTL flow operations were reduced for 6.5 hr

to permit removal of the Type A-4 $\frac{1}{4}$ Permanent-magnet Flowsensor (No. 1) from the instrument package and to install Eddy-current Flowsensor No. 12. During this period, the mechanical pump was operated to maintain a sodium flow of ~125 gpm for normal fuel-assembly flowtesting and to ensure functioning of the CCTL cold-trap circuit.

On January 28, following installation of the eddy-current flowsensor, flow was reduced for about 5 min to determine and verify that the flowsensor was sensitive to flow reduction. On February 12, the flowsensor was calibrated; this required operation of the main CCTL pump for ~1 hr at a reduced flow rate.

All operations associated with flowsensor removal, replacement, and calibration reflected a CCTL operating factor of 99% for this report period.

A special, 1/2-in. pipe-size sodium loop has been fabricated and designated the CCTL Coolant Surveillance Loop. This loop is designed to: (1) take sodium from the top of the free surface of the CCTL test vessel, (2) circulate the sodium over appropriate metal-surveillance specimens, and (3) return the sodium to the CCTL test vessel. The loop will be operated by the ANL Sodium Technology group to provide basic data related to the coolant quality of CCTL, e.g., carburization potential and oxygen activity. This information will complement data now obtained from the nominal CCTL sodium-sample station. Operation of the loop is separate and independent of CCTL flowtesting.

The Coolant Surveillance Loop has been initially filled with sodium; some difficulty was encountered in establishing constant flow conditions.

Other than the flow reduction associated with flowsensor replacement, there has been no deviation, drift, or other anomaly in the fuel-assembly pressure, flow, or loop vibration-monitoring instruments. The constant records of flowtest variables indicate that the mechanical integrity of the fuel-assembly test has been maintained.

D. Experimental Breeder Reactor No. II--Research and Development

1. Reactor Analysis, Testing, and Methods Development (189a 02-144)

a. Nuclear, Thermal, and Hydraulic Surveillance

Last Reported: ANL-7765, pp. 33-35 (Dec 1970).

(i) Noise Analysis on the EBR-II Intermediate Heat Exchanger (C. C. Price and J. R. Karvinen)

Analysis of the noise data (see ANL-7765) taken on the intermediate heat exchanger (IHX) indicated that the stainless steel drain tube in the secondary-sodium inlet pipe was firmly attached to the stand penetrating the baffles at the bottom of the IHX. Measured resonances of the tube were compared with resonances calculated from two models of the drain tube (see Fig. I.D.1). In one model, the tube was fixed (firmly attached) at both ends; in the other, the tube was fixed at the top, but pinned (free to pivot) at the bottom.

For both the measurements and calculations, the sodium was drained from the IHX and the noise was generated externally. For the calculations, both the upper and lower J-clips (which laterally support the tube) were assumed removed.

Figure I.D.1 shows that the values calculated from the fixed-fixed model compare favorably with the measured values. The values calculated from the fixed-pinned model are significantly below the measured values.

Two other models (Fig. I.D.2) were used to calculate resonances of the drain tube immersed in sodium and fixed at both ends. The noise in this case was generated by flowing sodium. In one model, the tube was also fixed* at the upper J-clip; in the other, it was pinned at the clip. The values calculated from the second model compare favorably with the data taken at the various flow levels on November 17, 1970, the Monday after the unusual noises in the IHX were first noticed (see Fig. I.D.2 and Table I.D.1).

The calculations were made using the equation** for free-vibration resonances (f_n) of a beam

$$f_n = \frac{\lambda_n^2}{2\pi\ell^2} \sqrt{\frac{EI}{\rho A}}, \quad (1)$$

*"Fixed" in the sense that a moment such as that generated by a rigidly embedded beam section was assumed.

This moment was assumed to be transmitted to the upper part of the tube.

**W. Flügge, Handbook of Engineering Mechanics, 1962 Edition, pp. 61-9 and 62-8, McGraw-Hill, New York.

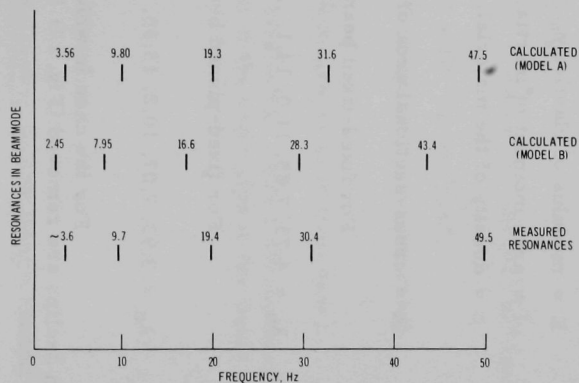
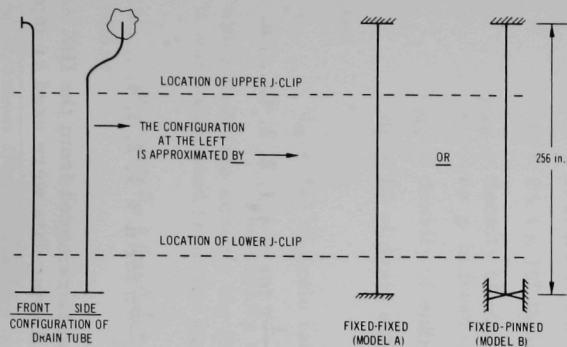


Fig. I.D.1. IHX Drain Tube with Sodium Drained and Both J-clips Removed

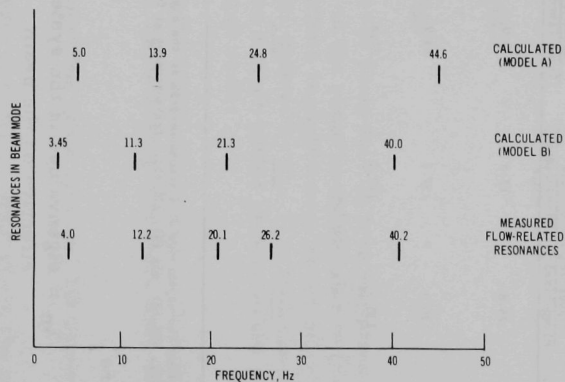
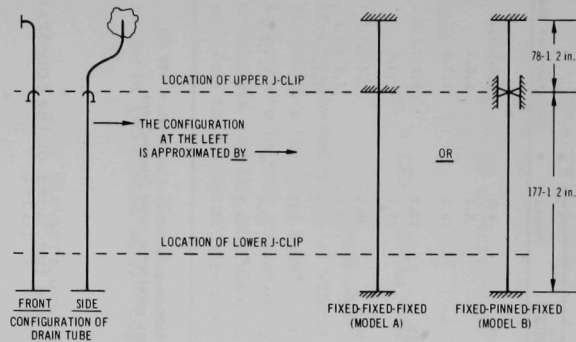


Fig. I.D.2. IHX Drain Tube Immersed in Sodium, with Upper J-clip in Place and Lower-J-clip Removed

TABLE I.D.1. Comparison of Calculated and Measured Resonances of Drain Tube When IHX Is Filled with Sodium

Mode, n	Frequencies, Hz				Measured	Appearance vs Flow ^a
	Upper 78½ in. of Tube		Lower 177½ in. of Tube			
	Fixed-Fixed	Fixed-Pinned	Fixed-Fixed	Pinned-Fixed		
1	25.8	17.8	5.0	3.45	4.0	1,2,3,4,5
					8.1	1,2,3
					10.1	1,2,5
2	70.7	57.2	13.9	11.25	12.2	1,2,3,4,5
					15.1	1,3,4
3	130	112.0	24.8	21.34	20.1	1,2,3,4,5
					26.2	1,2,3,4,5
					35.0	1,3,4,5
					36.2	1
4	----	----	44.6	40.0	40.2	1,2,3,4,5
					44.2	1
					48.2	1

^a Indicates the appearance of a resonance peak in the spectra for the following secondary-flow levels: 79% (1), 70% (2), 60% (3), 45% (4), 27% (5). Peaks present at 0% flow were not considered to be flow-related.

where

λ_n = eigenvalues of the system, which are functions of the constraints effective on the beam,

ℓ = distance between restraints,

E = modulus of elasticity,

I = area moment of inertia,

ρ = density of the material,

and

A = cross-sectional area of the beam.

For fixed-fixed beam ends,

$$\lambda_n = 4.73, 7.85, 11.0, 14.1, \dots, \sim \frac{2n+1}{2} \pi \text{ for } n = 1, 2, 3, 4, \dots, n.$$

For fixed-pinned beam ends,

$$\lambda_n = 3.93, 7.07, 10.2, 13.35, \dots, \sim \frac{4n+1}{4} \pi \text{ for } n = 1, 2, 3, 4, \dots, n.$$

For the case in which sodium is removed from the IHX and both J-clips are removed (Fig. I.D.1), the following data were used as input for Eq. 1:

ℓ = length of drain tube = 256 in.,

$E = 29 \times 10^6 \text{ lb/in.}^2$ at 72°F ,*

ρ = density of stainless steel = $7.42 \times 10^{-4} \text{ lb-sec}^2/\text{in.}^4$,

d_i = ID of drain tube = 0.875 in.,

and

d_o = OD of drain tube = 1.00 in.

Visual observation of the drain tube in free vibration showed the preferred mode of vibration to be in the plane perpendicular to the plane containing the pipe bend. The calculations reported were based on this plane. Use of the higher vibrational modes (as defined by Eq. 1) in both the measurements and the calculations provides a much better picture of the phenomena than use of only the fundamental mode.

For the case in which the IHX is filled with sodium (and the noise is generated by flowing sodium), the following data were used as input for Eq. 1:

ℓ_1 = distance between the top of the drain tube and the upper J-clip = $78\frac{1}{2}$ in.,

ℓ_2 = distance between the upper J-clip and point where the pipe is fixed to the stand penetrating the baffles = $177\frac{1}{2}$ in.,

$E = 23.3 \times 10^6 \text{ lb/in.}^2$ at 600°F ,*

ρ_{ss} = density of stainless steel = $7.42 \times 10^{-4} \text{ lb-sec}^2/\text{in.}^4$ (same as ρ in first case),

ρ_{Na} = density of sodium = $8.1 \times 10^{-5} \text{ lb-sec}^2/\text{in.}^4$,

d_i = ID of drain tube = 0.875 in. (same as in first case),

and

d_o = OD of drain tube = 1.00 in. (same as in first case).

The density actually used in Eq. 1 was a pseudodensity, which took into account the immersion of the drain pipe in the liquid sodium. It was calculated from the equation

$$\rho = \rho_{Na}A_0 + \rho_{ss}A_{ss}, \quad (2)$$

where

A_{ss} = cross-sectional area of the drain tube

*C. W. Andrews, Effect of Temperature on the Modulus of Elasticity, Metal Progress 58(1), 85-100 (July 1950).

and

$A_0 = \frac{\pi}{4} (d_0^2 + d_1^2)$, which accounts for the sodium set in motion by the pipe vibration.

This configuration is not as simple as the one for the empty IHX. It involves many approximations, such as:

(1) Representation of the pipe and sodium as a free system. Actually, (a) the sodium provided a viscous damping effect and (b) the drain tube was continuously being excited by the sodium flow and was dissipating energy in a random manner by contacting the wall of the inlet pipe.

(2) Representation of the upper J-clip as either a fixed or a pinned point. Subsequent investigation has shown that the upper clip was loose and allowed the drain tube to rub radially against it.

(3) Assumption that the upper section of the tube acted solely as a stiff transmitter rather than as a flexing member. This approximation becomes complicated and uncertain near resonance modes of the upper section of the tube.

The calculated resonance modes for the pinned-fixed condition of the lower portion of the tube correlate reasonably well with measured modes at all flows of the secondary-system except zero flow, and appear to be flow-dependent.

(ii) Modification of Irradiation Conditions in EBR-II for Subassembly XX03 (L. B. Miller and R. E. Jarka)

Over the past two years, methods have been developed to analyze the detailed spatial variations in neutron- and gamma-flux levels that occur in heterogeneous reactors.* These methods have been used to investigate the degree to which irradiation conditions can be modified in a small region of the core and to define a core-loading pattern tailored to provide a specified gamma-flux level in a particular experimental subassembly. The results of the investigations show that it is feasible to reduce the gamma-flux level 77% in an experimental subassembly. In the modified core loading, the gamma-heating rate in the stainless steel components of the subassembly will be 39% less than that in the same position in the unperturbed core.

The experimental-irradiation subassembly of interest (XX03, an instrumented subassembly) was designed for neutron irradiation at a controlled temperature that is to be attained by gamma heating of the

*L. B. Miller and R. E. Jarka, Detailed Analysis of Space-Dependent Phenomena, Trans. Am. Nucl. Soc. 13(1), 307 (June 1970).

subassembly components. To achieve the correct temperature, the gamma flux in the subassembly must produce approximately 3.8 W/g in iron.

Detailed distributions of gamma-heating rate in EBR-II have recently been obtained by using an energy-balance technique* to normalize distributions of rates of gamma-energy generation calculated with a transport-theory code. Used in the calculations were 22-group neutron-transport and 20-group photon-transport cross-section libraries, which have been checked by comparison with experimental data for ^{235}U and ^{238}U fission rates, control-rod worths, and melt-wire temperatures. The results of the calculations indicated that if XX03 were located in its intended position in the unmodified EBR-II reactor grid, with the reactor operating at its design power of 62.5 MWt, the gamma-heating rate would be 47% too high (5.6 W/g in iron).

Transport-theory analyses show that the local reactor environment can be modified to accommodate XX03 by surrounding XX03 with subassemblies containing half as much fuel as driver subassemblies do.

The maximum variation in the core loading that might possibly be made--taking into consideration the necessity of maintaining a critical core configuration and avoiding excessive flux asymmetry that could lead to local overheating of some fuel subassemblies--is to surround XX03 with subassemblies filled with stainless steel. Neutron- and gamma-transport analyses show that with this variation the gamma-heating rate in iron is reduced to 1.29 W/g in XX03. The gamma-heating rates in other subassemblies in the perturbed sector of the reactor are reduced about 30%. In other sectors, the gamma-heating rates are increased 4 to 20%. The distributions of neutron flux, fission rate, and gamma source are distorted in a similar manner and to approximately the same degree.

The results of this study show that it is feasible to modify irradiation conditions significantly for a limited number of experiments. However, large modifications (e.g., a 70% reduction in the gamma-flux level) can only be obtained by severely distorting the distributions of flux and fission rate in the entire reactor.

(iii) Thermal Effect of Modifying Core Environment for Subassembly XX03 (R. A. Cushman)

An analysis has been carried out to determine the thermal environment for driver-fuel and experimental-irradiation subassemblies in an EBR-II core modified to accommodate experimental instrumented subassembly XX03. The results indicate that the radial fission-rate distribution

*L. B. Miller and R. E. Jarka, The Distribution of Gamma Energy Deposition in a Fast Reactor, Trans. Am. Nucl. Soc. **13**(2), 831 (Nov 1970).

is similar to that for 62.5-MWt cores studied previously. The subassembly temperatures are within the range of those covered in ANL-7743.*

Results of core neutronics were obtained for the core given in Fig. 12 of ANL/EBR-035.** This core loading was described as that for the optimum modification of local environment for XX03 (see Sect. I.D.1.a(ii) above). The POWER subroutine of the DOT code was used to give the relative power production in each subassembly. From this, the radial relative fission rate was determined for effective driver subassemblies in each type core position, and relative fission rate versus radius was plotted. The radial distribution of fission rate and the number of effective subassemblies in each type core position were then used as input for a POWDIST calculation. From this was obtained the power per effective subassembly and the bulk outlet temperature for each type core position. These powers and temperatures are compared in Table I.D.2 with similar data for the 69-effective-subassembly core of ANL-7743. The maximum temperatures are lower for the core modified to accommodate XX03, which contained 68.8 effective subassemblies.

TABLE I.D.2. Results of POWDIST Calculations for
Two Reactor Loadings at 62.5 MWt

Type of Core Position	Power per Subassembly, kW		Bulk Outlet Temp, °F	
	Optimum Core for XX03 ^a	Core with 69 Effective Subassemblies ^b	Optimum Core for XX03 ^a	Core with 69 Effective Subassemblies ^b
1A1	1046	1032	892	889
2A1	1039	1020	890	887
3A1	984	996	905	907
3A2	1006	1011	910	911
4A1	861	886	945	952
4A2,3	912	931	959	964
5A2,4	769	805	958	970
6A1	579	597	923	930
6A2,5	634	655	944	952
6A3,4	663	690	956	966

^aFig. 12, ANL/EBR-035.

^bFrom ANL-7743.

*R. R. Smith, W. B. Loewenstein, and C. M. Walter, The EBR-II: A Status Report, ANL-7743 (to be published).

**L. B. Miller and R. E. Jarka, Local Modification of Irradiation Conditions, ANL/EBR-035 (to be published).

A comparison was also made of the power produced in fueled experimental subassemblies for two different core loadings shown in ANL/EBR-035: Fig. 1 (a typical EBR-II core loading) and Fig. 12 (the core for optimum modification of local environment). In making the comparison, we used the outputs of two different POWER calculations, one for each core. The fission power in each subassembly was compared with that of a driver subassembly in position 1A1 (set arbitrarily equal to 1.000 in both cores). The results are compared in Table I.D.3 together with (in the righthand column) the ratio of the power produced by a fuel experiment in

TABLE I.D.3. Relative Power Production in Experimental Subassemblies in Two Cores at 62.5 MWt

Core Position	Subassembly No.	Typical Core ^a		Optimum Core ^b for XX03 ^b		Ratio of Normalized Values (Optimum/Typical)
		Value from POWER Code	Normalized to 1A1	Value from POWER Code	Normalized to 1A1	
1A1	Driver	0.8078	1.000	0.3598	1.000	1.000
3C1	X107	0.9487	1.174	0.4055	1.127	0.960
4B2	X079	0.5463	0.6763	0.2446	0.6798	1.005
5A2	X051	0.1629	0.2016	0.0631	0.1754	0.870
5D2	X083	0.4010	0.4964	0.1812	0.5036	1.014
5E2	X082	0.4038	0.4999	0.1835	0.5100	1.020
5B4	X087	0.5265	0.6518	0.2221	0.6173	0.947
5C4	X093	0.7370	0.9124	0.3126	0.8688	0.952
5D4	X097	0.5650	0.6994	0.2400	0.6670	0.954
6B1	X055	0.2211	0.2737	0.0983	0.2732	0.998
6F1	X073	0.2087	0.2583	0.0800	0.2223	0.861
6A2	X086	0.2608	0.3228	0.1097	0.3049	0.994
6C2	X056	0.4327	0.5356	0.1901	0.5283	0.986
6B3	X078	0.2386	0.2954	0.1115	0.3099	1.049
6C3	X059	0.2879	0.3564	0.1229	0.3416	0.958
6D3	X069	0.1970	0.2439	0.0866	0.2407	0.987
6E3	X054	0.4241	0.5250	0.1821	0.5061	0.964
6A4	X088	0.1364	0.1688	0.0576	0.1601	0.948
6B4	X096	0.4928	0.6100	0.2163	0.6012	0.986
6C4	X071	0.2669	0.3304	0.1230	0.3418	1.035
6D4	X043	0.4395	0.5441	0.1888	0.5247	0.964
6E4	X084	0.2676	0.3313	0.1147	0.3188	0.962
6A5	X074	0.4134	0.5117	0.1819	0.5055	0.988
7B1	XG04	0.0155	0.0192	0.0071	0.0197	1.026
7D1	X075	0.2064	0.2555	0.0929	0.2582	1.010
7C3	X062	0.3641	0.4507	0.1610	0.4475	0.993
7E3	X072	0.1224	0.1515	0.0546	0.1518	1.002
7F4	X088	0.1841	0.2279	0.0659	0.1832	0.804
7B6	X058	0.3461	0.4284	0.1534	0.4263	0.995
7C6	X081	0.1247	0.1544	0.0550	0.1529	0.990
8B2	X036B	0.0771	0.0954	0.0353	0.0981	1.028
8D2	XG03	0.0134	0.0166	0.0061	0.0168	1.012
8E2	X036A	0.0954	0.1181	0.0416	0.1156	0.979

^aFig. 1 of ANL/EBR-035.

^bFig. 12 of ANL/EBR-035.

the modified core to that produced in the typical core. Inspection of this column reveals that in only three cases (X051 in position 5A2, X073 in 6F1, and X088 in 7F4) is there more than a 6% difference between the two powers. The agreement between the data for the two cores is probably slightly better than indicated by Table I.D.3, because the difference between the number of effective subassemblies in each core was not considered when the power in position 1A1 was normalized to 1.000. The modified core had 68.8 effective subassemblies, the unmodified typical core 67.4.

Modification of the local environment around position 5F3 so that XX03 can be located there will have negligible effect on all other driver and fueled experimental subassemblies, except three experimental subassemblies located close to the local perturbation.

(iv) Analysis of Temperatures and Mixing of Coolant in Subchannels of EBR-II Instrumented Subassembly XX01
(R. A. Cushman)

Included in the instrumentation in experimental subassembly XX01, the first instrumented subassembly to be used in the EBR-II instrumented-subassembly system,* were seven thermocouples measuring coolant temperatures: four spacer-wire thermocouples and three outlet-coolant thermocouples. The spacer-wire thermocouples were butt-welded to the 0.041-in.-dia spacer wires, which were wrapped at a 6-in. pitch around the nineteen 0.357-in.-dia capsules in the subassembly. Their junctions were 8.6 in. above the bottom of the fuel in the 13.5-in.-high core. The junctions of the outlet-coolant thermocouples were at the top of the capsules, 20 in. above the top of the core, but within the channel formed by three adjacent capsules. Figure I.D.3 shows the layout of the instrumentation and the composition of the subassembly. Sixteen capsules contained UO_2 fuel elements operating at approximately 8 kW/ft; the other three capsules produced little heat.

Temperatures of the coolant channels through and up to 20 in. above the core were calculated using the HECTIC** code as modified at EBR-II. For the calculations, the subassembly was divided into two halves about the line to the core center, and each half was subdivided into 22 coolant subchannels and 65 surfaces. The YEDH factor in HECTIC, which can be considered as a mixing factor, was varied to provide good agreement between the measured and calculated temperatures at both the height of the junctions of the spacer-wire thermocouples and of the outlet-coolant thermocouples. As shown in Table I.D.4, a YEDH of 65, which

*A. Smaardyk, C. J. Divona, and E. E. Hutter, The Instrumented Subassembly System in EBR-II, Nucl. Technol. 10, 139-159 (Feb 1971).

**N. Katchee and W. C. Reynolds, HECTIC-II, An IBM 7090 FORTRAN Computer Program for Heat Transfer Analysis of Gas or Liquid Cooled Reactor Passages, IDO-28585 (Dec 1965).

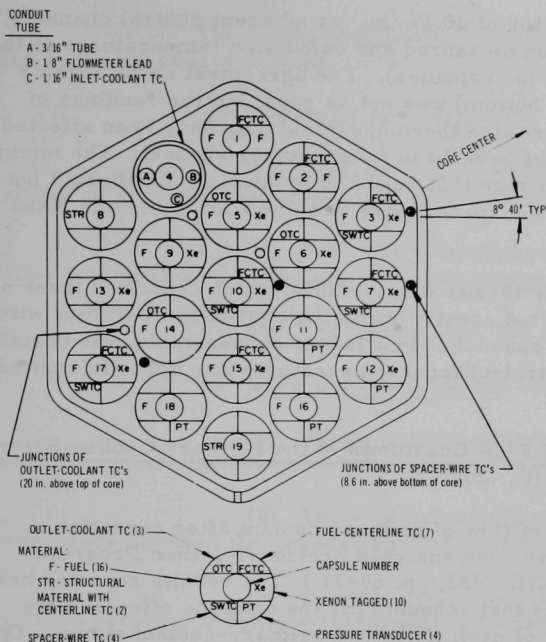


Fig. I.D.3

Arrangement of Capsules and Instrumentation in Instrumented Subassembly XX01.
ANL Neg. No. IF-103-05464 Rev. 1.

TABLE I.D.4. Effect of YEDH Factor on Calculated Subchannel Temperatures in EBR-II Subassembly XX01^a

YEDH Factor	Spacer-wire TC No.				Outlet-coolant TC No.		
	3	7	10	17	5	6	14
<u>Calculated Temperatures, °F</u>							
5	784	768	843	824	847	908	864
15	780	771	842	818	838	883	841
25	779	774	841	813	831	864	830
35	779	776	840	809	826	850	823
45	779	778	838	806	824	841	820
55	780	780	836	803	822	835	817
65	781	781	834	801	821	831	816
<u>Measured Temperatures, °F</u>							
--	790	775	830	824	824	826	815

^aBased on operation of subassembly at 142 kW, during 50-MWt reactor operation, in EBR-II run 39A.

corresponds to a mixing factor of 20.6%/in. for adjacent central channels, gave good agreement between measured and calculated temperatures at the latter location (at the top of the capsules). The agreement at the former location (8.6 in. above core bottom) was not as good, but the readings of these thermocouples (spacer-wire thermocouples) may have been affected by their "seeing" coolant just brought in from another channel. The mixing factor of 20.6%/in. is higher than that reported by Marian and Hines,* but the pitch/diameter ratio of the spacer-wire wrap was lower for the XX01 bundle (1.115 versus 1.28).

Even in this 19-rod subassembly, which contained three non-fueled capsules, mixing did not greatly affect the coolant temperature within the fueled length in central channels. In a larger subassembly, one containing 91 to 217 elements, central-channel temperatures are apt to be unaffected by mixing.

(v) Analysis of Flow Coastdown of the Primary Cooling System in EBR-II (D. Mohr)

Coastdown of flow of primary coolant after cessation of power at the pump motor has been analyzed previously. (See Progress Report for October 1970, ANL-7753, pp. 69-71.) The results reported here are for an extended analysis that accounts for the dynamic effects of the motor-generator (M-G) set of each of the two primary-coolant pumps. One of the cases analyzed (see Fig. I.D.4) could be compared directly with recent measurements;** because this comparison is favorable (within 8%), considerable confidence is placed in the coastdown model used for the extended analysis.

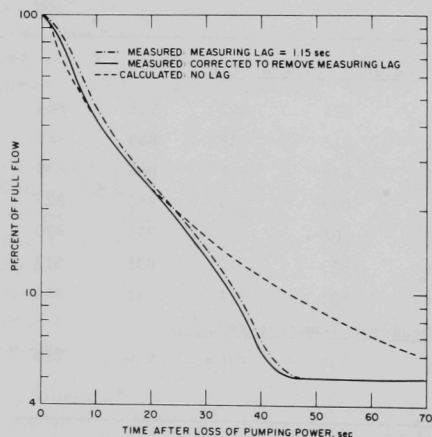


Fig. I.D.4

Calculated and Measured Coastdown of Flow of Primary Coolant Following Mode-2 Loss of All Primary Pumping Power; Auxiliary Pump Operating

*V. R. Marian and D. P. Hines, Transfer of Coolant between Adjacent Subchannels in Wire Wrap and Grid Spacer Rod Bundles, Trans. Am. Nucl. Soc. 13(1), 807 (Nov 1970).

**Guide for Irradiation Experiments in EBR-II, Rev. 4, Appendix E, EBR-II Project document (Feb 1971).

The model is divided into several submodels derived from the following considerations.

(a) Motors of M-G Sets

- (1) Each motor is a squirrel-cage induction type and offers no electrical retarding torque after it loses power.
- (2) Power is simultaneously cut off to both M-G sets. (The model, however, can also simulate power interruption to a single unit.)
- (3) The dynamics of the two sets are identical.

(b) Eddy-current Clutches (one per unit)

- (1) Ninety percent of the transmitted torque is proportional to the product of a "slip function" and the effective field current.*
- (2) The slip function is a nonlinear relationship of the difference between the speeds (slip) of the input and output shafts.*
- (3) The effective field current lags the applied field voltage because of voltage-to-current and current-to-torque transfer functions.*
- (4) Ten percent of the total torque transmitted is due to the hydraulic-coupling effect of the cooling-water circuit within the clutch.

(c) Generators

- (1) Each generator is a synchronous machine excited by an external exciter driven by each M-G motor. (The excitation system was recently changed; generator excitation is now provided by a separate dc power supply at constant voltage.)
- (2) The output voltage of each generator is proportional to the product of generator speed and excitation voltage.
- (3) The load torque is proportional to the transmitted power divided by generator speed.
- (4) The current in each integral generator and pump-motor circuit can be determined by analyzing the equivalent electrical circuit whose impedance depends upon generator frequency.**
- (5) Windage and friction losses are negligible.

*Information supplied ANL by Dynamatic Division of Eaton Yale and Towne, Inc. (Apr 1969).

**A. F. Puchstein and T. C. Lloyd, Alternating-Current Machines, Chapters V, XXIII, and XXXI, Wiley and Sons, New York (1936).

(d) Pump Motors

- (1) Each pump motor is a squirrel-cage induction type.
- (2) The resistance and reactance of each stator and rotor are part of the integral electrical circuit with the generator.
- (3) The equivalent load resistance is a nonlinear function of slip of the pump motor; the resistance decreases as slip increases.*
- (4) The output torque is a function of: the square of the applied voltage; the slip; and the equivalent impedance.*
- (5) Friction and windage losses are negligible.

(e) Pump Equations and System Friction Losses

- (1) The equations for steady-state pump head and torque hold during the transient.
- (2) Both primary pumps are described by identical equations (although power loss to a single pump can also be simulated).
- (3) The developed head of the primary auxiliary pump varies linearly with flow rate.
- (4) The pressure drop through all components of the primary system is approximately proportional to the 1.85 power of flow rate.
- (5) Effects of shaft and fluid inertia are included.
- (6) Effects of natural convection are excluded.

The effect of the natural driving head is excluded in this treatment, because it has essentially no effect on the initial flow transient. A separate dynamic model for natural convection has been developed, however, and will be described in a subsequent report.

The model consisted of 43 equations--including 10 first-order differential equations and 22 nonlinear equations--which were programmed on the CSMP** code for the IBM-360.

After a detailed checkout and a parametric-sensitivity study were conducted, several cases simulating loss of electrical power were run. First, however, three distinct modes of power loss, for both pumps, were recognized:

*A. F. Puchstein and T. C. Lloyd, op.cit., previous page.

**System/360 Continuous System Modeling Program, User's Manual, H20-0367-3, IBM (Oct 1969).

Mode 1: Loss of 2400-V power to M-G motor (clutch remains energized).

Mode 2: Total loss of power to M-G set (both the 2400 V to the motor and the 480 V to the eddy-current clutch).

Mode 3: Direct loss of power to pump motor (e.g., opening of generator circuit breaker).

All three modes of power loss are physically possible in the plant, Mode 3 being the least probable, and Mode 2 appearing to be the most probable.

The following transients were then analyzed:

(1) Loss of both pumps simultaneously for Modes 1, 2, and 3, with auxiliary pump not operating.

(2) Loss of both pumps simultaneously for Modes 2 and 3, with auxiliary pump operating.

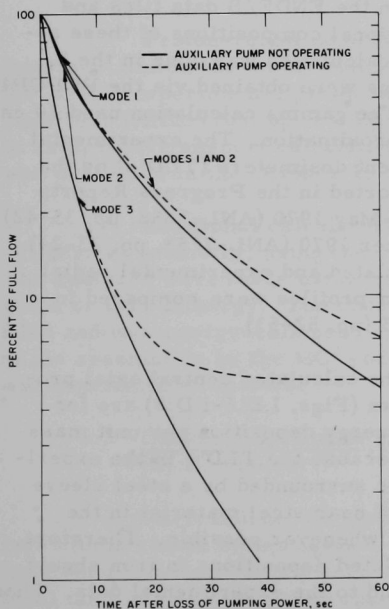


Fig. I.D.5. Calculated Coastdown of Flow of Primary Coolant Following Mode-1, -2, and -3 Loss of Primary Pumping Power

The results for Mode-2 loss are compared directly with the most recent coastdown measurements (April 1970) in Fig. I.D.4.

Great care must be taken when comparing "measured" with "calculated" results, since the flow measurements inherently contain a known measuring lag of about 1.15 sec. In Fig. I.D.4, we see that: (1) the effect of this lag is significant; and (2) calculated and measured results compare closely when this lag is included in the analytical model. Figure I.D.5 shows calculated results without this measuring lag, both with and without the auxiliary pump operating.

Of the many parameters contained in this dynamic model, some could not be accurately determined. The study of parameter sensitivities showed one of these parameters to be significant: the pump torque load due to shaft friction. All the final results were determined with one best estimate of this effect.

Of the parameters that could be determined with reasonable accuracy, the mode of power failure, the shaft inertia, and the flow-measuring lag were the most important. The lag is especially significant; because of it, the actual flow rate through the core is 5 to 25% less than the measured flow rate during the early stages (first 6 sec) of the transient.

2. Characterization of Irradiation Environment (189a 02-151)

Last Reported: ANL-7765, pp. 47-57 (Dec 1970).

(Experimental results for the EBR-II experiments on ZPR-3 discussed here are reported in Sect. I.B.4, "ZPPR and ZPR-3 Operations and Analysis.")

a. Axial Gamma-deposition Profiles for ZPR-3 Assemblies 60, 61, and 62 (D. G. Stenstrom and D. Meneghetti)

Two-dimensional, RZ-geometry calculations of gamma depositions in ZPR-3 Assemblies 60, 61, and 62 have been made with the DOT transport code and compared with experimental values. The analysis utilized 29-group cross sections based on the ENDF/B data files and energy-collapsed specifically for the regional compositions of these assemblies by the MC² code. The neutron calculation was done in the S_4 approximation, and the gamma productions were obtained via the POPOP4 code* and POPOP4 yield-data library. The gamma calculation used 20 energy groups and was done in the S_8P_3 approximation. The experimental values were obtained by thermoluminescent dosimeters (TLD's) by the ZPR-3 experimental group and were reported in the Progress Reports

for April-May 1970 (ANL-7688, pp. 35-42) and October 1970 (ANL-7753, pp. 23-24). The calculated and experimental radial deposition profiles were compared in ANL-7765 (pp. 52-53).

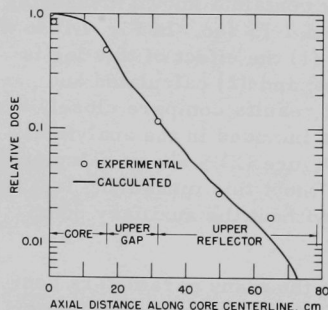


Fig. I.D.6

Comparison of Calculated Axial Gamma-deposition Profile for ZPR-3 Assembly 60 with Experimental Values Obtained with Thermoluminescent Dosimeters

The calculated central axial profiles shown (Figs. I.D.6-I.D.8) are for gamma-energy deposition per unit mass of iron, because the TLD's in the experiment were surrounded by a steel sleeve and placed near steel material in the assembly whenever possible. Therefore, the calculated depositions in iron should correspond to the experimental data. These figures show a good agreement between the calculations and experiments in the axial direction.

*W. E. Ford III and D. H. Wallace, POPOP4: A Code for Converting Gamma-ray Spectra to Secondary Gamma-ray Production Cross Sections, CTC-12, Union Carbide Corporation, Nuclear Division, Computing Technology Center (May 1969).

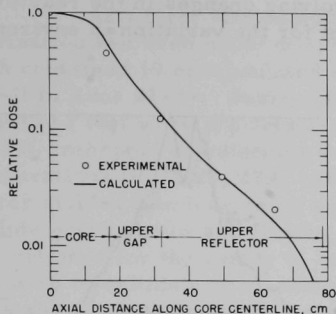


Fig. I.D.7. Comparison of Axial Gamma-deposition Profile for ZPR-3 Assembly 61 with Experimental Values Obtained with Thermoluminescent Dosimeters

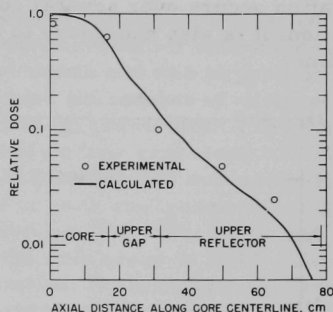


Fig. I.D.8. Comparison of Axial Gamma-deposition Profile for ZPR-3 Assembly 62 with Experimental Values Obtained with Thermoluminescent Detectors

b. Calculated Fine-energy Flux Spectra in ZPR-3 Assembly 61
(D. G. Stenstrom, K. E. Phillips, and D. Meneghetti)

Proton-recoil measurements at core center, at core-reflector interface, and in the nickel reflector in ZPR-3 Assembly 61 were made by the ZPR-3 experimental group and reported in the Progress Report for June 1970 (ANL-7705, pp. 33-35). A comparison of the experimental results of an S_4 DOT transport calculation in RZ geometry with 29 energy groups was presented in the October 1970 Progress Report (ANL-7753, pp. 90-91).

Additional calculations have been made in one-dimensional cylindrical geometry, using the code ANISN* with the diffusion-theory option. The analyses were made using a 165-group cross-section set with a group width of $1/10$ lethargy. The cross-section set was based on ENDF/B data files and was energy-collapsed specifically for the regional compositions of the assemblies by the MC² code. Figure I.D.9 compares the calculated and experimental spectra.

c. Characterization of Environment of Subassembly X012 in EBR-II
(G. H. Golden)

Correlations for predicting fast-flux-induced swelling of stainless steels can be tested against observed swelling in subassemblies that have been irradiated in EBR-II. To do this, it is necessary to specify the level (and in some cases the spectrum) of the flux as well as the power generation throughout the volume of interest during the irradiation. For a given run, both core-wide and local flux effects must be considered. If the

*W. W. Engle, Jr., A Users Manual for ANISN, A One Dimensional Discrete Ordinates Transport Code with Anisotropic Scattering, K-1693, ORNL (Mar 1967).

irradiation occurs over several runs involving changes in the reactor configuration, it is also necessary to account for the variation in environment with time.

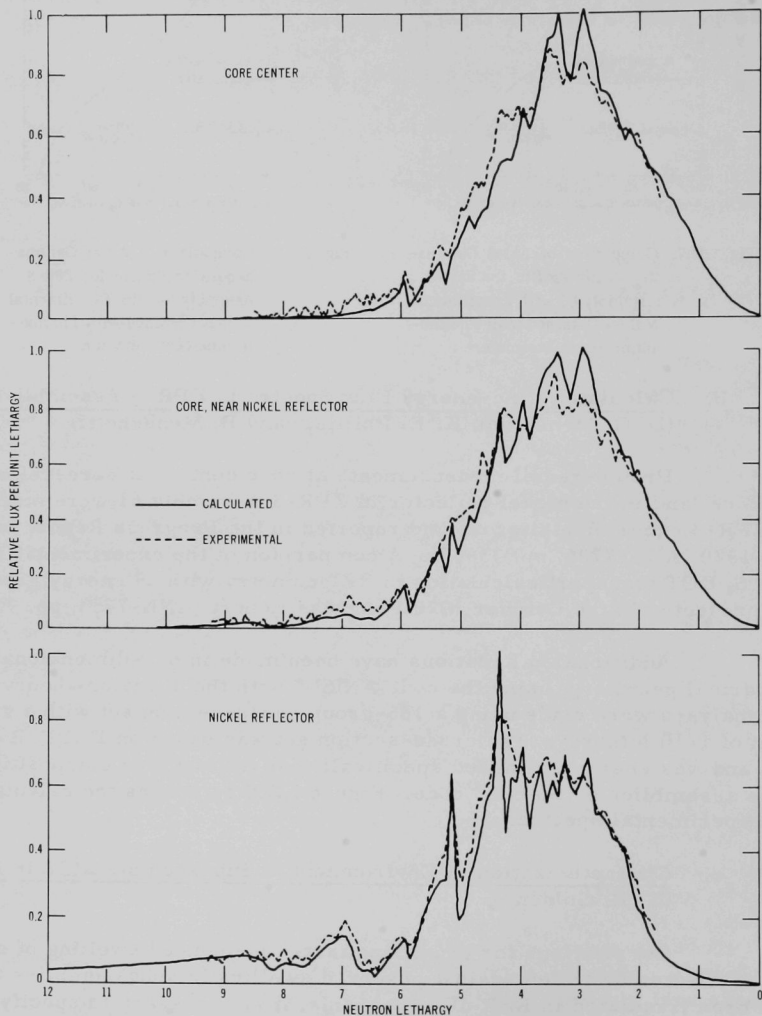


Fig. I.D.9. Comparison of Calculated Spectra with Experimental (proton-recoil) Spectra at Various Positions in ZPR-3 Assembly 61

As a first step in making these correlations, a detailed characterization has been made of experimental-irradiation subassembly X012, which contained 19 encapsulated oxide elements and was in position 4B2 of EBR-II in Runs 21-37. During this interval, the number of adjacent subassemblies that were not drivers ranged from one to three. Two-dimensional (X-Y) S_2 transport calculations were made on four representative reactor configurations (Runs 24, 27A, 29D, and 31F), with each subassembly in the reactor divided into four equal areas. For each configuration, midplane absolute group fluxes and fission densities for ^{235}U , ^{238}U , ^{239}Pu , and ^{240}Pu were obtained for the center of each of the four areas in X012. These values were used to estimate, for each configuration, the midplane absolute group fluxes and fission densities in a given capsule in the subassembly. These fluxes and fission densities were then averaged on the basis of the number of MWd spent in configurations similar to each of the four representative ones.

Two-dimensional (R-Z) S_2 transport calculations were used to estimate relative axial distributions of total flux and fission densities for ^{235}U , ^{238}U , ^{239}Pu , and ^{240}Pu . The absolute distributions of flux and fission densities over the length of a given capsule were determined from the midplane absolute values and the relative axial distributions. The power in each of 20 axial nodes was calculated by multiplying the average fission rate per gram of each of the four heavy nuclides in the node by its mid-irradiation mass in the node and summing the four products so obtained. The midirradiation masses were obtained from burnup corrections on initial masses.

Table I.D.5 gives the results of these calculations for Capsule C-17 of Subassembly X012.

TABLE I.D.5. Average Total Flux and Power in Capsule C-17 of Experimental Subassembly X012

Axial Node	Total Flux, $10^{15} \text{ n/cm}^2\text{-cm}$	Midlife Fission Rate, $10^{13} \text{ fissions/sec}$				Total
		^{235}U	^{238}U	^{239}Pu	^{240}Pu	
1 ^a	1.64	1.584	0.007	0.454	0.011	2.056
2	1.75	1.649	0.009	0.482	0.012	2.151
3	1.85	1.714	0.010	0.508	0.013	2.245
4	1.96	1.777	0.011	0.534	0.014	2.336
5	2.04	1.839	0.012	0.556	0.015	2.421
6	2.12	1.891	0.012	0.575	0.016	2.494
7	2.17	1.934	0.012	0.589	0.016	2.552
8	2.22	1.965	0.013	0.602	0.017	2.596
9	2.24	1.986	0.013	0.608	0.017	2.624
10	2.26	1.994	0.013	0.611	0.017	2.635
11	2.25	1.992	0.013	0.611	0.017	2.633
12	2.23	1.986	0.013	0.601	0.017	2.616
13	2.20	1.988 ^b	0.012	0.571	0.016	2.587
14	2.15	1.948	0.012	0.559	0.015	2.534
15	2.09	1.901	0.011	0.543	0.015	2.469
16	2.01	1.843	0.011	0.523	0.014	2.392
17	1.92	1.774	0.010	0.501	0.013	2.298
18	1.82	1.701	0.009	0.474	0.012	2.196
19	1.70	1.629	0.008	0.445	0.011	2.093
20	1.57	1.554	0.007	0.417	0.010	1.988

^aCore bottom.

^bHigher ^{235}U mass in this and subsequent nodes.

3. Operation of Data Acquisition System (DAS) (189a 02-530)

Last Reported: ANL-7753, p. 95 (Oct 1970).

a. Development of Programs

(i) Measurement of Transfer Function (E. W. Laird)

A series of programs that measure transfer function by insertion of the pseudorandom binary (PRB) signal has been written and checked out.

The PRB signal is generated on a digital output line from the Sigma 5 computer. The analog input equipment is used to sample the output signal of the system under analysis. This output data is stored on magnetic tape. Subsequent programs perform the following:

- (a) Average four frames of PRB output.
- (b) Cross-correlate the PRB input and the output from the system under measurement.
- (c) Perform a Fourier Transform of the data from step 2.
- (d) Plot the Fourier Transform against the log of frequency on the Calcomp plotter.

The plot from step d is a measure of the transfer function of the system to be analyzed. Measurements made in this way on operational amplifiers with known transfer functions have agreed well with expected values.

(ii) Display of Critical Parameters (K. D. Tucker)

An overlay program has been developed to display critical parameters to reactor operators on the alphanumeric scopes of the DAS. The parameters to be displayed are:

- (a) Nuclear power
- (b) Primary-system heat balance
- (c) Reactor ΔT
- (d) Reactivity
- (e) Outlet temperature of subassembly in position 2C1
- (f) Outlet temperature of subassembly in position 3B1
- (g) Outlet temperature of subassembly in position 2A1
- (h) Outlet temperature of subassembly in position 4C3
- (i) Inlet bulk-sodium temperature

- (j) Secondary-system heat balance
- (k) Steam-system heat balance
- (l) Measured secondary-system flow
- (m) Error in measured secondary-system flow
- (n) Electrical power

The current parameters will be displayed along with the time of day every 30 sec.

PUBLICATIONS

Functional Description of the EBR-II Digital Data Acquisition System

J. M. Allen,* R. W. Hyndman, R. A. Call, E. W. Laird, M. R. Tuck, and K. D. Tucker

ANL/EBR-029 (Nov 1970)

The Influence of a Predominantly Oxide Fuel Loading on the Dynamic Behavior of EBR-II

A. V. Campise

ANL-7673 (Oct 1970)

Transformation Kinetics of U-5 wt % Fs Driver-fuel Pins Produced by Aerojet General Corporation

A. K. Chakraborty

ANL/EBR-032 (Nov 1970)

Performance of the ANL Dynamitron Tandem

S. A. Cox and P. R. Hanley**

Bull. Am. Phys. Soc. 16, 227 (Feb 1971) Abstract

Status of Important Heavy-Element Nuclear Data above the Resonance Region

W. G. Davey

Proc. 2nd Int. Conf. on Nuclear Data for Reactors, Helsinki,
June 15-19, 1970, Vol. 2, pp. 119-135

Analysis of Compton Continuum Measurements

R. Gold and I. K. Olson

ANL-7611 (Feb 1970)

Meltdown Analysis of Various EBR-II Core Configurations Using the MELT-II Code

G. H. Golden and R. H. Shum

ANL-7752 (Nov 1970)

*Division of Reactor Development and Technology, USAEC.

**Radiation Dynamics, Inc.

Prompt-neutron Spectra and Delayed-neutron Spectra from Fission: Some
Comments on Current Knowledge

Arthur H. Jaffey

ANL-7747 (Nov 1970)

A Code for Calculating Effluent Air Temperatures from a Sand Filter

G. K. Rusch

ANL-7687 (Nov 1970)

Design, Analysis, and Construction of EBR-II Primary Tank and Associated
Structures

R. W. Seidensticker

ANL-6922 (Sept 1970)

Investigation of the Thermodynamics of V-O Solid Solutions by Distribution
Coefficient Measurements in the V-O-Na System

D. L. Smith

Met. Trans. 2, 579-583 (Feb 1971)

Performance of a 4 MeV Dynamitron with a Heavy Ion Source

Anthony Taylor

Bull. Am. Phys. Soc. 16, 225 (Feb 1971) Abstract

II. GENERAL REACTOR TECHNOLOGY

A. Applied and Reactor Physics Development

1. Theoretical Reactor Physics

a. Theoretical Reactor Physics (189a 02-081)

(i) Cross-section Data Evaluation (E. M. Pennington)

Last Reported: ANL-7758, p. 62 (Nov 1970).

Data testing using Version-II ENDF/B data in calculating fast-reactor benchmark assemblies has been completed. MC² problems were run for six assemblies, and were followed by S_n transport or diffusion-theory calculations to yield values of k_{eff} and activation ratios, and by perturbation-theory calculations to obtain central worths and delayed neutron-dependent quantities. The values of k_{eff} so obtained are given in Table II.A.1.

TABLE II.A.1. Values of k_{eff} Using Version-II ENDF/B Data

Assembly	k_{eff} (Version II)	k_{eff} (Modified Version II)
Godiva	1.00117	-
ZPR-3-6F	0.99264	1.00794
Vera 1B	0.98926	0.99999
Jezebel	0.98870	-
ZPR-3-48	0.96135 ^a	0.99385*
Zebra 3	0.94897	-

^aDiffusion theory. (An S_4 calculation would give $k_{eff} \sim 0.0065$ higher.)

The first three assemblies in the table are fueled with ²³⁵U; the last three are ²³⁹Pu assemblies. The values of k_{eff} are generally too low, especially for the ²³⁹Pu assemblies.

A task force meeting was held at Brookhaven National Laboratory in early February to consider the problem of low k_{eff} values. It was decided to modify some cross sections at the broad group level and to redo the transport or diffusion-theory calculations using the modified data. The cross-section changes involved increases in fission cross sections for ^{239}Pu , ^{235}U , and ^{238}U over various energy ranges, and a decrease in the capture cross section of ^{238}U . Also, the fission spectra were modified somewhat. The results for the assemblies assigned to Argonne for recalculation are given in the last column of Table II.A.1. As expected, these modifications led to increases in k_{eff} and better agreement with experiment. It was felt at the Brookhaven meeting that the cross-section changes were within the experimental error bounds of the differential data.

(ii) Neutronics Computational Capability

Last Reported: ANL-7758, pp. 62-64 (Nov 1970).

(a) Application of Space-energy Factorization to Two-dimensional LMFBR Diffusion-theory Calculations
(W. M. Stacey, Jr.)

The basic idea of the space-energy factorization (SEF) method, which is to represent the neutron flux as the product of a purely energy-dependent spectral function, $\rho(E)$, and a spatial function, $\psi(r,E)$, with weak energy dependence, was presented elsewhere.* An iterative procedure for sequentially improving ρ and ψ was presented and some numerical results for one-dimensional, 24-group representations of LMFBR's were given. Subsequently, the method was applied to one-dimensional, many-group problems and to two-dimensional, 24-group problems, and some early results of these calculations have been reported.** A detailed study of the application of SEF to the solution of two-dimensional, 24-group neutron-diffusion problems in realistic LMFBR models is in progress.

In these studies, SEF has been integrated into the conventional outer-inner iteration strategy, so that a comparison with standard procedures can be made. A power iteration scheme, with two-term Chebyshev extrapolation, was used for the outer iterations of the 24-group flux. (It was necessary to devise a consistent method for accelerating the spatial functions of the SEF.) The inner iterations consisted of using the

*W. M. Stacey, Jr., Solution of the Neutron Diffusion Equation by Space-Energy Factorization, Trans. Am. Nucl. Soc. 13, 739 (1970).

**W. M. Stacey, Jr., and H. Henryson II, "Applications of Space-Energy Factorization to the Solution of Static Fast-Reactor Neutronics Problems," Proc. Conf. New Developments in Mathematical Models and Applications, Idaho Falls, 1971 (to be published).

most recently calculated shape function for each energy interval to spatially average group constants to use in the calculation of the spectral function for that interval. This spectral function was then used to collapse the 24-group equations to $N < 24$ equations for the shape functions. The same shape function was assumed to be appropriate for all the energy groups within a given shape-function interval. The equation for each shape function was then solved by an ADI-B² scheme similar to that proposed by Hageman and Yasinsky,* with one sweep in each direction per inner iteration.

Three types of questions were examined with regard to SEF: (1) What was the trade-off of accuracy versus computing time, relative to a conventional multigroup solution? (2) How effective was SEF in accelerating a conventional multigroup solution by providing a good fission-source guess? (3) How much better is SEF than the simpler, but less consistent, strategy of initially collapsing to a few groups using a critically buckled core spectrum? Representative results are shown in Tables II.A.2 and II.A.3 for a reactor model with composition typical of an LMFBR at initial startup. In general, it is concluded that SEF provides an economical approximate solution suitable for many design and analysis applications, and provides an excellent means of accelerating an exact solution.

TABLE II.A.2. Comparison of Space-Energy Factorization and Conventional Few-group Results

Calculation ^a	k_{eff}	Breeding Ratio ^b					Power Fraction, %			
		Total	Axial Blanket	Radial Blanket	Core 1	Core 2	Axial Blanket	Radial Blanket	Core 1	Core 2
24-group	1.0381	1.16	0.31	0.20	0.50	0.15	1.3	0.9	64.6	32.8
2 SF	1.0295	1.11	0.26	0.19	0.50	0.16	2.6	1.9	62.3	32.7
4 SF	1.0361	1.13	0.28	0.20	0.50	0.16	1.7	1.2	63.9	32.8
6 SF	1.0390	1.14	0.29	0.20	0.50	0.16	1.4	0.9	64.3	33.0
2-group ^c	1.0510	1.12	0.26	0.20	0.49	0.16	3.0	2.3	62.1	32.2
6-group ^c	1.0419	1.14	0.29	0.20	0.50	0.16	1.4	0.9	64.3	33.0

^aSF = Number of shape function intervals.

^bRegion BR's are defined as the ²³⁸U capture rate in region divided by the total ²³⁹Pu destruction rate in the reactor.

^cFew-group calculations used a critically buckled spectrum from a Core 1 medium to collapse group constants.

(b) Spatial Synthesis (V. Luco)

A highly nonseparable Merriman type problem (see Progress Report for April-May 1970, ANL-7688, p. 158) was used to study the following questions:

(1) How much asymmetry is introduced into the solution of this highly symmetric problem by the use of asymmetric interface conditions at the synthesis boundaries?

*L. A. Hageman and J. B. Yasinsky, Comparison of Alternating Direction Time-Differencing Methods with Other Implicit Methods for the Solution of the Neutron Group-Diffusion Equations, Nucl. Sci. Eng. 38, 8 (1969).

TABLE II.A.3. Comparison of Computing Times

Calculation	Outer Iterations	CPU ^a Time, min
24-Group	15	10.90
24-Group/2 SF ^b	7	7.05
24-Group/6 SF	7	8.10
2 SF	15	2.05
6 SF	16	3.10

^aCentral Processing Unit, IBM 360-50/75, including edits.

^b24-group calculation used initial fission source from 2 SF calculation. Computing time includes 2 SF calculation.

continuity interface was introduced at the midpoint along the length of the cell. With the same set of trial functions on both sides of the interface, synthesis calculations were performed using in turn symmetric and asymmetric interface conditions. The effect in k_{eff} is small, typically about 0.1%. The flux asymmetry introduced by the asymmetric interface conditions is clear, up to a few percent of the flux values in some situations.

(2) An unexpected outcome of this investigation is the finding that for this configuration the results of the synthesis calculation using the symmetric interface conditions (in which the flux and current continuity conditions are weighted with the mean value of trial functions on both sides of the interface) are extremely sensitive to the ordering of the trial functions used. This feature is, of course, absent when asymmetric weighting is employed.

Typically, if on one side of the interface a set of trial functions, let us say 1, 2, 3 is used, and an antisymmetric set of 1', 2', 3' is used on the other half of the cell, and the pairing at the interface is 1-1', 2-2', 3-3', the flux obtained in the synthesis direction (perpendicular to the interface) is flat; that is, all the mixing functions are constant, and the k_{eff} value is totally in error. This "cylindrical error" can be removed by changing the pairing of trial functions at the interface, in other words, by changing the ordering of the trial functions in one of the synthesis regions. Unfortunately, in some cases, different reorderings of the functions, while eliminating the "cylindrical error" and giving more reasonable values for k_{eff} , still differ widely among themselves. For example, in one case, the following results were obtained:

Cylindrical error case with pairing 1-1', 2-2', 3-3':	$k_{\text{eff}} = 1.4096.$
Pairing 1-3', 2-2', 3-1':	$k_{\text{eff}} = 1.1658.$
Pairing 1-2', 2-1', 3-3':	$k_{\text{eff}} = 1.1430.$

(2) How sensitive are the results obtained to the ordering of the trial functions used, in the case of symmetric interface conditions at the synthesis boundaries?

The computations were carried out in six energy groups using the ARC system computational module SYN2D. The results obtained are as follows:

(1) The characteristics of the Merriman cell make it particularly suitable to test the effects of introducing an asymmetric set of synthesis interface conditions into the synthesis equations. A discontinuity

These results, based on an atypical model chosen to accentuate the influence of the effects studied, provide qualitative insight into problems which may be encountered in the application of spatial synthesis to realistic LMFBFR models. A report is in preparation.

(c) A Fast-reactor Spectrum in a Thermal Core
(H. Greenspan and J. C. Carter)

Work is continuing on the development of calculational methods for designing and analyzing the currently proposed tests of fast-reactor fuel elements in thermal reactors. A primary interest is the computation of the fine-mesh fission distribution over the cross sections of individual mixed-oxide fuel elements in heterogeneous assemblies surrounded by a filter or converter. Some calculations have been made and substantiated by measurements.*

A primary objective in testing assemblies of fast-reactor fuel elements in thermal cores is to minimize the fission gradient over the cross section of individual rods by using filters or converters. The same total power per rod is achieved by varying enrichment, inversely as the distance from the center of the assembly.**

Discrete-ordinate transport theory is used to find the spectral shift as rings of elements are added to heterogeneous test assemblies, and to determine the skewness of the fission distribution brought about because of the significant effect of self-shielding among elements in small heterogeneous assemblies.

R-Z geometry is used to determine the total fission distributions and the buckling. With the information from this R-Z calculation, an external source calculation in X-Y geometry with fine mesh in the test section is made to determine the fission distribution over the cross sections of individual fuel rods and the effect of self-shielding.

Figure II.A.1 shows the variation in calculated and measured fission density over the cross section of rods 1A, 2B, and 3C in a test assembly of 19 enriched UO_2 elements.

(iii) Reactor Computation and Code Development (B. J. Toppel)

Last Reported: ANL-7776, pp. 47-56 (Jan 1971).

(a) The MC²-2 Code. Coding is proceeding on the new cross-section code MC²-2 in the areas of: library preparation; resolved

*E. W. Barts, J. C. Carter, M. V. Davis, and R. A. Morris, Measurement of Fission Distribution in an Assembly of 19 Fast-reactor Fuel Elements, (to be published as an ANL topical report).

**C. N. Kelber, Rule of Thumb for Fast Flux Irradiations, Nucl. Appl. 6, 6 (1969), letter.

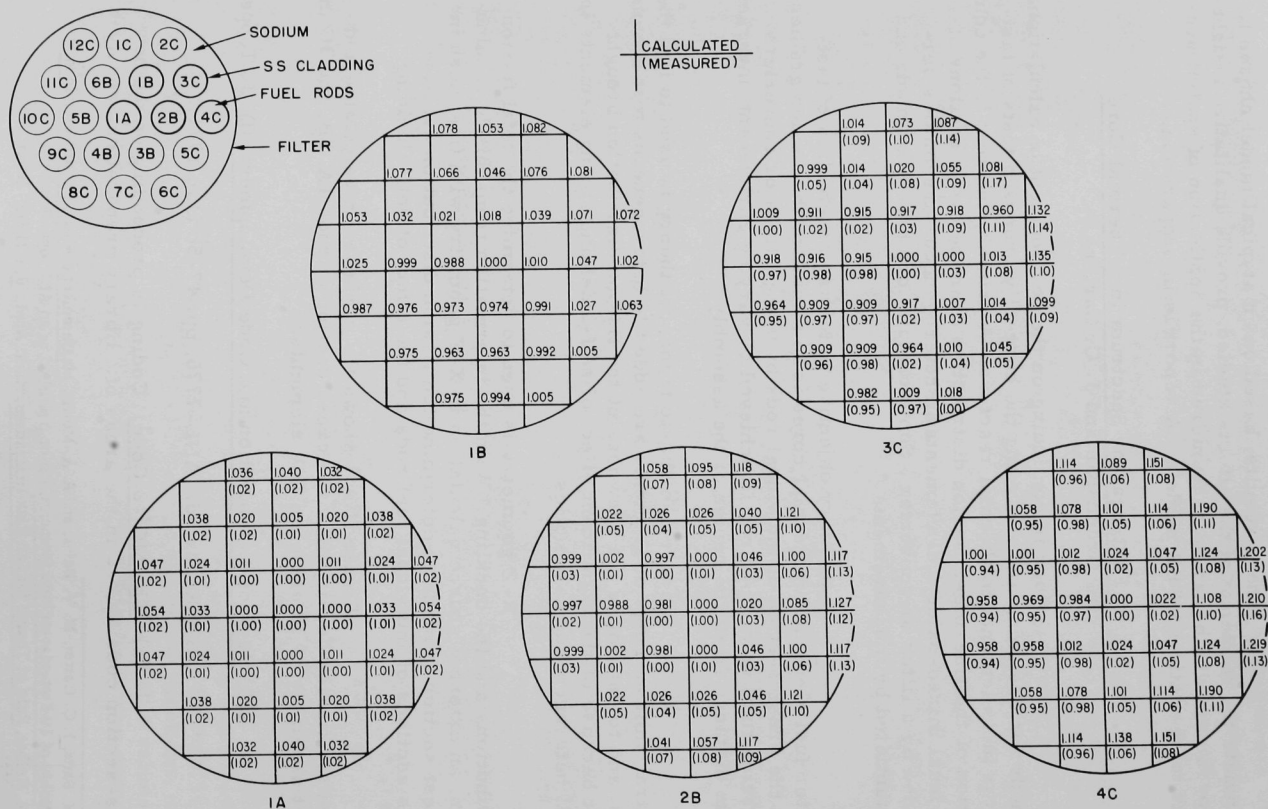


Fig. IIA.1. Calculated and Measured Fission Distribution. ANL Neg. No. 900-433.

resonance J integral calculations; and macroscopic cross sections, continuous slowing-down moderating parameters, and Legendre elastic matrix preparation.

The code to generate the Legendre elastic scattering data file in the library preparation is nearing completion. A problem encountered in integrating products of high-order Legendre polynomials is being investigated. Until the other sections of the library code are completed, a test library is being prepared which will comply with the new library format but which will not contain completely realistic data.

The coding in the resolved resonance area is complete, except for the initial array setup and input processing. The code handles an arbitrary number of overlapping neighboring resonances and includes interference scattering. Both single-level and Adler-Adler multilevel representations are accommodated.

The subroutine QUICKW has been revised and shortened. QUICKW calculates the real and imaginary parts of the complex error function $W(x, y)$. The original QUICKW had a number of modes of calculation, depending upon the magnitude of $x^2 + y^2$, including: (i) table interpolation, (ii) a rational approximation, (iii) a continued-fraction representation, and (iv) an asymptotic approximation. For 10,000 calls to QUICKW, the times to execute the areas (i)-(iv) above were, respectively, 1.7, 1.2, 1.6, and 0.8 sec. The new QUICKW has dispensed with the continued-fraction representation. The table interpolation is used for $0 \leq x \leq 3.9$ and $0 \leq y \leq 3.0$. A different longer rational approximation is used for $3.9 < x \leq 6.0$ or $3.0 < y \leq 6.0$. The original rational approximation is used for $6.0 < x \leq 100.0$ or $6.0 < y \leq 100.0$. Finally, the asymptotic form is used for x or y greater than 100.0. The longer rational approximation requires 1.4 sec for 10,000 executions.

Coding to generate macroscopic cross sections, fission-spectrum distributions, extended transport cross sections, and P_0 and P_1 elastic scattering matrices is nearing completion. The macroscopic-cross-section calculation includes the smooth microscopic library data as well as the capture and fission cross sections calculated in the unresolved resonance area of the code. Several options are available to specify fission-spectrum distributions. Chi vectors are calculated once and stored on a peripheral device for use in the spectrum calculation. Chi matrices are recalculated in the spectrum area from library data, and a normalization factor is generated in this area of the code. A complete restart capability has been incorporated into the Legendre elastic scattering calculation. If microscopic matrices are not available for a material from a previous calculation, they will be generated using either the heavy mass approximation*

*H. Henryson II, Multigroup Elastic Scattering Cross Sections for Heavy Elements, Nucl. Sci. Eng. 43, 235 (1971).

or a hyperfine-group algorithm (see Progress Report for October 1970, pp. 106-110). Two transport approximations* are being provided on user option with the inconsistent P_1 or B_1 spectrum calculations to speed up the calculation of the P_0 scattering matrices.

2. Nuclear Data

a. Reactor Code Center (M. Butler) (189a 02-085)

Last Reported: ANL-7776, pp. 61-62 (Jan 1971).

In February, seven program packages were incorporated in the Code Center program library. Six of these were new programs; the other was a revised CDC 6600 version of the PDQ-7 program. Babcock and Wilcox converted the Bettis Atomic Power Laboratory's Environmental Routines and PDQ-7 to the SCOPE 3.1.6 Operating System, and this version of the library program, ACC No. 275, is now ready for distribution.

The six new program packages include:

(1) ACC No. 455, DAC1, a one-dimensional S_n perturbation code prepared by Los Alamos Scientific Laboratory.** DAC1 uses DTF input and output fluxes to calculate reactivity perturbations, effective delayed-neutron fractions, or neutron generation time. It is written in FORTRAN IV for the CDC 6600.

(2) ACC No. 456, DBUFIT-1, a code designed to obtain integral-reaction cross-section values by fitting burnup equations to isotopic data.† This FORTRAN V program was developed by the Battelle Pacific Northwest Laboratory for plutonium and uranium-plutonium fuel computations on the UNIVAC 1108.

(3) ACC No. 461, EPOCH, a program prepared to calculate fine-detail $P-1$ flux spectra for simply buckled media using up to 2000 lethargy groups.†† Nuclear cross sections are obtained from the ENDF/B library, and neutron-flux ages are computed from multiple spectra calculations by varying the buckling. EPOCH was written in FORTRAN IV language for the CDC 6600 by Bettis Atomic Power Laboratory.

*W. M. Stacey, Jr., Approximate Treatments of the Effect of Anisotropy Upon Elastic Neutron Moderation, internal memorandum (Dec 1970).

**B. M. Carmichael, DAC1, A One Dimensional S_n Perturbation Code, LA-4342 (Apr 1, 1970).

†R. P. Matsen, DBUFIT-1, A Least Squares Analysis Code for Nuclear Burnup Data, BNWL-1396 (May 1970).

††J. D. Butler, E. M. Gelbard, and E. Schmidt, EPOCH, A Program to Calculate Neutron Ages Using the ENDF/B Library, WAPD-TM-822 Addendum 1 (May 1970).

(4) ACC No. 464, DYNO-1, a FORTRAN program for determining the distribution of electrons emitted from a photomultiplier composed of a series of dynodes.* This package was contributed by Knolls Atomic Power Laboratory.

(5) ACC No. 466, APRFX-1, a cross-section collapsing code for use with multigroup constant data in the ANISN-DOT format. This FORTRAN IV program was prepared for use in Army Pulse Radiation Facility Reactor calculations by the U.S. Army Aberdeen Research and Development Center.

(6) ACC No. 473, CHIN-KIN, a FORTRAN program developed at Bettis Atomic Power Laboratory** to treat fast- and intermediate-reactivity transients in a water-cooled heterogeneous reactor. This package is written for the CDC 6600 computer.

B. Reactor Fuels and Materials Development

1. Core Applications Planning and Analysis

- a. Empirical Assessment of Swelling and Creep Correlations
(P. R. Huebotter and T. R. Bump) (Program Coordination)

Not previously reported.

Contemporary LMFBR core design requires reliable expressions for fast-neutron-induced swelling and radiation-enhanced creep of stainless steel, as well as an understanding of integral swelling-creep effects on core structural components. Existing correlations involve considerable uncertainty and are based on controlled experiments to a fluence that is a small fraction of FTR and LMFBR Demonstration Plant targets.

Core components removed from EBR-II, at fluences now approaching these targets, exhibit deformations that are attributable to a combination of swelling and creep. These deformations are being analyzed to ascertain the reliability of existing swelling and creep correlations and to gain further insight into the response of stainless steel, in typical core structural applications, to the LMFBR environment. The EBR-II Project provides the neutron fluxes and temperatures employed in the analyses.

*J. E. Edwards and J. F. McCarthy, DYNO-1, A Program to Compute the Distribution of Secondary Electrons in Photomultipliers, KAPL-M-6575 (Sept 21, 1966).

**J. A. Redfield, CHIN-KIN, a FORTRAN Program for Intermediate and Fast Transients in a Water Moderated Reactor, WAPD-TM-479 (Jan 1965).

(i) Wrapper Tube on Experimental Assembly XA08
(T. R. Bump)

Photographs* of the XA08 assembly after about 8×10^{22} nvt peak exposure indicated that its wrapper tube had a permanent bow oriented properly to be consistent with differential swelling effects. To obtain a

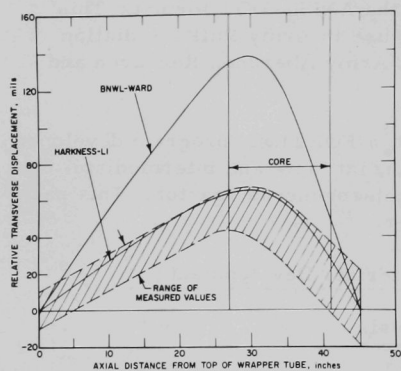


Fig. II.B.1. Relative Transverse Displacement vs Axial Distance from Top of Wrapper Tube for EBR-II Assembly XA08.
Neg. No. MSD-53907.

quantitative description of the bow (shaded area in Fig. II.B.1), positive transparencies of two photographs of opposite sides of the assembly were appraised with an EPO LP-2 Profile Projector. Displacements were measured at each side of the assembly in each transparency, producing four displacement measurements at each elevation. Corrections were necessary because the planes of an included ruler (and reference straight edges), assembly, and photographic plate evidently were not parallel. This skewed condition affected the local focus of the transparencies, and both factors contributed to the wide scatter band of the measured displacements. Future comparisons of this type will be easier, as many assem-

blies with interesting deformations (and with peak exposures up to 1.7×10^{23} nvt) now are being measured directly before disposal.

The calculated displacements in Fig. II.B.1 were obtained by using two swelling correlations for noncold-worked stainless steel** and the GROW code.[†] The code does not account for assembly interactions; such interactions evidently occur, because the displacements in Fig. II.B.1 produce unrestrained assembly upper-end deflections in the range of 0.3-0.6 in., and the initial upper-end clearance between XA08 and the relevant adjacent (never-swollen) assembly was only about 0.02 in., according to calculations that considered thermal deflections.^{††} Because interactions could alter the final assembly shape through radiation-enhanced creep, it

*C. L. Meyers, Argonne National Laboratory (EBR-II Project), private communication (Nov 1969).

**R. J. Jackson, Battelle Northwest Laboratory, private communication (Apr 1970); S. D. Harkness and

C. Y. Li, A Study of Void Formation in Fast Neutron Irradiated Metals (to be published in Trans. AIME).

[†]T. R. Bump and W. Marr, An LMFBF Design to Accommodate Steel Swelling, Trans. Am. Nucl. Soc. **13**, 129 (1970).

^{††}T. R. Bump, BOW-II: A Code for Calculating Deflections of Closely Spaced Parallel Beams, ANL-7528 (to be published).

is risky to draw conclusions from Fig. II.B.1 at this time. To permit consideration of the interactions, the BOW-V* and CRASIB** codes are being combined.

The distances across the stamped spacer pads of the XA08 assembly wrapper tube remained essentially unchanged because of external forces, even though nearby the tube was swelling about 20 mils across flats;[†] that is, a "moat" was formed adjacent to the pads. To find if this moat formation is comprehensible, AXICRP^{††} calculations were made using a centrally loaded, circular, flat-plate representation and a noncold-worked creep correlation.[‡] The pad load was assumed to be uniformly distributed and equal to a constant 25 lb, as suggested by BOW-II calculations. The constant-load assumption seems reasonable because of the constant distance maintained across pads and the "nesting" characteristics of wrapper tubes. The periphery of the plate was assumed to be simply supported. Reasonable values of total creep deformation were obtained, but no sign of moat formation was observable. Further calculations are being performed in this area to study the effects of different boundary conditions on results and to minimize computer time requirements.

(ii) Fuel-element Claddings in Experimental Assembly X040A
(T. R. Bump)

The unencapsulated mixed-oxide fuel elements in the X040A assembly were observed, after about 4×10^{22} nvt peak exposure, to have acquired significant permanent bows, generally in the form of "belly-out" from the assembly centerline. At least the peripheral elements were highly overcooled on their outboard sides,^{‡‡} and thus were subjected to thermal stresses oriented properly to explain the bowing, provided creep overshadowed the differential swelling. Calculated bows have been obtained for four peripheral elements by using noncold-worked swelling and creep correlations[‡] and CRASIB. The 61-in.-long elements were assumed to be restrained laterally at 29 axial positions during operation, which may be more restraint than the elements actually experienced.

Measured and calculated bows are compared in Table II.B.1. The calculated values have the same sign as, but are substantially larger

*D. A. Kucera and D. Mohr, BOW-V: A CDC-3600 Program to Calculate the Equilibrium Configurations of a Thermally Bowed Reactor Core, ANL/EBR-014 (Jan 1970).

**W. H. Sutherland and V. B. Watwood, Jr., Creep Analysis of Statically Indeterminate Beams, BNWL-1362 (June 1970); R. D. Cheverton, Oak Ridge National Laboratory, private communication (July 1970).

†L. J. Koch, Mechanical Requirements of the LMFBR, Nuclear News 13(11), 61-65 (Nov 1970); S. D. Harkness, B. J. Kestel, and D. G. Franklin, "Swelling in the Dimple Region of Subassembly XA08," Reactor Development Program Progress Report, ANL-7758, pp. 5-6 (Nov 1970).

††W. H. Sutherland, A Finite Element Computer Code (AXICRP) for Creep Analysis, BNWL-1142 (Oct 1969).

‡R. J. Jackson, Battelle Northwest Laboratory, private communication (Apr 1970).

‡‡F. D. McGinnis, Argonne National Laboratory (EBR-II Project), private communication (Aug 1970).

than, the measured values, indicating that either (a) the creep correlation gives creep rates that are too high, or (b) the swelling correlation gives thermal-differential-swelling values that are too low. In view of the evidence (see Fig. II.B.1) that the swelling correlation gives absolute swelling values, at least, that are sufficiently high, it appears that the creep correlation is suspect. Further calculations will study the effects of different restraint assumptions and swelling and creep correlations on calculated deformations.

TABLE II.B.1. Magnitude of "Belly-out" Bow of X040A Fuel Elements

Element Identification	AISI-type Cladding Material	Belly-out Bow, in.	
		Measured ^a	Calculated ^b
021 (ANL)	304L	0.23	0.92
025 (ANL)	304L	0.30	0.92
B-5 (GE)	316	0.18	0.98
B-16 (GE)	316	0.10	0.98

^aR. V. Strain, Argonne National Laboratory (EBR-II Project), private communication (July 1970).

^bElements were assumed to be highly restrained in pile; noncold-worked swelling and creep correlations were used.

The B-5 and B-16 elements were on the side of the assembly away from the core vertical centerline, and the 021 and 025 elements were on the side toward the core centerline. However, the flux gradients of Elements 021 and 025 were of opposite sign to that of their temperature gradients, which did not affect the calculated results noticeably, but may have had something to do with the measured bow of the Type 316 stainless steel-clad elements being less than that of the Type 304L stainless steel-clad elements.

The calculations indicated that at the point of maximum creep strain (the core exit) the initial cladding peak thermal stresses for all elements were about 18,000 psi at the start of operation. At 25% of total peak flux exposure time, the total stresses had decreased to 7000 psi due to 0.05% creep strain, and at the end of exposure the total stresses and creep strain were about 2500 psi and 0.09%, respectively.

2. Fuels and Claddings

a. Behavior of Reactor Materials (189a 02-086)

(i) Oxide-fuel Swelling Mechanisms and Models (R. B. Poeppel)

Last Reported: ANL-7737, pp. 109-110 (Aug 1970).

The ANL-developed Gas Release and Swelling Subroutine (GRASS) has been extensively revised and is now ready for production runs and inclusion into the LIFE code. Convergence time has been greatly improved through the use of the hyperbolic tangent function in the integration subroutine.

The hyperbolic tangent is found as an approximation to the solution of the differential equation that describes the evolution of the bubble-size distribution. The equations are written in the form

$$\frac{df_i}{dt_i} = -a_i f_i^2 - b_i f_i + c_i, \quad (1)$$

where

f_i = number of bubbles in the i th size range,

a_i = rate at which bubbles are lost from the i th range through coalescence with bubbles of the same size,

b_i = rate at which bubbles are lost from the i th range through coalescence with bubbles of different sizes and by resolution and migration,

c_i = rate at which bubbles are formed in the i th range,

and

$$f_i, a_i, b_i, c_i \geq 0.$$

The parameters b_i and c_i are functions of f_j , $j \neq i$; i.e.,

$$b_i = b_i(f_1, \dots, f_{i-1}, f_{i+1}, \dots, f_{i_{\max}}),$$

and

$$c_i = c_i(f_1, \dots, f_{i-1}, f_{i+1}, \dots, f_{i_{\max}}).$$

Equation 1 can then be integrated for each i with the assumption that b_i and c_i are constant over the time interval of integration. The result is*

$$t_i = -\frac{1}{a_i(p_i - q_i)} \log \frac{f_i - p_i}{f_i - q_i}, \quad (2)$$

where p_i and q_i are, respectively, the positive and negative roots of

$$-a_i f_i^2 - b_i f_i + c_i = 0. \quad (3)$$

Equation 2 is used to find t_i^0 , which is the value of t_i corresponding to the value of f_i , f_i^0 , at the beginning of the time step. Equation 2 is then inverted** to find $f_i(t)$:

$$\left. \begin{aligned} f_i(t) &= \frac{1}{2a_i} \left\{ \left(b_i^2 + 4a_i c_i \right) \tanh \left[\frac{1}{2} \left(b_i^2 + 4a_i c_i \right)^{1/2} \left(t - t^0 + t_i^0 \right) \right] + b_i \right\}, & f_i < p_i, \\ f_i(t) &= \frac{1}{2a_i} \left\{ \left(b_i^2 + 4a_i c_i \right) \operatorname{ctnh} \left[\frac{1}{2} \left(b_i^2 + 4a_i c_i \right)^{1/2} \left(t - t^0 + t_i^0 \right) \right] + b_i \right\}, & f_i > p_i, \\ f_i(t) &= p_i, & f_i = p_i, \end{aligned} \right\} \quad (4)$$

where t is the true time, and t^0 is the true time at the beginning of the time step.

Equation 4 has been used successfully to decrease convergence time by more than an order of magnitude. GRASS is now a useful tool for parametric studies.

b. Oxide Fuel Studies (189a 02-005)

- (i) Fuel-swelling Studies (L. C. Michels, G. M. Dragel, and J. C. Tezak)

Last Reported: ANL-7742, pp. 100-102 (Sept 1970).

The shielded glove facility for the preparation of irradiated oxide fuel specimens for transmission-electron microscopy is essentially complete. The equipment for preparation of the specimens has been installed in the gloveboxes, and the gloveboxes are being checked for leaks. This facility will be used initially to study mixed-oxide fuels irradiated in EBR-II.

*Herbert Bristol Dwight, Tables of Integrate and Other Mathematical Data, Rev. Ed., Macmillan, 1947, p. 33.

**Loc. cit., p. 29.

The entire facility for the preparation of specimens and their transfer to the 200-kV Hitachi electron microscope consists of (1) an alpha-tight glovebox, shielded with 4 in. of steel and equipped with PAR Model MM-2436 manipulators, where the principal preparation steps are performed, (2) an unshielded alpha glovebox for coating and mounting the prepared specimens, and (3) an unshielded glovebox attached to the microscope for introduction of specimens.

The procedure of preparing a thin specimen for microscopy begins with a mounted transverse section from an EBR-II-irradiated oxide fuel element. The polished metallographic specimen is transferred from the Alpha-Gamma Hot Cell to the shielded glovebox in a small cask designed for the purpose. In the glovebox, the specimen is ultrasonically core-drilled in three radial locations, each corresponding to a different fuel structural region, to a depth of ~ 0.025 in. A cylindrical stainless steel tool, with an outside diameter of 0.120 in. and an inside diameter of 0.050 in., is used for drilling. This operation leaves three annular-shape regions each containing a 0.050-in.-dia cylinder of fuel in the center. The metallographic specimen is transferred to the Alpha-Gamma Hot Cell where it is impregnated with cold-setting epoxy resin to fill the annular rings. The specimen is ground down to the original surface to remove excess epoxy. The metallographic specimen is then joined face-to-face with a blank mount of the same diameter using double-backed adhesive tape. A transverse cut is made through the original mount leaving a 0.025-in.-thick slice containing the three annular regions attached to the blank mount. This mounted slice is then ground until its thickness is reduced to 0.010-0.015 in., and then it is transferred to the shielded glovebox.

To further thin the fuel samples, a 0.038-in.-dia hole is ultrasonically drilled to within 0.003 in. of the bottom of each of the three 0.050-in.-dia fuel cylinders.* The three annular rings of epoxy containing the fuel specimens, now in the form of a "cup," are separated from the surrounding material by an ultrasonic core-drilling operation leaving the three islands of epoxy attached, by the adhesive tape, to the blank mount. The adhesive is then dissolved using acetone.

The final thinning is accomplished by dipping the specimens into an agitated hot chemical polishing solution.** The thinned fuel specimens are transferred to the unshielded glovebox, where a thin coating of gold is deposited on one surface, and the specimens are mounted in specimen holders for the electron microscope.

The specimen holder containing the thinned specimen is transferred to the unshielded glovebox connected to the electron microscope, where it is introduced into the microscope column for examination.

*D. J. Keast, J. Sci. Instrum. 44, 862 (1967).

**A. J. Manley, J. Nucl. Mater. 15, 143 (1965).

3. Radiation Damage on Structural Materials

a. In-reactor Creep Studies (189a 02-091)

- (i) A Simulation of In-reactor Test Conditions Using Cyclotron Bombardment (S. D. Harkness, F. L. Yaggee, and J. W. Styles)

Last Reported: ANL-7765, p. 65 (Dec 1970).

Uniaxial creep tests were performed on a specimen of 20% cold-worked Type 316 stainless steel during 22-MeV-deuteron bombardment at a nominal temperature of 505°C. The specimen (gauge section 1.0 by 0.208 by 0.010 in.) was one of six obtained from a 0.60-in.-dia by 8.0-in.-long rod (B-51) provided by WADCO (HT 87210). The purpose of the test was to obtain information on the minimum creep rate for this material at 482°C and a stress of 20,000 psi under deuteron bombardment, and the results will be compared with the WADCO creep tests in EBR-II on the same material. The results of the uniaxial creep tests conducted in this cyclotron run are given in Table II.B.2. Because the specimen was tested for creep at 492°C and a stress of 18,930 psi for 200 hr in the absence of deuteron bombardment, the metallurgical structure at the end of this period will remain constant and thus sustain a minimum creep rate. Therefore, the values of the minimum creep rate given in Table II.B.2 do not contain a contribution from primary creep.

TABLE II.B.2. Results of Simulation of In-pile Creep of 20% Cold-worked Type 316 Stainless Steel Using 22-MeV-deuteron Bombardment

Deuteron Current, μA	Stress, psi	Temperature, °C	Duration of Test, hr	Minimum Strain Rate, hr^{-1}	Correlation Parameter	Stress Dependence, a_n
0	18,930	492 \pm 2	200	$< 1 \times 10^{-7}$	-	-
2.61 \pm 0.08	18,930	501 \pm 2	12.8	1.1×10^{-5}	0.60	-
2.54 \pm 0.09	34,780	506 \pm 2	7.5	2.7×10^{-5}	0.82	1.5
2.85 \pm 0.08	48,745	508 \pm 2	14	6.1×10^{-5}	0.88	2.1
0	48,745	470 \pm 2	72	2.3×10^{-6}	0.96	-

$$a_n = K \sigma^n$$

The stress dependencies for irradiation-controlled creep obtained from the data in Table II.B.2 were 1.5 and 2.1. The stress dependence for this material under thermal-creep conditions at 500°C is between 6 and 8 for the same stress range.

4. Techniques of Fabrication and Testing

a. Nondestructive Testing Research and Development (189a 02-092)

(i) Neutron Radiography

(a) Thermal Neutron Radiography with ^{252}Cf (J. P. Barton)

Last Reported: ANL-7753, pp. 124-125 (Oct 1970).

Previous experiments with ^{252}Cf neutron radiography have indicated the importance of an air gap between the collimator liner and the source. A small air gap between source and neutron opaque wall material forming the collimator input can increase radiographic resolution by a factor of two in collimator ratio. More detailed experiments have shown the significant effects of fine changes in the actual dimension of this air gap on the separate factors of (a) exposure rate, (b) radiographic contrast for cadmium, (c) indium, (d) hydrogenous material, (e) inherent resolution, (f) detail visibility involving geometric resolution for low-neutron opacity material, and (g) detail visibility involving geometric resolution for high-neutron opacity material. The results reported are for a divergent collimator that has an inlet diameter of 5 cm and a length of 56 cm; the 12-cm length nearest the source is constructed of pure paraffin, and the remainder (44 cm) is boron-loaded paraffin. A collimator lining of cadmium foil extending from the outer end to the source end aperture creates a zero air gap. A lining extending only to within 12.5 cm of the source end aperture coincides with the boron shielded part and yields a 12.5-cm air gap. Intermediate air gaps have been studied at intervals of 2.5 cm. The effect of introducing an air gap on the exposure rate is at first very abrupt (90% increase in exposure rate for the first 2.5-cm gap), and then the effect is less rapid, leveling off at about 10-cm air gap, with an increase in exposure rate of a factor of four compared with zero air gaps. Likewise, the effect of introducing an air gap on the radiographic contrast is at first large (for cadmium, the contrast increase is 60% for the first 2.5-cm gap) and thereafter saturates rapidly (only an additional 10% increase over the full range studied). The effect on an inherent resolution test (fine detail visibility in cadmium foil placed near the imaging plane) is that the first 2.5-cm air gap makes significant improvement, but beyond that the inherent resolution deteriorates again. This peaking effect is probably not only due to the interdependence of the inherent resolution test with contrast and geometric resolution, but also to the increasing importance of statistical effects as the neutron spectrum becomes more completely thermal and fewer signals are recorded. The air-gap effect on detail visibility also shows significant peaking for both low-contrast (plastic) and high-contrast (cadmium) details. The rise to

the peak from a zero air gap to a 2.5-cm air gap is relatively rapid; thereafter the decline is relatively slow. The results enable us to draw the following general conclusions: For the best overall contrast of large detail areas and for best exposure rates for a given-size ^{252}Cf source, air-gap dimensions of 10-12.5 cm should be used. For the best visibility of very small detail, the air-gap dimensions should be 2.5 cm. For the best compromise between exposure rate, contrast, and detail visibility, an air-gap dimension of 5 cm should be used.

- (b) Track-etch Detection Methods (H. Berger and N. P. Lapinski)

Last Reported: ANL-7669, pp. 119-120 (Feb 1970).

Contrast studies on track-etch detection methods have been conducted with several plastic detection materials and a test object consisting of a natural-uranium, stepped penetrometer and a 2.54-cm-thick base material. Techniques studied in these thermal-neutron radiographic tests included several cellulose nitrate materials exposed with alpha-emitting screens of natural lithium borate and $^6\text{Li-F}$, and with fission-fragment-emitting screens of ^{235}U foil. The latter screens were also used with several polycarbonate plastics. Included in the study were several tests at total neutron exposures from 10^5 to 10^9 n/cm² of 10- μm -thick Kimfoil polycarbonate plastic. It is planned that these plastics will be etched and image-enhanced by sparking techniques.*

For the visual images examined thus far, without attempts at image enhancement, the best contrast has been observed for the cellulose nitrate plastic, Eastman Kodak Type 106-01. Thickness changes of 6% have been readily observed; changes as small as 2% may be brought out by image-enhancement techniques (photographic or spark methods). This compares with previously achieved results in which contrasts of only 10% could be observed.**

- b. NDT Measurement of Effective Cold Work in Cladding Tubes
(C. J. Renken) (189a 02-133)

Last Reported: ANL-7705, pp. 149-150 (June 1970).

Significant progress has been achieved with a method involving measurement of magnetic retentivity for determining cold work in Type 316 stainless steel.

*B. G. Oltman, F. Congel, N. P. Lapinski, and H. Berger, Trans. Am. Nucl. Soc. 13, 531-532 (1970).

**H. Berger and I. R. Kraska, Trans. Am. Nucl. Soc. 10, 72-73 (1967).

In small-diameter, thin-wall tubing containing $< 50\%$ cold work, it is not practical to attempt to measure the retentivity in any environment, except one that has exceptionally stable and uniform magnetic fields. For example, the change in field caused by the rotation of a steel desk chair at 15 m from the point of measurement may well be an order of magnitude above the field due to the martensite in a 20% cold-worked tube.

Recently, however, by a method of mechanical modulation of the magnetic field produced by the specimen and filtering of the output of the magnetometer, useful signals have been produced from tubes containing amounts of cold work as low as 5%. The steps involved in the process include (1) demagnetization of the tube, (2) formation of a magnetic field along a diameter of the tube, (3) rotation of the line-magnetized tube at a constant rate past the magnetometer probe, and (4) processing of the signal after filtering to peak the system at the tube-rotation frequency used.

In initial tests, a logarithmic system response has been obtained as a function of cold work. Differences have been observed between tubing made by various manufacturers, a fact that possibly reflects varying amounts of redundant cold work introduced by the manufacturing process. For one tubing type, the response followed a smooth curve. These tests have been made with a rotation rate of 10 rps, giving a modulation frequency of 10 Hz. This would limit the throughput of a single system to about 4 m/min; however, the throughput could be increased several times by working at higher rotation rates.

Effects of changes in chemistry of the stainless steel material will be investigated.

5. Engineering Properties of Reactor Materials

a. High-temperature Properties of Ceramic Fuels (189a 02-094)

(i) Plastic Yielding and Fracture of Mixed Oxides (J. T. A. Roberts and B. J. Wrona)

Last Reported: ANL-7765, pp. 67-68 (Dec 1970).

In four-point-bending tests of UO_2 -20 wt % PuO_2 specimens, the brittle-to-ductile transition temperature T_C coincides with the temperature at which maximum strength is measured. An alternative method of determining T_C is to use the temperature of intersection of the curve of yield stress σ_y (σ_y is assumed to be the elastic limit) versus temperature with the curve of fracture stress versus temperature. This is illustrated in Fig. II.B.2 using data obtained from specimens (~96% TD) tested at strain rates of 0.085-0.75 hr^{-1} . The values of T_C and the temperature of maximum

strength are presented in Table II.B.3 for two batches of UO_2 -20 wt % PuO_2 specimens with theoretical densities of $96.6 \pm 0.4\%$ ($\dot{\epsilon} = 0.085 \text{ hr}^{-1}$) and $96 \pm 0.5\%$ ($\dot{\epsilon} = 0.15 - 0.73 \text{ hr}^{-1}$); both had a grain size of $2.5 \pm 0.5 \mu\text{m}$ and an $\text{O/M} = 1.97 \pm 0.005$. The results of previous work* on UO_2 are included for comparison. The two temperatures are essentially equivalent in the mixed oxide, but are separated by $\sim 300^\circ\text{C}$ in UO_2 .

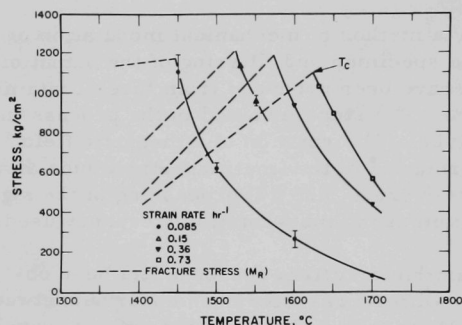


Fig. II.B.2

Effect of Temperature and Strain Rate on the Fracture Stress and Elastic Limit of UO_2 -20 wt % PuO_2 . Neg.No. MSD-53920.

TABLE II.B.3. Critical Temperatures in Deformation of UO_2 -20 wt % PuO_2 and UO_2^a

Strain Rate, hr^{-1}	Brittle-to-ductile Transition T_c , $^\circ\text{C}$	Temperature of Maximum Strength, $^\circ\text{C}$
0.085	1445	1460
0.15	1525	1545
0.36	1575	1560
0.73	1625	1640
UO_2 ($97 \pm 0.5\%$ TD, $8 \mu\text{m}$ grain size, $\text{O/M} = 2.00 \pm 0.01$)		
0.092	1100	1416
0.92	1375	1591
9.2	1450	1780

^aR. F. Canon, J. T. A. Roberts, and R. J. Beals, J. Am. Ceram. Soc. (to be published).

*R. F. Canon, J. T. A. Roberts, and R. J. Beals, J. Am. Ceram. Soc. (to be published).

The transition from completely brittle to completely ductile behavior occurs over a much narrower temperature range in UO_2 -20 wt % PuO_2 . This must in some way be related to the different microstructures developed in UO_2 and UO -20 wt % PuO_2 . The former was stoichiometric, single phase, and homogeneous, with a grain size $\geq 8 \mu$. The latter was hypostoichiometric ($\text{O}/\text{M} = 1.97 \pm 0.005$) and inhomogeneous (in some areas, plutonium concentration varied from 15 to 30 wt % over a distance of 60μ) and had a grain size of $\approx 2 \mu$. The influence of grain size alone can profoundly affect mechanical properties, for example, by changing the rate-controlling deformation mechanism.* Inhomogeneity and hypostoichiometry are largely unknown quantities.

In UO_2 , the high-temperature transition (i.e., the temperature of maximum strength) was denoted by T_t^{**} and increased as the strain rate increased (0.09 - 9.0 hr^{-1}) according to the relation

$$T_t(^{\circ}\text{C}) = \frac{4.8 \times 10^4}{26.2 - \ln \dot{\epsilon} (\text{hr}^{-1})} - 273. \quad (1)$$

In UO_2 -20 wt % PuO_2 , T_c and T_t are equivalent, but the transition temperature is similarly affected by strain rate. When data from a single batch of specimens (strain rates 0.15 - 0.73 hr^{-1}) are used, the corresponding relation is

$$T_c(^{\circ}\text{C}) = \frac{5.5 \times 10^4}{28.6 - \ln \dot{\epsilon} (\text{hr}^{-1})} - 273. \quad (2)$$

Both equations are a rewritten form of an Arrhenius-type expression obtained by plotting $\ln \dot{\epsilon}$ against the reciprocal of the absolute transition temperature. The "activation energy" term obtained from the gradient of the curve is not meaningful, because the transition does not occur at a constant stress.

(ii) Atmosphere-control System for Mechanical Properties Measurements of Mixed-oxide Fuels (N. A. Javed)

Not previously reported.

A mixed oxide ($\text{U}_{0.8}\text{Pu}_{0.2}\text{O}_{2+x}$) with a stoichiometric composition of 1.97 - 1.98 has tentatively been chosen to fuel the Liquid Metal Fast Breeder (LMFBR). To predict fuel performance (e.g., swelling and cracking), the creep and fracture behavior must be determined as a function of stoichiometry, since the stoichiometry will change continuously during

*M. D. Seltzer, A. H. Clauer, and B. A. Wilcox, J. Nucl. Mater. **34**, 351 (1970).

**R. F. Canon, J. T. A. Roberts, and R. J. Beals, J. Am. Ceram. Soc. (to be published).

burnup. One method to achieve the required oxygen-to-metal ratio (O/M) is to equilibrate and test the specimens in a gaseous atmosphere that has the appropriate oxygen partial pressure.

Thermodynamic data on the $(\text{U,Pu})\text{O}_{2+x}$ solid-solution system* have been used to construct the curves shown in Fig. II.B.3. This graph can be used to predict the chemical potential of oxygen necessary to maintain a particular stoichiometry between 700 and 2000°C. It must be noted, however, that these data were extrapolated to temperatures above 1100°C because no information is available for the higher temperatures.

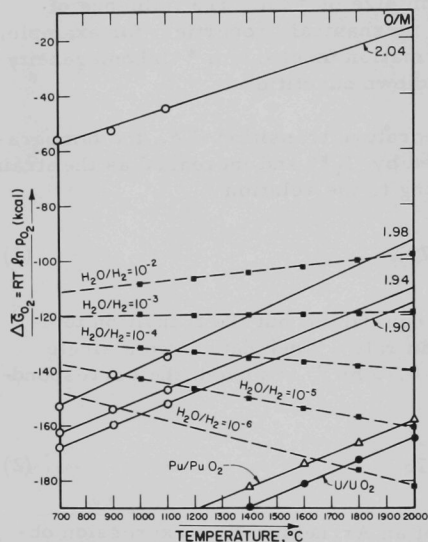


Fig. II.B.3. Chemical Potentials of Oxygen for $(\text{U}_{0.8}\text{Pu}_{0.2})\text{O}_{2-x}$ as a Function of Temperature and $\text{H}_2\text{O}/\text{H}_2$

Figure II.B.3 shows that, for O/M ratios of 1.94-1.98 and temperatures of 1100-1800°C, the required chemical potentials of oxygen are in the range of -155 to -110 kcal/mole. To achieve the desired low chemical potentials of oxygen, gaseous equilibria such as $\text{H}_2/\text{H}_2\text{O}$ or CO/CO_2 can be used, provided the required low ratios of $\text{H}_2\text{O}/\text{H}_2$ (10^{-5} to 10^{-2}) or appropriate ratios for CO/CO_2 are controlled and measured with reasonable accuracy.

A system using $\text{H}_2/\text{H}_2\text{O}$ mixture was chosen to control stoichiometry during the $\text{UO}_2\text{-PuO}_2$

deformation studies, since easier and better means are available to control and measure low moisture contents (i.e., down to 1-2 ppm in flowing hydrogen). The low moisture content and the associated very low dew point are achieved by passing purified, water-saturated hydrogen through a variable-temperature refrigeration unit. At each test-furnace inlet and outlet, moisture content is measured with a hygrometer. The controlled atmosphere equipment and test-furnace arrangements are shown in Fig. II.B.4.

The $\text{UO}_2\text{-20 wt \% PuO}_2$ specimens are now being equilibrated at 1700°C to produce O/M ratios of 1.90-2.00. X-ray analyses will determine whether the extrapolation technique used to generate Fig. II.B.3 is valid. This is a critical experiment in relation to the proposed creep and fracture work, where test temperatures up to 1700°C, and possibly higher, will be used.

*T. L. Markin and E. J. McIver, Plutonium 1965, p. 845.

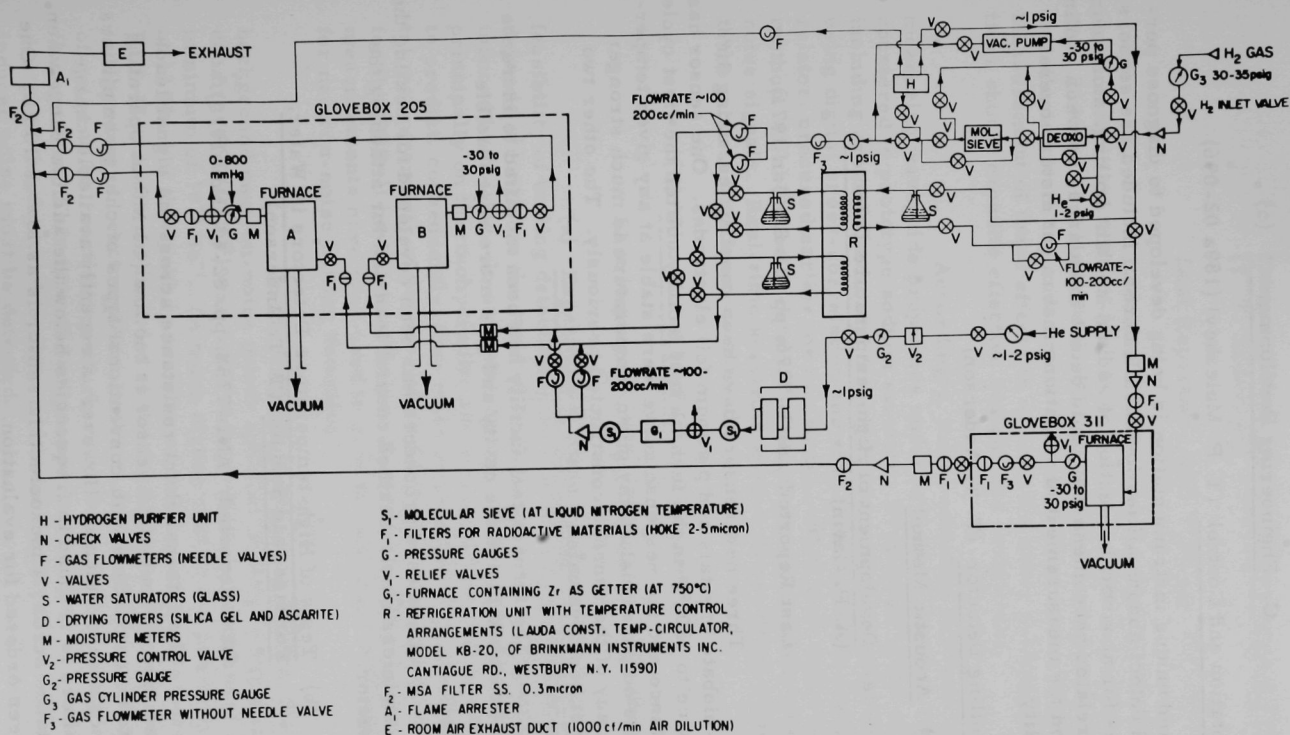


Fig. II.B.4. Furnace Arrangements for Study of the (Uranium-Plutonium) Dioxide Solid-solution System at High Temperatures. Neg. No. MSD 53777.

C. Engineering Development

1. Instrumentation and Control (T. P. Mulcahey) (189a 02-096)

New and unique instrumentation is being developed to diagnose performance and detect abnormalities in LMFBF cores. Included are sensors and techniques for acoustical detection of sodium-coolant boiling, monitoring of flow-rate-related phenomena that could detect imbalances between cooling and power, and the measurement of vibrations that might disturb overall reactor stability.

a. Boiling Detector (T. T. Anderson)

(i) Acoustic Method

(a) Development of High-temperature Detector (A. P. Gavin)

Last Reported: ANL-7776, pp. 81-82 (Jan 1971).

Three new sensors have been constructed, using 36° Y-cut lithium-niobate crystals and platinum foil electrodes. One sensor has been cycled twice to 1200°F in the furnace test facility. After the first cycle, both the resistance and the response curve were stable at any given temperature. Also, the output signal at any given temperature is much stronger than that from any of the sensors constructed previously. The other two sensors have not been evaluated.

The furnace test facility has been modified to increase the sound level produced inside the cavity and give more reproducible results.

A standard procedure has been developed for sealing the cold end of the stainless steel-sheathed coaxial lead and for attaching the electrical connector.

(b) Tests of High-temperature Detectors in Water, Furnace, and Sodium (T. T. Anderson)

Last Reported: ANL-7758, pp. 82-83 (Nov 1970).

The internal shunt resistance across the signal leads of a high-temperature piezoelectric sensor is too low ($< 1 \text{ M}\Omega$ at operating temperatures) to be compatible with conventional types of charge amplifiers for low-frequency measurements. However, a recently available charge amplifier is claimed to respond to frequencies below the audible range when the shunt resistance across a piezoelectric sensor is as low as $10 \text{ k}\Omega$. One amplifier has been ordered for evaluation.

(c) Design of Prototype Boiling-detection System
(T. T. Anderson)

Last Reported: ANL-7737, pp. 132-133 (Aug 1970).

Previous studies of waveguides for monitoring acoustic phenomena in the EBR-II (see Progress Report for September 1968, ANL-7500, p. 104) have shown that the acoustic energy in a solid waveguide is reflected from the ends and is dissipated after multiple reflections. Measurement of these effects in waveguides under prototype-reactor conditions should expedite effective designs and evaluations.

Accordingly, instrumentation has been assembled for measuring waveguide properties under acoustic conditions likely to be encountered in prototype sodium systems. Properties of the acoustic noise including acoustic paths and frequency transmission bands will be explored, using digital cross-correlation and real-time spectrum analysis. The correlator, procured earlier for measuring sodium flow by the two-thermocouple method, will be used to determine transit times and reflections in acoustic noise signals. Real-time spectrum analyzers are being evaluated; thus far, three models have been examined.

(ii) Flux-noise Method (L. J. Habegger)

Last Reported: ANL-7705, pp. 153-154 (June 1970).

(a) Experimental Measurement of Background Noise. The feasibility of boiling detection in an LMFBF by analysis of neutron noise depends strongly on the level of background noise superimposed on the noise induced by boiling. In a power reactor, the background-noise level depends principally on thermohydraulic and structural fluctuations which are difficult to predict; consequently, they must be obtained experimentally. Experimental measurements of background-noise power spectral density (PSD(f)) levels for the EBR-II have been obtained at various reactor powers, and these measurements have been used to give an indication of feasibility requirements for neutron-noise boiling detection.

In the frequency range 4 to 100 Hz, the ratio of the background neutron-noise power spectral density to squared mean neutron density $(\text{PSD}(f)/|\bar{n}|^2)$ was found to vary from a maximum of $2 \times 10^{-6} \text{ Hz}^{-1}$ to a minimum of 10^{-8} Hz^{-1} . (A much higher peak in the power spectrum occurred at 12 Hz, but this peak is considered to be a unique characteristic of the EBR-II and was not included in the feasibility analysis.) This ratio remained independent of reactor power in the 4- to 100-Hz range, indicating the source of noise to be reactivity perturbations from thermohydraulic or structural fluctuations. This type of background noise cannot be readily reduced by redesign of the detection system and is thus a fixed level above which boiling-induced noise must be detected.

In the frequency range 100 to 1000 Hz, the ratio $\text{PSD}(f)/|\bar{n}|^2$ was inversely proportional to the mean density \bar{n} and independent of frequency f . This type of dependency is characteristic of noise resulting from either the statistics of the detection process or inherent neutron density fluctuations; the relative level of this noise can be reduced by increasing detector efficiency or increasing reactor power.* Thus in this frequency range, the $\text{PSD}(f)/|\bar{n}|^2$ value of 10^{-8} Hz^{-1} , obtained at the highest power level of 50 MWt, is a maximum for the background noise.

By using estimates of the background noise spectrum, the experimental requirements for detecting boiling-induced neutron noise at a given frequency, with, for example, 90% confidence, can be approximated by the relations**

$$\frac{\text{Spread}}{2} \leq \left[1 + \frac{\text{PSD}(f)/|\bar{n}|^2, \text{boiling}}{\text{PSD}(f)/|\bar{n}|^2, \text{background}} \right] \quad (1)$$

and

$$\text{Spread} = \frac{14}{[2(\text{duration of sample})(\text{resolution, Hz}) - 5/3]^{1/2}}, \quad (2)$$

where Spread is the value, in decibels, of the ratio of the upper and lower boundaries of the range in which 90% of the estimates of total power spectral density will fall on the average.

An indication of the results obtained with Eqs. 1 and 2 is obtained by assuming a (duration of sample)(resolution, Hz) product of 50 (e.g., a 10-sec sample with 5-Hz resolution, or a 0.5-sec sample with 100-Hz resolution). In this example, a boiling-to-background ratio of at least 0.085 is required to detect, with 90% confidence, at each frequency the increased noise level due to the onset of boiling. With a conservative estimate of $2 \times 10^{-6} \text{ Hz}^{-1}$ for the background noise, a boiling noise of $1.7 \times 10^{-7} \text{ Hz}^{-1}$ would be required for detection. For a less conservative background noise level of 10^{-8} Hz^{-1} , the detectable boiling noise level is $8.5 \times 10^{-10} \text{ Hz}^{-1}$.

In the frequency range 4 to 1000 Hz, the ratio of reactivity $\text{PSD}(f)$ to neutron $\text{PSD}(f)/|\bar{n}|^2$ is approximately 10^{-4} for the EBR-II. Thus for a neutron noise-level range of 1.7×10^{-7} to $8.5 \times 10^{-10} \text{ Hz}^{-1}$, the boiling void $\text{PSD}(f)$ is in the range 17 to $0.085 \text{ cm}^6\text{-Hz}^{-1}$ for an assumed sodium void reactivity coefficient of $10^{-6}/\text{cm}^3$.

The amount of boiling which would give the above power spectral densities for the void fluctuations is unknown at present. However,

*C. E. Cohn, A Simplified Theory of Pile Noise, Nucl. Sci. Engr. 7, 472-475 (1960).

**R. B. Blackman and J. W. Tukey, The Measurement of Power Spectra, Dover Publications, Inc., New York (1958).

as an example, if it is assumed that $PSD(f)$ for the void fluctuations is constant between 0 and f_0 Hz, and that the boiling void volume V has a Poisson distribution ($\sigma_V^2 = V$), the above values give average void volumes of from 0.085 to 17 f_0 cm³. (For f_0 equal to 100 Hz, as an example, these values represent a range of from 0.03 to 5.3% of the total sodium volume in the EBR-II core.)

The results from this analysis, which at best are qualitatively correct, emphasize the importance of various quantities in the boiling sodium process. At present these quantities are undetermined.

(b) Survey of Neutron-detection Techniques for Neutronic Noise Boiling Detection. A survey of existing techniques for fast-reactor neutron detection has been undertaken for the purpose of planning reactor experiments to test the feasibility of boiling detection by analysis of reactor neutron noise. This survey consisted of determining: (1) the restrictions for neutron detectors imposed by detector environments in the experimental facility, in this case, the EBR-II; and (2) the availability of detectors that satisfy these restrictions and, also, the specifications that are important for neutronic noise analysis.

Potential sites for detector location exist both in-core and out-of-core in the EBR-II. The out-of-core locations (Nuclear Instrument Test Facilities, NITF) available to experimenters are the O-1 and J-2 thimbles which penetrate the neutron shield. The physical dimensions (4.8-in. ID x 240 in. long) and temperature (125°F, with air cooling) of the O-1 location permits the use of standard reactor neutron detectors. The GE NA09 compensated ion chamber is available at the EBR-II site and is expected to be sufficient for immediate noise analysis applications in this location. The volume of the J-2 location is also adequate (6.2-in. ID x 84 in. long); however, temperatures in this thimble have been limited to the range 700 to 1200°F. Performance of out-of-core detectors in this temperature range has yet to be demonstrated, although several vendors offer detectors with maximum ratings in this range. An additional restriction of the NITF locations, from the standpoint of boiling detection, is the low value for the neutron flux, which is less than 0.01% of the flux in the core center.

Potential in-core locations for neutron detectors are provided by the Instrumented Subassembly (ISA) and the In-core Instrument Test Facility (INCOT). Neutron detectors to be used in these facilities are restricted to 0.184-in. OD x 40 in. long in the ISA, and less than 1.4-in. OD x 40 in. long in the INCOT Facility. Auxiliary cooling has not been provided in these facilities; thus the detectors must be able, as a minimum, to withstand the 700°F temperature of the bulk sodium coolant. The flux level at the in-core locations is approximately 2×10^{15} at 62.5 MWt. Miniature fission chambers, ion chambers, and self-powered prompt (cobalt core) detectors, with sufficiently small dimensions and required compatibility with the high

temperature and flux, are offered by several manufacturers. However, adequate tests of these detectors at the rated temperatures have yet to be completed, and development of these detectors will continue to be monitored.

Because of the necessary miniaturization and resultant loss of sensitivity for in-core detectors, the advantage of in-core over out-of-core detectors for boiling detection may not prevail in view of the adverse in-core environment.

2. Heat Transfer and Fluid Flow (R. P. Stein) (189a 02-097)

Analytical and experimental investigations of liquid-metal heat transfer and fluid flow in components and systems are conducted to provide information of immediate interest to the FFTF and LMFBR Programs. Fundamental studies in heat transfer and fluid flow also are conducted to improve current, or to devise new, engineering prediction methods essential to the advancement of reactor technology in general.

a. LMFBR Flow Stability Studies (R. Rohde)

This activity covers (1) the acquisition and analysis of experimental data on the vaporization and superheating of sodium in operating ranges (pressures, flow rates, temperatures, and equivalent diameters) and flow circuits of interest to the LMFBR Program; and (2) the determination, by both experiment and analysis, of two-phase flow phenomena related to flow stability. An LMFBR Simulation Heat Transfer Loop is being constructed for the experiments.

(i) Experiments with Superheat

Not previously reported.

A preliminary test plan has been completed. This plan includes: (1) the order of testing; (2) a step-by-step description of the test procedure; (3) a scheme for recording high- and low-speed data via a Hewlett-Packard data-acquisition system; and (4) some details relative to computations to be made on the system during testing.

D. Chemistry and Chemical Separations

1. Fuel Cycle Technology

a. LMFBR Reprocessing--Plutonium Isolation (D. S. Webster, A. A. Jonke, G. J. Bernstein) (189a 02-159)

(i) Centrifugal Contactors for Plutonium Handling

Last Reported: ANL-7776, pp. 88-89 (Jan 1971).

An experimental stainless steel centrifugal contactor having critically favorable dimensions for processing high-plutonium LMFBF fuel (ANL-7735, p. 84) has been installed in the centrifugal-contactor test facility. Balancing tests and preliminary performance tests have been done.

Vibration tests with no liquid flowing through the contactor were conducted at speeds up to 3500 rpm. Results showed that the rotor was well balanced and required no supplementary balancing. Vibration tests conducted with liquid flowing steadily through the contactor showed even less vibration than tests made with the system dry.

Other tests were made using 0.01M HNO_3 and Ultrasene (refined kerosene) as aqueous and organic phases to check the performance of the interface control system and the throughput capacity. At an organic-to-aqueous flow ratio of 1, total throughputs of 10, 14, and 16 gpm were achieved at rotor speeds of 2000, 2500, and 3000 rpm, respectively. Entrainment of either phase in the discharge stream of the other was 1-2%. A value of 1% entrainment is used as a reference in measuring maximum throughput of such units. Normal operation is generally limited to ~70% of the maximum.

Interface control by means of the air-controlled aqueous-phase weir was good. (Separations of the aqueous and organic phases occurs at the top of the rotor. An emulsion band at the interface between these phases must be positioned between the aqueous and organic weirs to minimize contamination of one phase by the other.) The location of the emulsion band could be shifted between the aqueous-phase underflow baffle and the organic-phase weir by adjustment of the weir air pressure between 0.4 and 2.0 psig.

Some flow surging was evident, accompanied by intermittent entrance of air with the inlet streams. It was observed that this phenomenon was more pronounced at higher rotor speeds and higher flow rates. Surging may be a result of the high pumping capacity of the contactor mixer-pump combined with the rotor. As a result, the standpipes on the inlet lines are pumped out, permitting air to enter in a cyclic pattern. The openings in the standpipes were sealed so that the standpipes operated as surge chambers and inflow of air was prevented. Thereby, a substantial reduction of the surging behavior was effected. Additional baffling in the mixing chamber is planned; this is expected to give more stable operation by reducing the pumping capacity.

- b. Molten Metal Decladding of LMFBF Fuels (D. S. Webster)
(189a 02-173)

A head-end liquid-metal process is under study in which stainless steel cladding is first dissolved in liquid zinc having an overlying salt layer, the resulting zinc-steel solution is separated from the unreacted

(U,Pu)O₂ fuel, and the fuel oxide is reduced to metal and dissolved in the reduction solvent. (This process may also be applicable for Zircaloy cladding.) Also being studied is melt decladding, which consists of heating fuel elements until the cladding melts and drains away from the fuel.

(i) Engineering Developments (R. D. Pierce)

Last Reported: ANL-7776, pp. 90-91 (Jan 1971).

(a) Reduction of UO₂ Pellets. A Zn-Mg/MgCl₂-CaCl₂-CaF₂ system, which was found to be excellent for the reduction of unfired UO₂ in the EBR-II fuel process, is being considered for the fuel-oxide reduction step. For sintered UO₂-PuO₂ fuels, it was found necessary to add calcium to Cu-Mg alloys (in work on the Salt Transport Process) to attain suitable reduction kinetics. Although the Mg-Cu-Ca/CaCl₂-CaF₂ reduction system would work for the present head-end step, a Zn-Mg system would be more attractive because of the lower cost of zinc and because the solvent metals could be removed from the dissolved fuel by vacuum evaporation if desired. In several reduction runs to determine whether calcium is also required with a Zn-Mg system, UO₂, a stand-in for (U,Pu)O₂, was reduced with Zn-Mg and Zn-Mg-Ca alloys. (UO₂ is somewhat more difficult to reduce than is PuO₂ or (U,Pu)O₂ in these systems.)

In a reduction run with Zn-30 at. % Mg/MgCl₂-47.5 mol % CaCl₂-5 mol % CaF₂, the reduction rate was low; only 89% of the uranium was reduced and dissolved in the alloy after agitation for 5 hr at 800°C. This system will not be evaluated further.

The remaining runs in this study will use Mg-Zn-Ca systems. High-zinc systems will give a product solution containing reduced uranium and plutonium; high-magnesium systems will give a product solution containing only the reduced plutonium, with the uranium metal present as a separate precipitated phase.

One reduction run was made with Mg-17 at. % Zn-4 at. % Ca and one reduction run with Zn-29 at. % Mg-6.6 at. % Ca to substantiate the earlier good results obtained in the reduction of sintered UO₂ pellets with these alloys (Runs Mg-Zn-R4 and Mg-Zn-R5, ANL-7765, pp. 78-79). Preliminary results indicate good reduction rates and complete reduction of UO₂. It has been concluded that Zn-Mg-Ca/CaCl₂-CaF₂ is a practical reduction system for the head-end process.

Although dissolution of one or both of the fuel actinides in the reduction solvents will be required in the reduction step, calcium has been found to suppress uranium solubility and is expected to suppress plutonium solubility in zinc-rich zinc-magnesium alloys. A single run has been completed to measure the effects of calcium additions on uranium solubility

at 800°C in Zn-14 wt % Mg. The uranium concentration in the solution decreased from 14.2 to 1.55 wt % as the concentration of calcium was increased from 0 to 11.5 wt %. For a process application where dissolution of uranium is desired, excess calcium could be removed following the reduction step by reaction with MgCl_2 or another oxidizing agent.

Since reduction salt is a waste stream, its quantity will be minimized. A few additional reduction runs are planned to establish the minimum requirement for salt in the reduction step. Another possibility is that CaO reduction product can be filtered or settled out, and a portion of the salt from each run recycled. Further work on the head-end process, including the runs for determining salt requirements, is estimated to require six additional reduction runs.

(b) Melt Decladding. Experiments have been started to investigate a melt-decladding concept in which stainless steel cladding is melted from a subassembly suspended vertically in an inductively heated region, causing the fuel pellets and molten steel to fall through a cold zone and onto a cold surface, where the metal drops solidify as discrete particles. In this concept, a mixture of steel and oxide particles is then fed to a nitric acid dissolver, where the fuel oxide is dissolved in preparation for the following solvent-extraction steps.

In a laboratory experiment completed during this period, a mock fuel element consisting of a $1\frac{7}{8}$ -in.-dia stainless steel tube containing UO_2 pellets was suspended in an inductively heated graphite tube. Upon melting of the steel, the steel and UO_2 pellets fell to a ceramic (firebrick) surface, which was inclined 32° from the horizontal. Although this apparatus was expected to divert the UO_2 pellets and discrete steel particles into a container at the base of the firebrick, most of the steel and oxide formed a solid ingot on the firebrick. The apparatus is being modified (1) to increase the distance that the steel drops fall and (2) to provide a steeper incline.

c. LMFBR Fuel Materials Preparation--U/Pu Nitrates to Oxides
(A. A. Jonke and N. M. Levitz) (189a 02-157)

Last Reported: ANL-7765, pp. 81-82 (Dec 1970).

A fluid-bed denitration process is under development for converting U/Pu nitrates in nitric acid solutions to mixed oxides suitable for the fabrication of fuel shapes.

(i) Phase Stability of $\text{UO}_2(\text{NO}_3)_2$ - $\text{Pu}(\text{NO}_3)_4$ Solutions. Work is under way to determine an appropriate composition for the feed solution for fluid-bed denitration. The feed solution should be as concentrated as possible to increase throughput, yet stable enough to avoid inadvertent

precipitation of plutonium salts and the associated criticality problems. Ten dilute nitric acid solutions containing uranium and plutonium in concentrations totaling 1 to 2M have been prepared for cooling-curve tests in the laboratory. Preliminary data obtained on crystallization temperatures of three of these solutions are given in Table II.D.1. These results indicate that the presence of plutonium in $\text{UO}_2(\text{NO}_3)_2\text{-Pu}(\text{NO}_3)_4$ solutions lowers by about 5°C the temperature at which crystallization starts in uranyl nitrate hexahydrate (UNH) solutions of equivalent metal-ion concentration.

TABLE II.D.1. Crystallization Temperatures of U-Pu- HNO_3 Solutions

<u>Solution Composition (M)</u>			Measured Crystallization Temp ($^\circ\text{C}$)	Crystallization Temp ^a ($^\circ\text{C}$) for Uranyl Nitrate Hexahy- drate (UNH)
U	Pu	HNO_3		
1.6	0.4	2	18.1	23
1.28	0.34	2	3.4	8
1.28	0.34	3.4	15.3	22

^a These values are interpolated from literature data for UNH-nitric acid solutions. The uranium concentrations are each equal to the sum of the uranium and plutonium concentrations in the corresponding experimental solution.

2. General Chemistry and Chemical Engineering

a. Thermophysical Properties of Reactor Fuels (A. D. Tevebaugh and P. E. Blackburn) (189a 02-162)

(i) Partial Pressures of Vapor Species in the U-Pu-O System and in the U-Pu-O System Containing Fission Products
(P. E. Blackburn)

Last Reported: ANL-7758, pp. 88-91 (Nov 1970).

Further mass-spectrometric studies of the volatilization behavior of the $\text{UO}_2\text{-PuO}_2$ fuel materials have been temporarily discontinued, and efforts are being directed toward studies of the reactions between sodium and fuel material. In particular, the studies are being directed toward determining the oxygen and sodium partial pressures [elemental activities of sodium-mixed oxide reaction products (e.g., Na_3UO_4 , Na_3PuO_4 , or $\text{Na}_3(\text{U,Pu})\text{O}_4$)].

The oxygen partial pressure in equilibrium with the three condensed phases, $\text{Na-(U,Pu)O}_2\text{-Na}_3(\text{U,Pu})\text{O}_4$, can be used with oxygen

pressure-composition-temperature data for $(\text{U,Pu})\text{O}_2$ to establish the equilibrium oxygen content of the oxide fuel. If the oxygen concentration of the fuel is kept below this level, there should be no reaction between the sodium and the fuel. The equilibrium oxygen pressure can also be used with oxygen pressure-composition-temperature data for sodium to obtain oxygen concentration levels in sodium, where reaction will not occur. We are studying the U-Na-O system first to establish procedures and to obtain data that will be applicable to $(\text{U,Pu})\text{O}_2$ fuel for low plutonium concentrations. In these investigations, the sample (9% UO_2 -91% Na_3UO_4) is contained in an iridium-lined tungsten Knudsen cell. The vapor effusing from the heated cell is analyzed with a Bendix time-of-flight mass spectrometer.

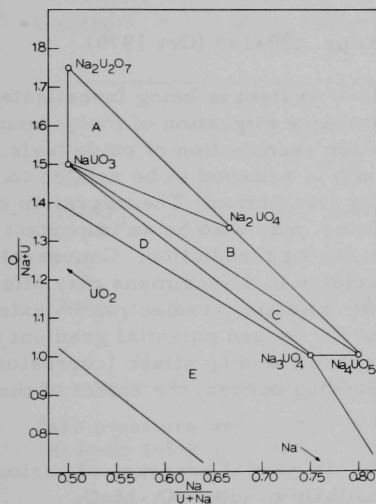


Fig. II.D.1. Portion of the Na-U-O Phase Diagram Showing the Phase Relations of the Compounds That Have Been Identified by X-Ray Diffraction

In ANL-7758, we showed that the oxygen pressure in equilibrium with $\text{Na-Na}_3\text{UO}_4\text{-UO}_2$ (region E in Fig. II.D.1) could not be measured directly. Thus we can measure only sodium pressures in three adjacent three-phase regions (B, C, and D) before reaching a region (A) where both sodium and oxygen pressures could be measured. This report gives the results of further measurements in the Na-U-O system.

A series of controlled experiments was conducted to establish a three-phase region that would be suitable for direct measurements of the sodium and oxygen partial pressures. The data for the first seven experiments (B1 to B7) were reported in ANL-7758 (p. 90), and 12 additional experiments have been performed. From analysis of the vapor-pressure and X-ray diffraction data, it appears that Experiments B1 to B3 apply to the three-phase region $\text{Na}_3\text{UO}_4\text{-Na}_4\text{UO}_5\text{-NaUO}_3$ (C in Fig. II.D.1); B4 and B5 apply to the region

$\text{Na}_4\text{UO}_5\text{-Na}_2\text{UO}_4\text{-NaUO}_3$ (B); B6 to B13 apply to the region $\text{NaUO}_3\text{-Na}_2\text{UO}_4\text{-Na}_2\text{U}_2\text{O}_7$ (A); B14 to B19 apply to the region $\text{NaUO}_3\text{-Na}_2\text{U}_2\text{O}_7\text{-X}$ (X is an unknown phase with lattice parameter $a = 4.3999 \text{ \AA}$). The partial pressure data for Na(g) in region A appear to be consistent, whereas the data for oxygen appear somewhat erratic and indicate the need for additional measurements.

A second series of measurements (C1 to C9) was conducted with the same procedure used in the first series. The objective of the second series was to establish firmly the partial pressure and heat of vaporization of Na(g) in regions B and C and, if possible, D. The data agree well with the previous results for regions B and C.

Because of the high partial pressure of Na(g) at low temperatures in regions D and E, a different cell arrangement is needed to obtain partial pressures and heat of vaporization. For this part of the study, iridium-lined platinum effusion cells have been fabricated and the effusion inlet system modified so that the temperature of the effusion cell can be measured with a Pt-Pt + 10% Rh thermocouple. This arrangement will also be used for additional measurements in region A, where the iridium-tungsten cell arrangement was not entirely satisfactory, since the high partial pressure of oxygen caused oxidation of the tungsten.

(ii) Total Effusion of Pu-O and U-Pu-O Systems
(C. E. Crouthamel and I. Johnson) (189a 02-162)

Last Reported: ANL-7753, pp. 139-140 (Oct 1970).

The chemistry of the U-Mo-O system is being investigated to provide a basis for understanding the extensive migration of molybdenum which has been observed in the postirradiation examination of oxide fuels. The migration of fission-product molybdenum is believed to be related to the local value of the oxygen potential during irradiation. The migration of molybdenum, as various gaseous oxide species, may also be an important mechanism for the redistribution of oxygen during irradiation. Conversely, the molybdenum spatial distribution in irradiated fuel specimens may offer a means for the reconstruction of the oxygen-potential gradient which existed in the fuel during irradiation. Knowledge of the oxygen potential gradient in the fuel will be useful in predicting the extent of cladding attack (corrosion), solid fuel swelling, and, if a break in the cladding occurs, the extent of the reaction of coolant sodium with the fuel.

In the present investigation, the partial pressure of various gaseous molybdenum oxide species in equilibrium with $\text{UO}_2\text{-MoO}_2$ mixtures are being determined as a function of the oxygen-to-metal (O/M) ratio and temperature. A combination of Knudsen effusion and mass spectrometry is being used for these studies.

Preliminary experiments have been completed to determine the general nature of the interaction of molybdenum oxide with hyper- and hypostoichiometric urania. Samples of MoO_2 , $\text{UO}_{2.08}\text{-10 wt \% MoO}_2$, and $\text{UO}_{1.96}\text{-10 wt \% MoO}_2$ were heated in an iridium-lined Knudsen effusion cell. The vapor over all the samples was found to be a mixture of the gaseous species MoO_3 , $(\text{MoO}_3)_2$, MoO_2 , and $(\text{MoO}_3)_3$. The ion currents observed for the four gaseous species were placed on a common basis of partial pressure by comparison with the data for the partial pressure of $\text{MoO}_3(\text{g})$ over the $\text{MoO}_2\text{-Mo}$ system reported by Burns *et al.** The results are given in Table II.D.2. It is seen that the partial pressures of all gaseous species

*R. P. Burns, G. DeMaria, J. Drowart, and R. T. Grimley, J. Chem. Phys. 32, 1363 (1960).

over the $\text{UO}_{2.08}$ - MoO_2 mixture are greater than those over the $\text{UO}_{1.96}$ - MoO_2 mixture or over pure MoO_2 , whereas the partial pressures of the gaseous species MoO_3 , $(\text{MoO}_3)_2$, and MoO_2 over the $\text{UO}_{1.96}$ - MoO_2 mixture are less than those over pure MoO_2 . These results indicate that some reaction occurs between urania and MoO_2 .

TABLE II.D.2. Relative Partial Pressures of Gaseous Species Over MoO_2 and UO_2 - MoO_2 Mixtures at 1195°C

Species	Relative Partial Pressures ^a Over		
	$\text{UO}_{2.08}$ -10 wt % MoO_2	MoO_2	$\text{UO}_{1.96}$ -10 wt % MoO_2
Relative Pressures ^a			
MoO_3	2.6	1.00	0.39
$(\text{MoO}_3)_2$	1.8	0.30	0.12
MoO_2	0.13	0.06 ₅	0.03
$(\text{MoO}_3)_3$	0.13	0.01 ₂	0.02

^aAll pressures were compared with the pressure of $\text{MoO}_3(\text{g})$ over MoO_2 -Mo ($\sim 5 \times 10^{-9}$ atm at 1195°C) reported by Burns.

The oxygen potential of hyperstoichiometric urania ($\text{UO}_{2.08}$) is about 35 kcal more positive than that of MoO_2 , and when the two oxides are heated together, some oxidation of the MoO_2 to a higher oxide would be expected. The oxidizing ability of $\text{UO}_{2.08}$ would not be sufficient to oxidize MoO_2 completely to MoO_3 ; hence the oxidation may halt at one of the solid oxide phases which have been reported between MoO_2 and MoO_3 . The intermediate oxide phase would be expected to have a higher oxygen potential than the MoO_2 -Mo system; consequently, the partial pressure of the gaseous MoO_3 species would be greater than in the MoO_2 -Mo system, as was observed experimentally (see Table II.D.2).

The oxygen potential of the hypostoichiometric urania ($\text{UO}_{1.96}$) is more than 100 kcal more negative than that of MoO_2 ; consequently, a significant reduction of MoO_2 would be expected when the mixture of oxides is heated. At the temperature of these experiments, stable suboxides of molybdenum are not expected. Therefore, the relatively low partial pressures of the gaseous species observed indicate a reaction of MoO_2 with urania. Whether this reaction involves solid solubility of MoO_2 in urania or the formation of a new solid phase has not been determined.

(iii) Phase Diagram Studies of the U-Pu-O System Containing Fission Products (Nonradioactive Isotopes)
(C. E. Crouthamel and I. Johnson)

Last Reported: ANL-7705, pp. 166-168 (June 1970).

The chemistry of the U-Pu-Cs-O system is under investigation to provide a factual basis for the understanding of the interaction of fission-product cesium with the UO_2 -PuO₂ fuel matrix under reactor operational conditions. This understanding will be useful in establishing oxide fuel specifications, for example, the initial oxygen-to-metal (O/M) ratio, and for predicting the useful life of a fuel element. Cesium appears to be a key fission-product element in the reactions involved in cladding attack and solid-fuel swelling.

In the present investigation, the activity of cesium in a mixed UO_2 -PuO₂ matrix will be determined as a function of the oxide composition and temperature. The cesium activity is expected to be significantly dependent on the oxygen potential of the system (O/M ratio), the cesium content of the solid phase, the nature (structure) of the solid phases, and the temperature. The cesium activity will be determined by the measurement of the partial pressure of cesium species in the vapor phase in equilibrium with known solid phases. A combination of Knudsen effusion and mass-spectrometric studies will be used to obtain these data.

Studies of the U-Cs-O system are under way to gain an overview of the interaction of cesium with a typical oxide-fuel system. An equimolar mixture of hyperstoichiometric urania ($\text{UO}_{2.075}$) and cesium oxide was heated in a sealed iron capsule at 1000°C for 75 hr. X-ray examination of the reaction product indicated the presence of UO_2 and Cs_2UO_4 . Samples of the reaction product were placed in a Knudsen effusion cell and heated over the temperature range from 590 to 806°C. The rate of vaporization into a vacuum and the composition of the vapor were determined simultaneously using a recording microbalance and a quadrupole mass spectrometer. Two experiments have been completed: In the first experiment, ~4.5 wt % of the sample was vaporized; in the second, 9 wt %. X-ray diffraction analysis indicated the presence of UO_2 and Cs_2UO_4 in the residue from the first experiment and UO_2 plus a very minor amount of an unknown substance in the residue for the second experiment.

In the two experiments, after a rapid initial weight loss of less than 1 wt %, the rate of weight loss was approximately the same at the same temperatures. The only gaseous (shutter-dependent) species observed during the effusion was cesium. A very low oxygen pressure was detected, but it was not shutter-dependent. In both experiments, at a given temperature, the rate of weight loss and the cesium ion current gradually decreased with time. For example, at 800°C, the cesium partial pressure (computed from the rate of weight loss) decreased from 3×10^{-4} to 8×10^{-5} Torr as the

total weight loss increased from 2.3 to 9.0 wt %. The cesium ion current exhibited a parallel decrease. The observed slowly decreasing cesium pressure at constant temperature suggests that the composition of one of the equilibrium solid phases is slowly changing. The O/M ratio of the urania produced by the decomposition of the Cs_2UO_4 is probably slowly increasing with the extent of reaction. This would lead to an increase in the oxygen potential and then to a decrease in the cesium pressure. On the assumption that the decomposition of Cs_2UO_4 involves the production of urania, gaseous cesium, and oxygen, the oxygen potential of the system was estimated. At 1070°K, the cesium pressure is approximately 2×10^{-7} atm and the calculated oxygen potential is -78 kcal/mol. This value of the oxygen potential corresponds to urania with an O/M ratio between 2.001 and 2.000. Thus, these preliminary results indicate that slightly hyperstoichiometric urania and Cs_2UO_4 may coexist at temperatures $\leq 800^\circ\text{C}$ with a very low cesium partial pressure.

- b. Physical and Chemical Studies-- Molten Fuel, Cladding, and Coolant (A. D. Tevebaugh and M. G. Chasanov) (189a 02-175)

Last Reported: ANL-7758, pp. 91-92 (Nov 1970).

- (i) Thermal Diffusivity of Reactor Materials: Liquid UO_2 .

Values of the thermal diffusivity of UO_2 in the liquid state are of importance to the reactor safety program. This information is needed to evaluate means of safely cooling the core of an LMFBR in the event of a meltdown incident. A knowledge of the thermal conductivity of liquid UO_2 will also be useful in determining the temperature distribution in the clad fuel under operating conditions.

We will determine the thermal diffusivity from the phase change in a thermal wave produced by heating the sample with a sinusoidally modulated electron beam. Two new electron-beam guns have been received and installed on the furnace and are now being tested.

PUBLICATIONS

Behavior of Countercurrent Liquid-Liquid Columns with a Liquid Metal
T. R. Johnson, R. D. Pierce, F. G. Teats, and E. F. Johnston
AIChE Journal 17, 14-18 (Jan 1971)

Pyrochemical Processing of Fuel Materials and Scrap Containing
Plutonium-238

P. A. Nelson, J. Fischer, J. F. Lenc, J. R. Haley, and J. D. Schilb
ANL-7709 (July 1970)

Recent Experimental Data for Heavy Nuclei

W. P. Poenitz

Proc. 2nd Int. Conf. on Nuclear Data for Reactors, Helsinki,
June 15-19, 1970, Vol. 2, pp. 3-29

Conversion of Uranium Dioxide to Uranium Carbide in an Induction Plasma
Torch Reactor

D. Ramaswami, J. R. Pavlik, and A. A. Jonke
ANL-7671 (Aug 1970)

On the Influence of Plastic Strain on Magnetomechanical Damping in Iron
and Nickel

J. T. A. Roberts

Phil. Mag. 23(181), 243-248 (Jan 1971)

The Nature of the Activation Volume-Stress Dependence in the High
Temperature Plasticity of UO_2

J. T. A. Roberts

J. Nucl. Mater. 38, 35-41 (Jan 1971)

III. NUCLEAR SAFETY

A. LMFBR Safety

1. Accident Analysis and Safety Evaluation (G. J. Fischer) (189a 02-112)

a. Initiating Accident Code Development (F. E. Dunn)

Last Reported: ANL-7753, p. 143 (Oct 1970).

(i) SAS2A Code. Coolant voiding due to fission-gas release from failed fuel pins is being incorporated into the multiple-bubble slug-ejection routine in the SAS2A accident-analysis code. Cladding failure is assumed to occur when the cladding becomes hot enough that the fission-gas pressure within the fuel pin exceeds the strength of the cladding. Then gas from the fission-gas plenum in the pin forms a bubble in the coolant channel. The rate of growth of the gas bubble is controlled by a user-specified orifice impedance between the gas plenum and the coolant channel, the inertia of the liquid slugs in the coolant channel, and the friction between the liquid slugs and the cladding. The temperature and pressure of the gas in the gas plenum and in the bubble are calculated.

Some of the effects of differences in fabrication or differences in power level between pins in the same subassembly are accounted for by dividing the pins in a subassembly into three separate groups, with a separate cladding-failure criterion for each group.

During a flow-coastdown type of accident, it is likely that sodium boiling and fission-gas release from failed fuel pins will occur simultaneously during part of the accident. Therefore, the multiple-bubble slug-ejection routine will be capable of treating fission-gas bubbles and vapor bubbles simultaneously.

b. Disassembly Accident Analysis, Including Computer Code Development and Sensitivity Studies (J. F. Jackson and R. B. Nicholson)

Last Reported: ANL-7758, pp. 95-97 (Nov 1970).

(i) Sensitivity Studies. The first phase of a study to evaluate the sensitivity of disassembly calculations to the pertinent parameters and initial conditions has been completed. This phase involved variations on a relatively low-yield excursion in which all the sodium coolant had been voided from the core before disassembly. The required initial conditions and reactivity insertion rate (\$20/sec) correspond to a flow-coastdown accident. The core composition was taken to be that of a typical FFTF "driver" assembly.

The disassembly calculations were performed using the VENUS* code. The initial conditions for such calculations must be obtained from an initiating-accident calculation, which is done, for example, by SAS1A or MELT-II. Because these codes treat such complex processes as sodium boiling and fuel meltdown, the power and reactivity history during the initiating phase is often very erratic and might vary greatly from one accident to another. Thus the VENUS code can be subject to great variations in the input initial conditions. These are temperature distribution, material distribution (especially sodium-voiding pattern), power level, reactivity, delayed-neutron precursor concentrations, and rate of reactivity increase. There is no explicit relationship between these VENUS input parameters. They are interrelated in a very complex way through the behavior during the initiating phase. In this study, we have treated them as parameters to be varied independently. Other parameters varied are the Doppler coefficient, the equation-of-state parameters, the prompt-neutron lifetime, and the pressure threshold for material motion.

The quantities of main interest in the sensitivity study are the total energy generated and the maximum pressure attained (exclusive of local pressure spikes). These quantities have a linear behavior with sufficiently small variations of the parameters. Of course, the behavior becomes nonlinear for large variations. Limitations on computer budget prevent the determination of the entire nonlinear sensitivity curves. We have had to choose variations of about the magnitude that we expect to be of most interest to most people. These are usually in the nonlinear range. In some cases, two or more variations have been made so that some indication of the extent of the nonlinearity is evident.

Table III.A.1 summarizes the results of these calculations. The results of the base case are given first, followed by the variations. The base-case value for each parameter being varied has been included for reference.

Although most of the variations should be self-explanatory from the table, the last four require further clarification. Three kinds of variations to the pressure function in the ANL equation of state have been considered. First, the entire function was multiplied by a constant factor. In the two-phase region of the equation of state, the following standard form is used:

$$P = \exp\left(A - \frac{B}{T} + C \ln T\right).$$

Variation by a multiplicative constant corresponds to varying the constant A in this expression.

*W. T. Sha and T. H. Hughes, VENUS: A Two-dimensional Coupled Neutronics-Hydrodynamics Computer Program for Fast-reactor Power Excursions, ANL-7701 (to be published).

TABLE III.A.1. Sensitivity Results for FFTF Flow-coastdown Accident

Parameter being varied	Variations	Total energy, MW-sec	Final pressure at core center, atm	Final temp. at core center, °K
(Base case) ^a		1580	35.7	4884
TdK/dT	-0.00125	2290	154.5	5629
(-0.0025)	-0.005	930	5.0	4196
Initial reactivity (\$1.01)	\$ 1.05	1800	60.0	5117
	\$ 1.10	2180	128.0	5520
Ramp rate (\$20/sec)	\$ 10/sec	938	8.0	4203
	\$ 40/sec	2550	235.0	5897
Initial power (61×10^3 W)	6.1×10^3 W	1980	88.0	5308
	610×10^3 W	1410	23.0	4703
Initial precursors (C_{i0})	$C_{i0} \times 0.01$	1590	36.9	4898
	$C_{i0} \times 10$	1650	43.0	4964
	$C_{i0} \times 100$	2410	171.0	5699
Initial temp. distribution	500°K Lower	2340	16.0	4565
	500°K Higher	480	5.52	4211
Heat capacity	1.2 x base	1890	34.6	4870
EOS pressure function	2 x base	1290	33.0	4580
	0.5 x base	1820	32.0	5149
	0.1 x base	2260	15.0	5616
Slope of vapor press. function	Base/1.2	1510	16.6	4811
	Base/2.0	935	2.3	4199
Total suppression threshold (0.0)	0.2 atm	1710	48.7	5022
	1.0 atm	1790	58.2	5105
Radial suppression threshold (0.0)	1.0 atm	1730	49.1	5025
	5.0 atm	1800	57.4	5098

^aBase-case values shown in parentheses.

The next most simple variation is to hold the pressure constant at some particular temperature and vary the shape of the P-T curve at that point so that (for example) pressures are higher than the base case at lower temperatures and lower at higher temperatures. This has been done by holding the same atmospheric boiling point and changing the slope at that point by the factors 0.5 and 2.0, respectively.

Finally, the motion of the reactor material has been suppressed until the pressure exceeds a given threshold. This has been done in two ways. First, the motion was totally restrained by suppressing all pressures below the threshold. Thresholds of 0.2 and 1.0 atm were considered in this case. Second, only the radial motion was suppressed, and the axial motion was permitted to continue. This was done by restraining the radial motion of each mesh-cell boundary until the pressure difference

across the boundary exceeded the threshold. After this had occurred, the boundary was free to move throughout the remainder of the calculation. This was intended to simulate the low-pressure radial restraint offered by the subassembly structure. These are the final results given in the table.

2. Coolant Dynamics (H. K. Fauske) (189a 02-114)

a. Sodium Superheat (R. E. Henry, R. E. Holtz, and R. M. Singer)

Last Reported: ANL-7776, pp. 96-101 (Jan 1971).

(i) Incipient-boiling Tests with EBR-II Sodium. The incipient-superheat tests with EBR-II primary sodium have continued. Approximately 200 test runs have been conducted by using an electromagnetic pump to pressurize the system. These tests have supplied the following information:

(a) A large incipient-boiling superheat can result in the boiling surface losing a previously established pressure-temperature history. The proposed mechanism by which this occurs is a large thermal stress at the boiling surface caused by the severe temperature gradient at the boiling surface during vaporization. This large thermal stress results in plastic deformation of the boiling surface (i.e., surface cracking).

(b) If the pressure-temperature history is reestablished for at least 20 min before each test run, the incipient-boiling superheats show good agreement with the pressure-temperature modeling technique* if a ratio for the receding-to-advancing radii of curvature in the range between 0.34 to 0.50 is used. This range for the ratio of receding-to-advancing radii is in excellent agreement with recent contact-angle data.**

(c) The incipient-boiling superheat appears independent of the approach to boiling. Data obtained approaching boiling both by increasing the temperature at constant pressure and by decreasing the pressure at constant temperature are in agreement.

Additional incipient-superheat test runs are being conducted. More detailed reporting of all the data will be included in future progress reports.

(ii) Model of Incipient Boiling during Forced Convection.

To examine the possible mechanisms that might reduce the incipient-boiling superheat of liquid metals in forced-convection flow, the roles of turbulent pressure and temperature fluctuations have been studied in an elementary fashion.

*R. E. Holtz, The Effect of the Pressure-Temperature History upon Incipient-boiling Superheats in Liquid Metals, ANL-7184 (June 1966).

**M. J. Todd and S. Turner, The Surface Tension of Liquid Sodium and Its Wetting Behavior on Nickel and Stainless Steel, TRG Report 1459(R) (1968).

During the nonadiabatic turbulent flow of a fluid, velocity fluctuations cause pressure and temperature to fluctuate. Furthermore, it has been reasonably well established that a high positive correlation exists between the velocity and pressure fluctuations, and that a high negative correlation exists between velocity and temperature fluctuations. Therefore, it can be inferred that a high negative correlation exists between pressure and temperature fluctuations; i.e., the maximum instantaneous temperature occurs simultaneously with the minimum instantaneous pressure, and vice versa. Such a situation can affect boiling inception, because vapor growth is favored by a lowering of liquid pressure and by an increasing of liquid temperature. The frequency of these fluctuations is also of considerable importance, because there might not be sufficient time available for net vapor growth to occur during "very rapid" temperature and pressure fluctuations. However, because this analysis is only exploratory, i.e., gross effects are being searched for, it will be assumed that the frequency of the fluctuations are unimportant insofar as vapor growth is concerned.

For a vapor bubble to nucleate from a vapor- and/or gas-filled cavity, the pressure difference across the vapor-liquid interface must exceed the surface-tension forces. At incipient nucleation, this requirement can be expressed as

$$P_V(T_L) + P_G - P_L = \frac{2\sigma(T_L) \cos \theta}{r}, \quad (1)$$

where P_V , P_L , P_G are the vapor, liquid, and gas partial pressure, respectively, T_L is the liquid temperature, σ is the surface tension, θ is the liquid-vapor-solid contact angle, and r is the radius of the cavity under study. During turbulent flow, the liquid pressure and temperature can be expressed as the sum of their mean and fluctuating values as

$$P_L = \bar{P}_L + p \quad (2)$$

and

$$T_L = \bar{T}_L + t, \quad (3)$$

where the barred quantities are the means, and p and t are the fluctuating components. Considerable data have been presented concerning these fluctuations, especially of the pressure. The pressure data have usually been presented in terms of the rms value of p relative to the dynamic pressure, i.e., as

$$\gamma_P = \sqrt{\langle p^2 \rangle} / \frac{1}{2} \rho u^2, \quad (4)$$

where γ_P is the turbulent-pressure-fluctuation coefficient, and ρ and u are the liquid density and velocity, respectively. Most of the measurements

made in simple geometries (pipes, flat plates, etc.) indicate that γ_P is in the range of 0.005-0.008 with only a slight dependence on the Reynolds number in the range of $2 \times 10^4 < Re < 2 \times 10^6$. However, some recent data obtained in Germany* in a 37-pin bundle with spacer grids resulted in a value of $\gamma_P \approx 0.19$ at $Re \approx 1.4 \times 10^4$ that gradually decreased to $\gamma_P \approx 0.07$ at $Re \approx 3.9 \times 10^4$.

There seem to be fewer data available on the turbulent temperature fluctuations, but some are reported for an unidentified liquid metal by Russian workers.** In that case, a turbulent-temperature-fluctuation coefficient γ_T is defined as

$$\gamma_T = \sqrt{\langle t^2 \rangle} / (T_W - \bar{T}_b) \quad (5)$$

where T_W and \bar{T}_b are the wall and mean bulk liquid temperatures, respectively. This coefficient decreased from 0.17 at $Re = 2.5 \times 10^4$ to 0.062 at $Re = 2.2 \times 10^5$. In other investigations,[†] the maximum value of γ_T occurred a short distance away from the heated wall, with γ_T decreasing significantly as the wall is approached.

In the application of these measurements to the nucleation conditions, the fact that the pressure and temperature fluctuations have a negative correlation (which will be assumed to equal -1) will be taken advantage of so that we will use

$$P_L = \bar{P}_L - \gamma_P(\frac{1}{2}\rho u^2) \quad (6)$$

and

$$T_L = \bar{T}_L + \gamma_T(T_W - \bar{T}_b) \quad (7)$$

in Eq. 1 to compute the minimum value of the mean temperature at which boiling will start. In applying the temperature fluctuations, we further note that $T_W - \bar{T}_b$ can be related to the Nusselt number Nu as

$$T_W - \bar{T}_b = \frac{qd}{kNu}, \quad (8)$$

where q is the heat flux, d the channel diameter, and k the liquid thermal conductivity. Thus, combining Eqs. 1, 6, 7, and 8, we obtain

$$P_V \left(\bar{T}_L + \frac{\gamma_T qd}{kNu} \right) + P_G - \bar{P}_L + \gamma_L(\frac{1}{2}\rho u^2) = \frac{2\sigma(\bar{T}_L) \cos \theta}{r}, \quad (9)$$

*J. Kadlec and W. Lang, Flow Induced Temperature and Pressure Pulsations in Rod Bundles, Kernforschungszentrum Karlsruhe Report KFK-1157 (Apr 1970).

**V. I. Subbotin et al., Measurement of Turbulent Temperature Pulsations in Liquid Flow, Teploenergetika 3, 64-67 (1962).

†S. Tanimoto and T. Hanrathy, Fluid Temperature Fluctuations Accompanying Turbulent Heat Transfer in a Pipe, Chem. Eng. Sci. 18, 307-311 (1963).

where it has been assumed that only insignificant variations in the surface tension σ result from the temperature fluctuations.

To examine initially the magnitude of the effect of these fluctuations on the incipient-boiling superheat, the coefficients γ_P and γ_T are treated as constant parameters. Additionally, because the Nusselt number for liquid metals is known to be essentially constant at a value of about 7.0 in turbulent flow for Peclet numbers less than about 100-200, this constant value of 7.0 will be used in the present calculations.

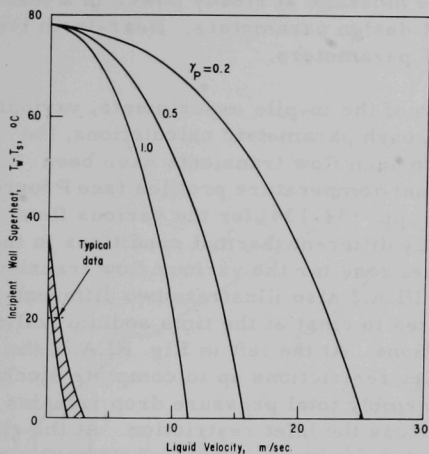


Fig. III.A.1

How Turbulent Pressure Fluctuations Can Reduce the Incipient Superheat. γ_P is the pressure-fluctuation coefficient. The temperature fluctuation coefficient γ_T is 0, saturation temperature T_s is 870°C, cavity size R is 2.5 μm , and gas partial pressure P_G is 0.

ception. However, the velocities necessary for these fluctuations to become significant are at least an order of magnitude more than those observed in experimental studies in which approximately zero superheat resulted for velocities of about 1-2 m/sec. In addition, the shape of the curve of superheat versus velocity as calculated here is of a distinctly different character than that measured experimentally.

Based on these observations, it seems as though the measured reductions in the incipient superheat with increasing velocity are not caused by turbulent fluctuations, and an alternative explanation is required, such as the "favored nucleation site" hypothesis.*

- b. Sodium Expulsion and Reentry: In-pile (M. A. Grolmes and H. K. Fauske)

Last Reported: ANL-7753, p. 145 (Oct 1970).

*H. K. Fauske, R. E. Holtz, and R. M. Singer, An Interpretation of the Reported Velocity and Heat Flux Effects in the Incipient Boiling of Liquid Metals, submitted to ASME (Jan 1971).

(i) Planning of In-pile Test Vehicles. Integrated in-pile (TREAT reactor) experiments are being planned to determine the overall consequences of coolant expulsion and reentry as they effect fuel failure and potential interactions of molten cladding, fuel, and coolant. For these tests, coolant expulsion will be specifically initiated by flow transients such as a coastdown and partial or complete blockage at steady power in a test vehicle that simulates current LMFBR design parameters. Near-term tests will be directed to simulation of FFTF parameters.

To meet the objectives of the in-pile experiments, various flow transients have been defined. Through parametric calculations, the fuel, cladding, and coolant responses to such flow transients have been analyzed for FFTF parameters. Coolant-temperature profiles (see Progress Report for September 1970, ANL-7742, pp. 133-134) for the various flow transients have illustrated the markedly different thermal conditions in the coolant downstream from the active fuel zone for the various flow transients. Pressure axial profiles shown in Fig. III.A.2 also illustrate two different hydraulic conditions that can be expected to exist at the time sodium boiling occurs for various loss-of-flow conditions. At the left in Fig. III.A.2, the pressure axial profiles for several inlet restrictions up to complete blockage are shown; for these cases, the subassembly total pressure drop remains constant with a large fraction taken across the inlet restriction. At the right in Fig. III.A.2, the pressure axial profiles for various reduced flows through the subassembly show the very low pressure drop across the subassembly. These different hydraulic conditions could also influence the voiding rate after coolant boiling takes place. This is especially apparent with respect to upstream propagation of coolant voiding.

For inlet partial restriction, the magnitude of inlet restriction required to cause coolant boiling at the subassembly exit was determined to be approximately 0.93 (area blockage fraction) for approximate FFTF conditions. Figure III.A.3 shows the variation of flow and sodium-temperature rise with inlet blockage fraction. A 75% inlet-area restriction is required for an ~20% increase in subassembly exit temperature for these conditions. Beyond the point of blockage required for coolant boiling, it remains to be determined whether the resulting two-phase flow through the subassembly is stable and follows dashed Curve A in Fig. III.A.3 or is, in fact, unstable (following Curve A') and leads to a boiling crisis and subassembly boiling. Calculations are being made to determine the stability of the resulting two-phase flow. These analyses will lead to a determination of the types of flow transients and inlet restriction that should be carried out as part of an in-pile loss-of-flow study.

c. Liquid-Vapor Dynamics (M. A. Grolmes and H. K. Fauske)

Last Reported: ANL-7776, pp. 101-102 (Jan 1971).

(i) Liquid-film Thickness and Breakup. Experiments have been carried out and previously reported for the determination of the liquid-film

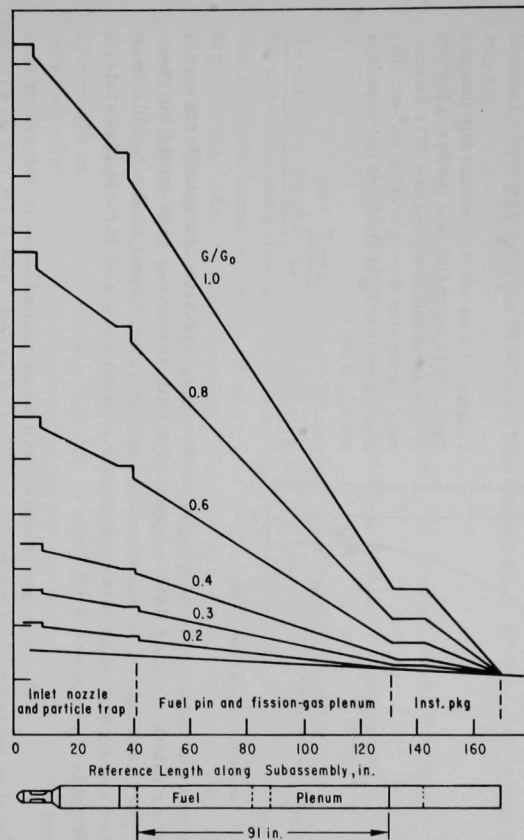
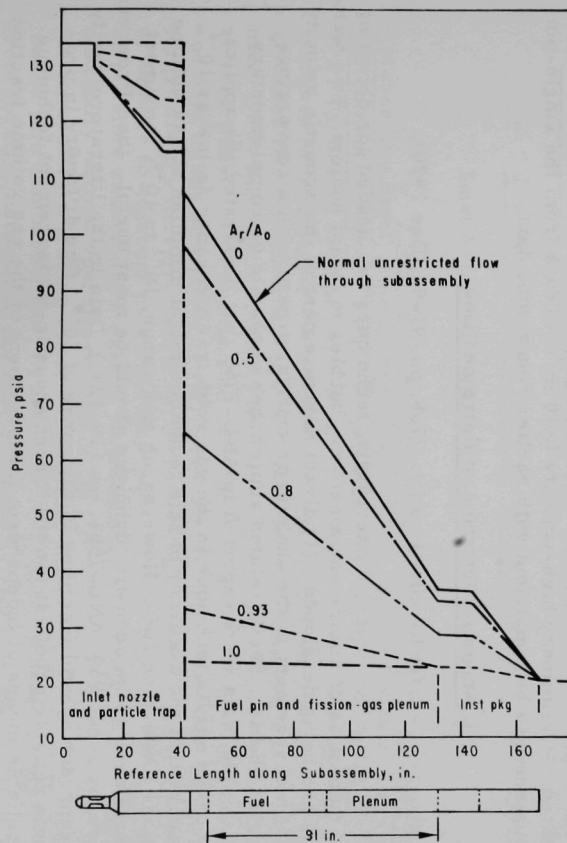


Fig. III.A.2. Pressure Axial Profiles for Flow Restriction and Complete Blockage at Lower Fuel-pin Grid Plate (left) and Flow Coastdown (right) for Approximate Parameters of FFTF Driver Fuel. A_r/A_0 is area restriction ratio. Steady-state flow G_0 is 1250 lb_m/ft²-sec; the coolant boils at $G/G_0 \approx 0.3$.

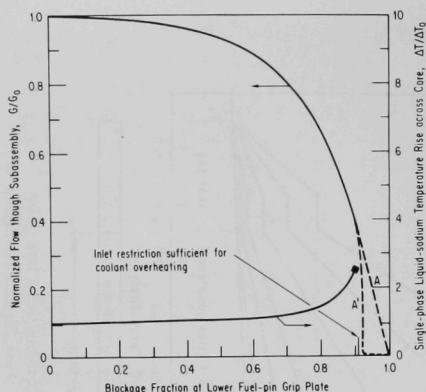


Fig. III.A.3

Variation of Flow and Temperature Rise through a Typical FFTF Driver Fuel Subassembly as a Function of Inlet Restriction for Approximate FFTF Parameters. Steady-state flow G_0 is $640 \text{ g/cm}^2\text{-sec}$, the inlet sodium is at T_{in} of 312°C , and the temperature rise ΔT_0 is 200°C .

thickness characteristic of single-bubble slug ejection from uniform-diameter tubes. These data suggested a film thickness that could be related to the turbulent velocity profile in the liquid ahead of the bubble in a manner consistent with interpretations of data obtained for steady-state, multibubble, two-phase slug flow.

These experiments have been extended to more complex geometries including a single-pin annulus, a seven- and a 19-pin unwrapped test assembly. Film-thickness results from these test sections are being evaluated. Preliminary high-velocity ($\geq 10 \text{ m/sec}$) data from the single-pin annulus seem to be consistent with earlier round-tube data.

(ii) Acoustic Detection of Entrained Gas

Last Reported: ANL-7765, pp. 91-92 (Dec 1970).

As reported previously, techniques are needed for detecting small quantities of minute entrained-gas bubbles in liquid sodium. Two techniques are being developed: (1) direct measurement of the acoustic velocity and (2) measurement of the choking or critical pressure in a converging-diverging nozzle. These related approaches appear to be complementary. For example, data were reported in ANL-7765 that illustrated the applicability of the nozzle technique in the gas void-fraction range as low as 10^{-2} . It appears that the accuracy of this technique might diminish at gas volume fractions lower than 10^{-3} . However, in this range, 10^{-3} to 10^{-6} , the direct measurement of the acoustic technique should be most useful. (See Progress Report for June 1969, ANL-7581, pp. 119, 121.) Data in the literature verify this approach at void fractions in the range of 10^{-4} . One difficulty in providing a reliable proof test for the direct acoustic-measurement technique is a reliable means of independent measurement of the gas volume fraction at such low levels. A test apparatus has just been completed for the determination of acoustic velocity in gas-liquid systems at such low gas volume

fractions. Water will be used in which the gas will be hydrogen released from electrodes by the electrolysis of water. In this apparatus, it should be possible to make direct acoustic-velocity measurements where the extremely low gas volume fractions are determined by the electrolysis current.

d. Sodium Simulations (H. K. Fauske and M. A. Grolmes)

Last Reported: ANL-7737, pp. 156-160 (Aug 1970).

(i) Transient-flow-regime Studies of Combined Expulsion and Reentry in Single- and Multiple-pin Geometries in Flowing Systems. A test facility has been designed and assembled and is approaching completion for the study of expulsion and reentry flow regimes in a single-heated-pin flowing system. Many glass parts are used in this apparatus to permit the direct visualization of flow regimes and other transient phenomena such as heater-surface dryout and possible rewetting. Either refrigerants or water will be used at low pressure. Liquid expulsion as a result of complete and partial inlet-flow restrictions as well as of gradual flow reduction will be studied. The mode of operation of this facility is expected to parallel closely, on a smaller scale, anticipated operating modes for future out-of-pile and in-pile sodium-expulsion and reentry tests.

3. Fuel Dynamics Studies in TREAT (C. E. Dickerman) (189a 02-117)

a. Transient In-pile Tests with Ceramic Fuel (C. E. Dickerman)

Last Reported: ANL-7776, pp. 107-110 (Jan 1971).

(i) First Mark-II-loop Experiments (D1 and D2) on Effects of Release of a Small Amount of Molten Fuel, Using Pins with Local High-enrichment Sections. The fuel-dynamics experimental program in support of FFTF design and analysis includes a series of Mark-II-loop experiments designed to investigate the behavior of small amounts of molten-oxide fuel released from a failed fuel pin into the flowing sodium coolant. Experiment D1 is the first of this series and is intended to survey the actual fuel-release phase. The mechanism and causes of release must be determined, and data on the conditions required for release are required. Also of interest are the movement of fuel after release into the coolant, and the extent of damage to adjacent pins resulting from fuel release. Conditions viewed as possible causes of release of small amounts of molten fuel include, at nominally normal operating conditions, a local section of high-enrichment fuel caused by a loading error, a complete pin of incorrect enrichment loaded into a subassembly, or a local flow blockage, such as might result from foreign material in the coolant, spacer-wire breakage, or fuel swelling. In addition, a small-reactivity-insertion accident could result in local release of molten fuel near the midplane without gross fuel movement or failure.

The D1 experiment is intended to simulate the most severe conditions encountered by an FFTF fuel pin during steady-state operation with a seven-pin cluster of prototypical pins similar to the PNL-17 design, containing only UO_2 fuel. The cluster is a pin-centered array with graded fuel enrichments to produce, as nearly as possible, uniform power in the cluster. The peripheral pins contain 20%-enriched fuel; the central pin contains 26%-enriched fuel, with a 1.5-in.-long section of 93%-enriched fuel located about the axial midplane. The power level, inlet temperature, and coolant flow rate are selected to simulate the conditions at the mid-section of the hottest FFTF pin at 120% power as estimated from FFTF data. Some departure from strict simulation is necessary to adjust for differences between a seven-pin test cluster and the larger reactor sub-assemblies. Peak pin linear power at 20% reactor overpower is 14.6 kW/ft, maximum average linear power at 20% reactor overpower is 11.8 kW/ft, sodium mass flow rate per pin is 830 lb_m/hr , and reactor inlet temperature is 600°F. From these data, we derive the results that average temperature rise in the coolant at 11.8-kW/ft input is 160°F/ft, temperature rise to inlet of the 13.5-in. section centered in the pin is 150°F, and experiment inlet temperature is 750°F.

Because the ratio of fuel cross-sectional area to flow area for the cluster is only 61% of that for a pin in a subassembly, the flow should be reduced to obtain the correct "mixed" temperature rise. The experiment flow rate is calculated as reactor mass flow rate of 830 lb_m/hr , reactor mass velocity of 1277 $\text{lb}_m/\text{sec-ft}^2$, experiment mass velocity of $0.61 \times 1277 = 779 \text{ lb}_m/\text{sec-ft}^2$, sodium density at 750°F of 53.467 lb_m/ft^3 , and experiment coolant velocity of 14.6 ft/sec or 445 cm/sec.

To obtain a linear power of 14.6 kW/ft in the "normal" part of the central pin, in which there is 57 g of fuel per foot of pin, the experiment specific power must be 1460/57 or 256 W/g, the reactor power calibration factor for 26%-enriched fuel in central pin must be 3.36 W/g-MW, and the required power of the TREAT reactor is 76 MW.

The linear power rating of the fully enriched central portion of the central pin is $14.6(7.47/3.36) = 32.4 \text{ kW/ft}$, which is about 20% lower than the value of 40 kW/ft on which previous calculations have been based. The lower power is necessary to provide the best possible simulation of FFTF conditions.

The seven-pin cluster of fuel elements is retained in a specially designed fuel holder that locates the pins in the Mark-II loop and simulates, to the maximum extent practical, the adjacent fuel pins in a sub-assembly. The remainder of the test-train hardware is the same as used previously. Instrumentation consists of inlet and outlet flowmeters, inlet and outlet pressure transducers, inlet and outlet sheathed thermocouples in the loop sodium, and the neutron hodoscope. The loop for D1, the "A1" loop, has been shipped to TREAT. The test train was shipped previously.

(ii) First Mark-II-loop Experiment (H3) on Transient Failure Threshold of Irradiated (5% Burnup) Mixed-oxide Fuel. Scheduling of the H3 test is being revised to match changes in the XX02 instrumented subassembly (PNL-17) irradiation schedule in EBR-II. Current plans for the EBR-II irradiation call for the instrumented subassembly to receive an additional 1.5 reactor runs before being removed at the end of Run 48. The H3 test is to use a pin irradiated in XX02.

b. Experimental Support (M. B. Rodin)

Last Reported: ANL-7776, pp. 110-111 (Jan 1971).

(i) Cask Fabrication. The manufacturer has submitted copies of all required procedures and drawings for ANL approval. All except the copper-spray procedure have been accepted. Material for all major components has been received by the manufacturer, and machining operations have been started. Casting and machining of uranium shield parts have been initiated. An ANL procurement representative visited the manufacturer's plant February 3 and 4 to inspect materials and machining operations.

As an interim measure pending delivery of the Mark-II-loop cask, the Savannah River plant has designed and built a "special form" container for use within the single-element Yankee shipping cask. This package is to be available for short-term use in shipping Mark-II TREAT loops containing failed fuel. Approval documentation is to be sent to ANL for review. The cask and special-form container will be checked physically before use.

(ii) As-built Design and Development Report on First Group of Mark-II Loops. A report is being prepared to describe the design and development of the Mark-II loops; it will have an as-built description for the first ten loops.

(iii) Preparation of Last Six Mark-II Loops from FY 1970 Stocks. The Mark-II Loop A3 has been delivered. The A4 loop has been assembled and is being inspected. All components for the stator of the A4 annular linear-induction pump have been completed, and pump assembly has begun. Pump tubes for both the A3 and A4 ALIP are scheduled to be heat-treated (i.e., age-hardened) and installed soon. Assembly operations on the A5 and A6 loops have been suspended pending availability of funds.

(iv) Preparation of Mark-II Loops for Use in FY 1972 Tests. A preliminary layout for the Mark-II-C loop (stretched Mark II) has been reviewed by experimenters. A detailed layout is being prepared to incorporate necessary revisions.

(v) Preparation of Handling Equipment for Routine Alpha-cave Operations on Mark-II Loops. Fabrication of the transfer port for handling Mark-II sodium loops at the FEF argon glovebox has been completed. Following operational checkout, it, together with the loop support table, will be shipped to FEF for installation on the glovebox.

c. Analytical Support (A. B. Rothman)

Last Reported: ANL-7776, pp. 111-116 (Jan 1971).

(i) Automated Handling of Hodoscope Data. Most of the problems associated with conversion of the hodoscope film-record scanning from

CHLOE to ALICE have now been unraveled, and the films from Transients 1281, 1317, 1322, 1346, 1348, and 1329 have been scanned. ALICE output for these transients are being processed through the CDC-3600; the quality of reconstruction of fuel motion depends on the chronological order of scanning, the quality of the scan, the quality of the image, and the peak power level. In some cases, the images on the film from TREAT lack all the fiducials, which raises severe requirements in data reduction. Because the ALICE scanning still lacks the x/y linearity of CHLOE, it is further necessary to take special measures to avoid loss of data. Finally, those transients that experience scaler overflow, which at the moment will be every transient whose peak exceeds several hundred MW, require operation of an automatic overflow provision in the computer coding. Development of this correction routine is under way.

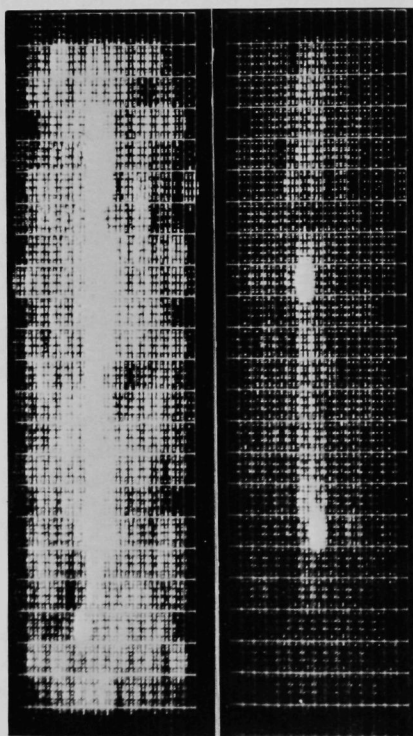


Fig. III.A.4

Computer Reconstruction of Fuel Positions at Two Instants (3.60 sec at left, and 4.32 sec at right) in the Meltdown History of an FFTF Prototype Pin in Test H2 during Transient 1317

Computer reconstructions of fuel positions at two instants in the meltdown history of Transient 1317 are shown in Fig. III.A.4 as an example of hodoscope status. This is Test H2 on an FFTF prototype pin. In the hodoscope time scale, the peak power was at about 4.0 sec with a full-width-at-half-maximum of about 0.2 sec.

At 3.60 sec, the pin appears to be intact. In particular, observe that the pin is not initially above Row 3. (There are no detectors in Row 1.) Despite the fact that there was a special boron thermal-neutron filter inside the loop can, the pin stands out strongly against the background of the sodium loop. At 4.32 sec, which follows the peak, some fuel can be seen to have moved into the space above the original pellet location. The transient was intended to induce mild failure so as to provide a more accurate determination of failure threshold. The data from these two computer-drawn film frames indicate the use of the hodoscope to augment postmortem inspections, which cannot yield the timing of fuel movements. Data close to the peak power show evidence of overflow and are still being analyzed. (The voided area in Row 7 corresponds to a region of voided fuel, as determined from the posttest radiograph of the test section.)

(ii) Analysis of Transient In-pile Experiments. Several transient irradiation experiments on fast-reactor fuel failure have been completed in TREAT using Mark-II loops to provide a flowing-sodium environment. In each of these experiments, the test fuel elements were exposed to a short power burst that caused failure of the pins and dispersal of the fuel into the sodium coolant. One quantity that can be derived from the experimental data is the fraction of the available fission energy converted to work on the coolant.

Release of hot fuel from the pins into the coolant generally results in boiling and subsequent ejection of sodium from the region adjacent to the fuel. Work done on the coolant shows up as (1) increased coolant kinetic energy, (2) work done in compression of the cover gas in the loop plenum, (3) work done in overcoming the pumping forces, and (4) work done in overcoming fluid friction. The Mark-II loop is equipped with electromagnetic flowmeters at the inlet and outlet of the fuel region. The data obtained from these flowmeters are used, along with the equations of fluid mechanics and thermodynamics, to estimate the work components. It is assumed that the flow is one-dimensional and continuous, except for a vapor bubble in the fuel region.

The coolant kinetic energy is a function of the instantaneous velocities measured at the flowmeters, and is evaluated by summing the kinetic energy of the sodium in the several constant-area subdivisions into which the flow path can be divided. Expansion of a vapor bubble in the fuel region requires compression of the cover gas in the loop plenum. The volume increase is determined by integrating the coolant velocities with respect to time, and the equations of adiabatic compression are applied to determine the work necessary to accomplish the expansion. Work is done by the expanding vapor bubble against the pumping forces if flow through the pump is reversed. The work done is evaluated by assuming the force necessary to move sodium back through the pump to be determined by the shutoff head of the pump. The work done against friction is evaluated by calculating the

hydrodynamic energy losses according to the usual equations of fluid flow. In this calculation, it is necessary to determine both the coolant velocities and locations of boundaries of the liquid slugs.

As can be seen, the calculation is dynamic in character, with both the energy appearing in the coolant and that resulting from coolant motion, and the available fission energy changing with time. Typical results are given in Table III.A.2 for the first three tests producing failure. Friction is not included in these results. These results were derived by selecting the time at which the work done appeared to be at its maximum.

TABLE III.A.2. Typical Energy Conversion in Mark-II-Loop Experiments^a

	Experiment		
	E2	H2	E3
Geometry	1 pin plus 6 dummy pins	1 pin	3 pins preirradiated
Test fuel	UO ₂	Mixed oxide	UO ₂
Coolant kinetic energy, J	2	1	29
Initial coolant kinetic energy, J	5	Negligible	Negligible
Work done in plenum gas, J	101	43	61
Work done against pump, J	9	Negligible	5
Total, J	107	44	95
Energy available, J	2.1×10^5	9.3×10^4	5×10^4
Conversion, %	0.05	0.05	0.19

^aFluid friction not included.

4. High-temperature Physical Properties and Equation-of-state of Reactor Materials (M. G. Chasanov) (189a 02-119)

a. Theoretical Extrapolation of Measured Physical Properties to Very High Temperatures (M. G. Chasanov)

Last Reported: ANL-7758, p. 116 (Nov 1970).

As part of the calculations of fuel and fission-product vapor pressures in LMFBR fuel pins, information is gained concerning the oxidation state (or O/M ratio) of the condensed fuel material. With the assumption of ideal solution of all condensed oxides and metals in their respective phases, we have calculated a linear increase in postburnup O/M ratio of 0.0054 units per at. % burnup for fuel of initial composition (Pu_{0.2}U_{0.8})O_{1.98}

at 2500°K for up to 7 at. % burnup. Thereafter the rate of increase is greatly diminished and is nearly zero above 8.5% burnup, corresponding to $O/M = 2.021$ and $p(O_2) = 7.79 \times 10^{-5}$ atm. The explanation lies in the fact that the phase boundary for the fission product molybdenum lies at the above value of the oxygen pressure. The oxygen released by further fissioning of the fuel cannot increase its O/M ratio until all the molybdenum is converted to its stable oxide phase. These predictions are supported by microprobe analyses of irradiated fuel pins in which it has been observed that both metallic and oxide phases of molybdenum are seen after quenching.

b. High-temperature Physical-property Studies (M. G. Chasanov)

Last Reported: ANL-7742, pp. 142-143 (Sept 1970).

(i) Matrix-isolation Spectroscopy of Uranium Oxides. A program has been undertaken to determine the thermodynamic functions of gaseous uranium-oxide species at high temperatures. These thermodynamic properties, in conjunction with measured or suitably extrapolated properties of the condensed oxide fuel phase, can be used to predict fuel partial vapor pressures under conditions of importance to the reactor safety program.

The method chosen to calculate the requisite thermodynamic functions for the gaseous species is the application of standard computational techniques to the molecular parameters of the urania vapor species, according to the principles of statistical mechanics. The molecular parameters needed for these calculations can be determined from the infrared, visible, and ultraviolet spectra of the species of interest.

Because insufficient amounts of vapor exist in equilibrium with the condensed phase at temperatures suitable to conventional spectroscopic sampling apparatus, the technique of matrix isolation is being used. A beam of vapor species emanating from a tungsten Knudsen cell containing $UO_{2\pm x}$ and heated to ~2200°K impinges, together with an inert gas, onto an optically transparent substrate kept at a temperature low enough (15°K) to prevent diffusion of the matrix molecules after condensation. The high dilution ratio of matrix-to-sample molecules virtually eliminates intermolecular interactions between sample molecules. The resulting spectra obtained from such samples are consequently similar to those of gaseous species.

Preliminary measurement of the infrared spectrum of uranium oxide species is shown in Fig. III.A.5. Strong transitions were observed at 776, 746, and 853 cm^{-1} . Weaker features are also noted at 801, 818, 840-850, and 871 cm^{-1} . Work is under way to assign these features to the appropriate uranium-oxide species by varying their relative concentrations through control of the temperature and O/M ratio of the condensed phase.

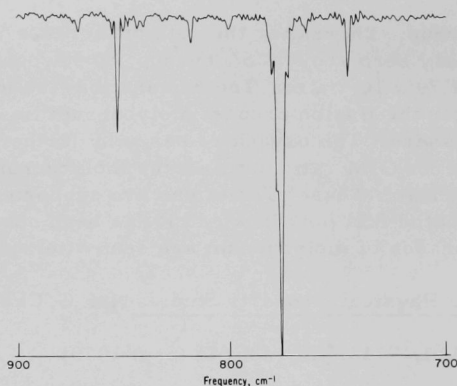


Fig. III.A.5

Infrared Spectrum of Matrix-
isolated Uranium Oxides

5. Fuel-Coolant Interactions (R. W. Wright) (189a 02-164)

a. Model Development (D. H. Cho)

Last Reported: ANL-7758, pp. 119-121 (Nov 1970).

(i) Parametric-model Analysis of Possible Energy-transfer-rate Controlling Mechanisms on Pressures Generated. Pressure pulses and mechanical work produced by molten fuel-coolant interactions have been studied parametrically using the rate-limited model developed earlier. (See Progress Reports for April-May 1970, ANL-7688, pp. 240-245; and July 1970, ANL-7726, pp. 159-162.) The parametric study considered a 2-ft-long molten zone across the FFTF core where 1250 kg of molten fuel at 3400°K was mixed with 196 kg of sodium at 922°K. A few less severe cases were also examined.

To examine the effect of a finite rate of fragmentation and mixing, a new formulation was used for the heating rate of the sodium mixed with the molten fuel. The heating rate per gram of sodium was given by

$$\frac{dQ}{dt} = hA(T_f - T_{Na}), \quad (1)$$

where h is the heat-transfer coefficient, A is the heat-transfer area available per gram of sodium, and T_f and T_{Na} are the average fuel and sodium temperatures. In the new formulation it was assumed that

$$h = \frac{k_f}{\sqrt{\pi \alpha_f t}} + \frac{k_f}{R} \quad (2)$$

and

$$A = A_0 \left[1 - \exp \left(-\frac{t}{t_m} \right) \right] \quad (3)$$

with $A_0 = 3W/\rho_f R$, where k_f is the fuel thermal conductivity, α_f is the fuel thermal diffusivity, R is the fuel-particle radius, ρ_f is the fuel density, W is the fuel-to-sodium mass ratio, and t_m represents a fragmentation and mixing time constant. Equation 2 assumes that the heat transfer is limited by the fuel conduction resistance alone. It does not take into account such thermal resistance as might occur if the fuel particles were surrounded by a film of gas or sodium vapor. Equations 2 and 3 do not describe the details of fragmentation, mixing, and heat transfer. Rather, Eqs. 2 and 3 together represent a convenient way of examining the effects of the fuel-particle size or the rate of fragmentation and mixing.

The latent heat of fusion of the molten fuel was taken into account by adding an equivalent temperature difference to the initial fuel

temperature. The equivalent temperature difference was obtained by dividing the latent heat of fusion by the fuel specific heat, and was about 562°C. A close examination suggests that this simple method is adequate for most calculations of interest and that any inaccuracies involved are likely to give a conservative result.

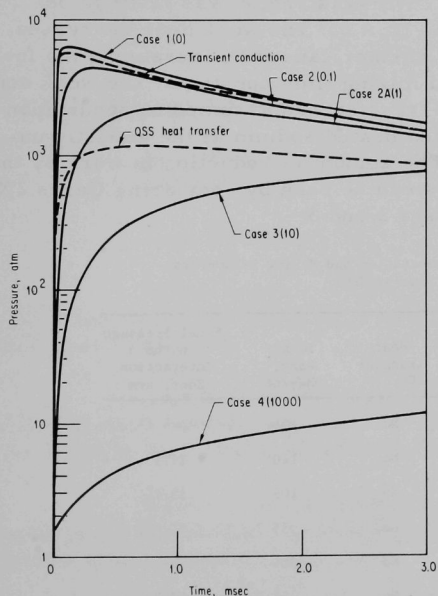


Fig. III.A.6. Effect of Various Fragmentation and Mixing Time Constants for a Fuel-particle Radius of 117 microns

A one-dimensional acoustic constraint was used for calculations of pressure-time histories during the initial shock wave. Figure III.A.6 shows the effect of different fragmentation and mixing time constants for a constant fuel-particle radius of 117 microns. As the fragmentation and mixing time constant increased, the peak pressure decreased and the pressure rise time became longer. There was no appreciable shock pressure when the time constant was 1 sec. Case 1, where $t_m = 0$, corresponds to the case of instantaneous fragmentation and mixing. It may be considered as an approximation of the transient-conduction

formulation given in ANL-7726, p. 160. Comparison of Case 1 with the transient-conduction solution (indicated by a broken curve) shows that the

difference between the two cases is small and may be neglected. Thus it appears that the form of the sodium heating rate given by Eq. 1 together with Eqs. 2 and 3 is adequate for describing the heating process, including the limiting case of instantaneous fragmentation and mixing. Figure III.A.6 also indicates that for the fuel-particle radius of 117 microns, the quasi-steady-state heat-transfer approximation (used in ANL-7726, p. 160) accounts for a fragmentation and mixing time constant of 3-4 msec. The peak shock pressure decreased with increasing fuel-particle size, and increased almost in proportion to the molten-zone length.

Parametric calculations were made of the kinetic energy of the sodium slug impacting on the reactor-vessel head. A one-dimensional model was used for the motion of the slug, which was 520 cm long and had a cross-sectional area equal to that of the reactor vessel. In this model, the slug energy represents the total work done by the molten fuel-coolant interaction up to the time of impact, and no allowance is made for the absorption of strain energy in the structure. This strain energy itself will be a function of the pressure-time history, which changes as the input parameters are varied. The pressure in the cover-gas region was assumed to remain constant at 1 atm. The initial gap of the cover-gas region was taken to be 50 cm. The results are given in Table III.A.3. The work done decreased with decreasing sodium heating rate, whether caused by increasing the fuel-particle size or the fragmentation and mixing time constant. The work done was reduced when a cutoff in the heat transfer was assumed to occur upon vaporization of the initially pressurized heated sodium at the acoustic unloading time of the sodium column. The amount of reduction in work by this cutoff depended on the heating rate, as can be seen by comparing Cases 2X and 3X with the otherwise similar Cases 2 and 3.

TABLE III.A.3. Effect of Fragmentation and Mixing Parameters on the Work Done by MFCI

Case	Fragmentation and Mixing Time, msec	Fuel-particle Radius, microns	Heat-transfer Cutoff	Total Work, MW-sec	Final Pressure in the Interaction Zone, atm
1	Infinitely fast heat transfer		No	424	--
2	0.1	117	No	140	29.9
3	10	117	No	103	32.7
4	1000	117	No	35.7	21.9
5	10	23.4	No	301	--
6	10	585	No	54.2	27.7
1X	Instantaneous thermal equilibrium followed by adiabatic expansion			140	9.5
2X	0.1	117	At unloading (1.98 msec)	125	27.4
3X	10	117	At unloading (2.68 msec)	7.1	3.7

B. Operations

1. TREAT Operations (J. F. Boland) (189a 02-122)

Last Reported: ANL-7776, p. 124 (Jan 1971).

a. Operations

Experiment HEDL-PNL-2-1 was subjected to two transients and radiographed after the transients. The experiment was then returned to HEDL.

Experiment EBR-II-MF-5 was radiographed and subjected to a series of three transients. This experiment is designed to measure axial expansion of EBR-II driver fuel.

(i) Automatic Power Level Control System. Interconnecting wires were installed between the computer and the servo-hydraulic drives, and the system is now being checked out.

C. Effluent Control

1. Environmental Studies

a. Mass/Energy Balance of the Great Lakes (J. G. Asbury) (189a 02-184)

Last Reported: ANL-7737, pp. 182-184 (Aug 1970).

Surface-water velocity data for the Waukegan Station plume were collected on the afternoon of August 24, 1970. The data have now been reduced and analyzed.

The field measurements consisted of photographing the movement of drift bottles released near the mouth of the outfall. A clock was included in the camera view to record time intervals between frames.

Five or six drift bottles were released for each run. The superposition of the streamline velocity data for all five runs yielded over 300 data points in the plume velocity field.

The data were smoothed by the computer routine SYMAP.*
A five-level SYMAP output is shown in Fig. III.C.1. The decay of center-line

*D. Shephard, "A Two Dimensional Interpolation Function for Computer Mapping of Irregularly Spaced Data," Harvard Papers in Theoretical Geography, Harvard Center for Environmental Design Studies, Harvard University, Paper No. 15 (1968).

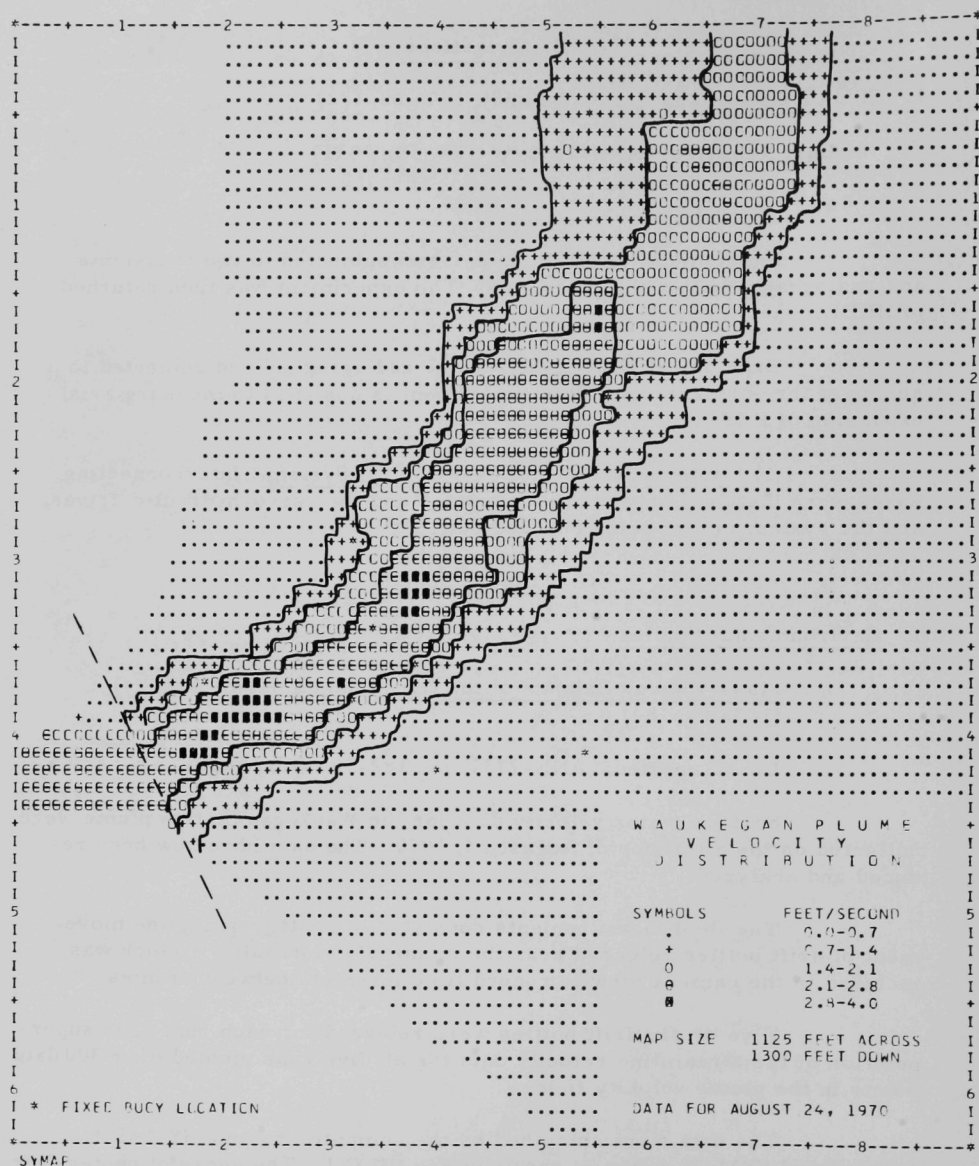


Fig. III.C.1. Velocity Map Developed by SYMAP: Five Levels

velocity was found to be reasonably consistent with the rates of temperature decay reported by Wiegel et al.*

It is concluded that the photographic technique represents a powerful technique for examining the behavior of thermal plumes. The report describing this study is currently in print.**

PUBLICATIONS

Pressure Distribution for Axisymmetric Two-dimensional Flow in a Plenum during Coolant Expulsion

T. C. Chawla and B. M. Hoglund

Nucl. Sci. Eng. 43, 87-90 (1971) Note

Safety Problems of Liquid-metal-cooled Fast Breeder Reactors

C. N. Kelber, A. M. Judd, G. Cinelli, Jr., C. E. Dickerman, H. K. Fauske,

R. E. Holtz, R. O. Ivins, W. C. Lipinski, D. R. MacFarlane,

J. F. Marchaterre, D. Miller, R. B. Nicholson, and R. M. Singer

ANL-7657 (Feb 1970)

Vaporization Dynamics of Initially Static Superheated Sodium

R. M. Singer and R. E. Holtz

ANL-7706 (Sept 1970)

The Equivalence of Dynamic Loads for the Final Plastic Deformation of a Tube

C. K. Youngdahl

1st Int. Conf. on Pressure Vessel Technology, Delft, September 29-October 2, 1969, Part 3, Discussion. ASME, New York, 1970,

p. 161 Abstract

Load-equivalence Parameters for Dynamic Loading of Structures in the Plastic Range

Carl K. Youngdahl

ANL-7677 (May 1970)

*R. L. Wiegel, I. Mobarek, and Yuan Jen, "Discharge of Warm Water Jet Over Sloping Bottom," Modern Trends in Hydraulic Engineering Research: Golden Jubilee Symposia, Vol. 2, Central Water and Power Research Station, Poona, India, pp. 144-164 (1964).

**J. G. Asbury, R. E. Grench, D. M. Nelson, W. Prepejchal, G. P. Romberg, and P. Siebold, A Photographic Method for Determining Velocity Distributions within Thermal Plumes, ANL/ES-4 (Feb 1971).

